

Dissertation
submitted to the
Combined Faculties for the Natural Sciences and for Mathematics
of the Ruperto-Carola University of Heidelberg, Germany
for the degree of
Doctor of Natural Sciences

Put forward by
M. Sc. Carlo Licciulli
born in Monopoli, Italy
Oral examination: 18.01.2018

**Full Stokes ice-flow modeling
of the high-Alpine glacier saddle Colle Gnifetti, Monte Rosa:
Flow field characterization for an improved
interpretation of the ice-core records**

Referees:

Prof. Dr. Olaf Eisen

Prof. Dr. Klaus Pfeilsticker

Abstract

The high-Alpine glacier saddle Colle Gnifetti (CG), Monte Rosa massif, is the only cold glacier archive in the European Alps offering detailed ice-core records on the millennial-scale. However, the highly irregular snow deposition pattern and the complex flow regime produce depositional noise and upstream effects, which hinder the full interpretation of the ice-core records in terms of past atmospheric changes. In this context, this work focuses on establishing a three-dimensional full Stokes ice-flow model of the CG saddle, with the main objective to calculate precise backward trajectories of existing ice-core sites, which is necessary to evaluate potential upstream effects.

The developed full Stokes model is fully thermo-mechanically coupled and includes firn rheology, firn densification and enthalpy transport, with consideration of atmospheric temperature changes of the last century, strain heating and surface meltwater refreezing. The simulations are performed using the state-of-the-art Finite Element software Elmer/Ice. The CG full Stokes model is validated by comparison with measurements of surface velocities, accumulation, annual layer thickness, borehole inclination angles, density and temperature. Estimated using different bedrock topographies, the error of the calculated source point positions on the glacier surface amounts to $\sim 10\%$ of the distance to the corresponding drill site. Moreover, the three-dimensional age field of the glacier is calculated with an uncertainty of $\sim 20\%$. The calculated chronologies of four out of five ice cores are consistent with experimental dating results, based among others on layer counting and ^{14}C measurements.

Zusammenfassung

Der hochalpine Gletschersattel Colle Gnifetti (CG), Monte Rosa Massiv, ist das einzige kalte Gletscherarchiv in den Europäischen Alpen, das detaillierte jahrtausendalte Eiskernzeitreihen liefert. Jedoch führen die höchst unregelmäßigen Schneeakkumulationsraten und das komplexe Fließfeld zu sehr variablen Depositionen und Gletscherfließeffekten, die die Interpretation der Eiskern-Zeitreihen hinsichtlich atmosphärischer Veränderungen der Vergangenheit behindern. In diesem Zusammenhang zielt diese Arbeit auf die Erstellung eines dreidimensionalen Full-Stokes Eis-Fließmodells des CG Sattels, mit dem Hauptziel präzise Rückwärtstrajektorien von existierenden Bohrplätzen zu berechnen. Diese Trajektorien werden für die Auswertung potenzieller Gletscherfließeffekte benötigt.

Das entwickelte Full-Stokes-Modell ist vollständig thermomechanisch gekoppelt und enthält Firn-Rheologie, Firn-Verdichtung und Enthalpie-Transport, mit Berücksichtigung der atmosphärischen Temperaturänderungen des letzten Jahrhunderts, der Deformationswärme und des wieder gefrierenden Oberflächenschmelzwassers. Die Modellsimulationen wurden mit der state-of-the-art Finite-Elemente-Software Elmer/Ice durchgeführt. Das CG Full-Stokes Modell wurde durch einen Vergleich mit Messungen von Oberflächengeschwindigkeiten, Oberflächenakkumulation, Jahresschichtdicke, Bohrlochinklinationswinkeln, Dichte und Temperatur validiert. Die Ungenauigkeit der berechneten Trajektorienausgangspunkte auf der Gletscheroberfläche wurde mit der Verwendung verschiedener Felsbett-Topografien abgeschätzt und beträgt $\sim 10\%$ der Distanz zu den entsprechenden Bohrstellen. Außerdem wurde die dreidimensionale Eisaltersverteilung des Gletschers mit einer Unsicherheit von $\sim 20\%$ berechnet. Die berechneten Alters-Tiefe-Beziehungen von vier von fünf Eiskernen sind konsistent mit experimentellen Datierungsergebnissen, die u.a. auf Abzählen von Jahresschichten und ^{14}C Messungen beruhen.

Contents

1	Introduction	1
2	The Colle Gnifetti drilling site	5
2.1	Glaciological settings	5
2.2	IUP ice-core drilling projects	8
2.3	Previous ice-flow modeling studies at CG	9
3	Glacier dynamics	13
3.1	Firn and ice	13
3.1.1	Glacier zones	13
3.1.2	Firn to ice transformation in the dry-snow zone	14
3.2	Ice deformation	14
3.3	Stress and strain-rate tensor	15
3.4	Field equations	17
3.4.1	Momentum, mass and energy conservation	17
3.4.2	Enthalpy transport	18
3.4.3	Free-Surface equation	19
3.4.4	Dating equation	19
3.5	Constitutive equations	20
3.5.1	Glen’s flow law	20
3.5.2	Ice slab model	21
3.5.3	Rheology of compressible firn	22
3.5.4	The role of bubble close-off	24
3.5.5	Anisotropic flow: GOLF	25
3.6	Thermal properties of firn and ice	26
4	Field measurements (2014–16)	29
4.1	Horizontal surface velocities	29
4.2	Surface topography	34
4.3	Borehole inclination angles	36
5	Ice-flow modeling of Colle Gnifetti	41
5.1	Glacier geometry	41
5.1.1	Glacier sectors	41
5.1.2	Stationarity	42
5.1.3	Surface topography	43
5.1.4	Bedrock topography and glacier thickness	44

5.2	Mechanical boundary conditions	47
5.2.1	Lateral boundaries	47
5.2.2	Basal conditions	48
5.3	Thermodynamic boundary conditions	48
5.3.1	Spin-up surface temperatures	49
5.3.2	Atmospheric forcing	50
5.3.3	Surface meltwater refreezing	51
5.3.4	Basal heat flux	54
5.4	Operating the model	55
6	Numerical implementation	59
6.1	The Finite Element software Elmer/Ice	59
6.2	The mesh	60
6.3	Deployed Solvers and User Functions	61
6.4	Implementation of bubble close-off	62
6.4.1	Modification of the Porous-Solver (firn flow law)	63
6.4.2	Test: Application on a simple test case	64
6.4.3	Test: Application to Colle Gnifetti	66
6.5	Attempt to combine firn and anisotropic flow law	68
7	Results: Model validation and applications	71
7.1	Velocity field	71
7.1.1	Horizontal surface velocities	71
7.1.2	Bulk velocities (firn flow law)	73
7.1.3	Diagnostic run using the anisotropic flow law	77
7.1.4	Borehole inclination angles	80
7.2	Surface accumulation	86
7.3	Density field	89
7.4	Temperature field	90
7.5	Calculation of trajectories	93
7.6	Dating of the ice cores	97
7.7	Depths of equal age	102
8	Summary and outlook	105
	Bibliography	109
	Lists	119
	List of Figures	119
	List of Tables	121
	List of Abbreviations	123
A	Appendix	125
A.1	Measured surface velocities (2014–16)	125
A.2	Measured surface accumulation (2014–16)	126

A.3 Orientation angles measured at KCC and KCI	127
A.4 Convergence plots	129
A.5 Ice-core source coordinates and chronologies	130

Acknowledgements	137
-------------------------	------------

1 Introduction

Human activities have a clear impact on the climate and are unequivocally connected to recent climate changes [IPCC, 2014]. The analysis of past climate variability is mandatory to understand the complex processes driving present and future climate changes. Apart from climate model simulations, this requires the exploration of natural climate archives like tree rings, stalagmites, sea sediments, or glacier ice. Compared to other sedimentary archives, glaciers and ice-sheets provide the most complete record of our past environments. That includes past temperatures derived from the isotopic composition of snow and ice [Johnsen et al., 2001], and past atmospheric composition inferred from various aerosol-derived species (e.g. sulfate or carbonaceous matter) trapped in the ice lattice [Wolff et al., 2010] as well as trace gases (e.g. CO₂ or CH₄) encapsulated in air bubbles of ice [Lüthi et al., 2008]. In this way, the analysis of Antarctic ice cores has provided records of climate parameters up to 800,000 years ago [Lambert et al., 2008], whereas the recovery of 1.5 million years old Antarctic ice is considered as possible [Fischer et al., 2013].

The geographical coverage of ice-core records can be extended outside polar regions by investigating glaciated mountain areas located at middle and low latitudes. In this context, the European Alps are of particular interest, since located very close to high populated areas and to the major European anthropogenic emissions [Wagenbach et al., 2012]. However, since the stratified ice archive needs to be preserved from percolating meltwater, suitable drilling sites in the Alps are confined to the very high summit ranges, where the temperatures remain well below zero during the whole year. In the Alps, so called *cold glaciers* are limited in number, have a small horizontal extension and can provide records covering the last 100 years or more [Wagenbach et al., 2012]. Examples of high-altitude glaciers subject to ice-core studies are: Col du Dôme (Mont Blanc) [Preunkert et al., 2000], Fiescherhorn (Bernese Alps) [Schwerzmann et al., 2006], Ortles (Eastern Alps) [Gabrielli et al., 2016] and Colle Gnifetti (CG, Monte Rosa massif) [Wagenbach et al., 2012].

Among these glaciers, the CG glacier saddle is the only drilling site where the net snow accumulation is low enough to offer continuous ice-core records on the millennial time scale [Jenk et al., 2009]. The exceptionally low accumulation observed at CG, by far lower than the meteorological precipitation rate [Bohleber et al., 2013], produces very thin annual layers. This is a consequence of the strong wind erosion, favoured by the topography and orientation of the glacier. The CG is subject to ice-core studies since the 1970s [Oeschger et al., 1977; Schotterer et al., 1978; Gäggeler et al., 1983; Wagenbach and Geis, 1989]. In the frame of projects led by the Institute of Environmental Physics (IUP), Heidelberg University, since 1982 five ice cores were drilled down to bedrock

at CG [Wagenbach et al., 2012], with the ice-core project KCC [Bohleber et al., 2017] being the most recent drilling effort (August 2013).

One caveat at the CG is that the wind-induced snow deposition pattern is highly irregular in space and time, which hampers the full exploitation of the CG ice-core records in view of reconstructing atmospheric changes of the past. Due to the highly variable accumulation rate, the small initial annual layer thickness and their rapid thinning in the vicinity of the glacier base (frozen to bedrock), dating of the ice cores deploying conventional cm-resolution annual layer counting techniques becomes a challenge after only a few hundred years. Only recently, annual layer counting could be extended over the last 1000 years (KCC core), deploying state-of-the-art Continuous Flow Analysis (CFA) of ice impurities and Laser Ablation Inductively Coupled Plasma Mass Spectrometry (LA-ICP-MS) at sub-mm depth resolution [Bohleber et al., 2017], with additional constraints from radiocarbon dating results of the basal ice [Hoffmann, 2016; Hoffmann et al., 2017].

Besides random depositional noise, which includes negative accumulation with missing annual layers, spatial and temporal changes of the accumulation rate show a strong systematic component as well. On the one hand wind erosion is more efficient at steep slopes and under colder atmospheric conditions, while on the other hand wind erosion is less efficient in areas with enhanced solar irradiation, where the snow consolidates faster and is more likely protected by ice crusts. As a consequence, at CG the accumulation rate is systematically lower in steep shady areas and systematically higher during the warmer half of the year [Preunkert, 1994; Armbruster, 2000; Wagenbach et al., 2012; Bohleber et al., 2013].

The ice particles retrieved in the ice cores were originally deposited as snow on the glacier surface upstream of the drilling site and, the deeper in the ice core, the further from the drilling site. In particular at CG, since located on a steep and north-facing flank of the glacier, the catchment area of the ice cores is characterized by lower and summer-biased accumulation. This produces so-called upstream effects, which may lead to misinterpretation of the climate signal recorded in the CG ice archive.

The only way to evaluate upstream effects is to identify the catchment area of the ice cores as precisely as possible. This can only be achieved calculating ice particles trajectories within the glacier body using numerical models. With this aim, several ice-flow modeling studies were conducted since the late 1980s [Haeberli et al., 1988; Wagner, 1996; Lüthi, 2000; Lüthi and Funk, 2000; Konrad et al., 2013]. Among these studies, the work of M. Lüthi stands out for the complexity of the developed flow model (3D full Stokes, with consideration of firn rheology and using the Finite Element method) and quality of the results. In particular, the model was able to reconstruct density and temperature profiles available at that time (late 1990s). Moreover, ice-core dating obtained using the model was in good agreement with experimental methods, at least for few hundred years. The model results were mainly limited by the accuracy of the bedrock topography used, and by the low coverage of englacial temperature measure-

ments, especially in the eastern part of the glacier.

Since the work of M. Lüthi the density of measurements available at CG has strongly improved. New englacial temperature profiles were measured [Hoelzle et al., 2011] and new ground-penetrating radar (GPR) tracks give a more detailed image of the bedrock and of the internal structure of the glacier [Eisen et al., 2003; Bohleber, 2011; Konrad et al., 2013]. Two new ice cores were drilled in 2005 (KCI) and 2013 (KCC). Particularly the drilling project KCC employs a unique approach of combining multiple state-of-the-art methods in ice-core analysis: new ultra-high resolution impurity analysis for detecting highly thinned annual layers [Bohleber et al., 2017], novel micro-radiocarbon dating techniques to constrain the age of the bottom ice layers [Hoffmann, 2016; Hoffmann et al., 2017], as well as measurements of the crystal-orientation fabric distribution [Kerch, 2016], which has an impact on the flow dynamics of the glacier.

The availability of these new and novel data sets, together with the still existing lack of information with respect to the correct evaluation of upstream effects at CG, motivates a new modeling attempt. In this context, the main goals of this study are:

- to determine the flow dynamics of the CG glacier saddle by means of state-of-the-art numerical ice-flow modeling;
- to calculate backward trajectories of the ice retrieved in the ice cores at different depths and map the source regions, in order to make the evaluation of potential upstream effects possible;
- to provide a reliable three-dimensional age field of the glacier, in order to assist experimental methods in dating the ice cores and calculate depths of equal age, necessary for the intercomparison of different records within the CG multi-core array.

To do so, the flow dynamics of the glacier is reproduced using a three-dimensional full Stokes ice-flow model, fully thermo-mechanically coupled, with consideration of firn rheology and transient temperature changes over the last century. The simulations are performed using the Finite Element software Elmer/Ice [Gagliardini et al., 2013], already widely used for small-scale ice-flow problems of high mechanical and physical complexity [Gagliardini et al., 2011; Gilbert et al., 2014a, 2015], as well as on large polar ice-sheets [Gillet-Chaulet et al., 2012; Seddik et al., 2012].

The main challenge in modeling the flow dynamics of CG consists in dealing with a compressible firn rheology in the firn part of the glacier, as well as with anisotropic ice rheology in the deeper part of the glacier [Kerch, 2016]. However, up to now no flow law is available, which takes into account both rheologies. Therefore within the final results only the firn flow law is used. A further challenge is the small-scale geometry of the saddle, typical for high-elevation summit areas, counting complex bedrock topography and lateral boundary conditions, including the presence of a bergschrund

(southern boundary), of a large crevasse (western boundary) and of an ice cliff (eastern boundary). Moreover, the complex geometry also produces non-trivial thermodynamic boundary conditions, due to the presence of areas with different solar exposition (on the glacier surface as well as on the slopes of the whole mountain below the glacier). To prove the reliability of the model developed within the framework of the present thesis, the model calculations are validated through comparison with measured surface velocity, surface accumulation, annual layer thickness (ice cores), density profiles (ice cores), borehole inclination angles and englacial temperatures.

Details about the CG drilling site, past ice-core drilling projects and previous modeling studies are given in chapter 2. An overview of the physics governing the glacier flow can be found in chapter 3. Field measurements performed at CG within this work are presented in chapter 4. The measurements include surveys of surface flow velocities, surface topography and borehole inclination angles. In chapter 5 the CG full Stokes model is introduced. In particular, data used to define the glacier geometry are presented and the process for defining mechanical and thermal boundary conditions is outlined. Moreover it is explained how the field equations presented in chapter 3 are used in the full Stokes model. Chapter 6 briefly introduce the Elmer/Ice software and the solvers used to run the model. Model validation and results are presented in chapter 7, whereas a final summary is given in chapter 8.

2 The Colle Gnifetti drilling site

The peculiar glaciological settings of the Colle Gnifetti glacier are presented in section 2.1. Ice cores recovered at Colle Gnifetti in the frame of IUP drilling projects are briefly presented in section 2.2, with main focus on the ice core KCC recovered in 2013. Since the late 1980s different modeling studies were performed on Colle Gnifetti. Those are introduced in section 2.3.

2.1 Glaciological settings

The high-Alpine glacier saddle Colle Gnifetti (CG) is part of the summit ranges of the Monte Rosa massif in the Swiss/Italian Alps. The saddle is situated at ca. 4450 m a.s.l. and lies between Signalkuppe (4554 m a.s.l.) and Zumsteinspitze (4563 m a.s.l.), as shown in Figure 2.1 and 2.2. The glacier has a rather small horizontal extension of about $500 \times 500 \text{ m}^2$ and a maximal thickness of ca. 140 m [Lüthi and Funk, 2000], with the firn-ice transition at about half of the glacier depth. According to geodetic surveys

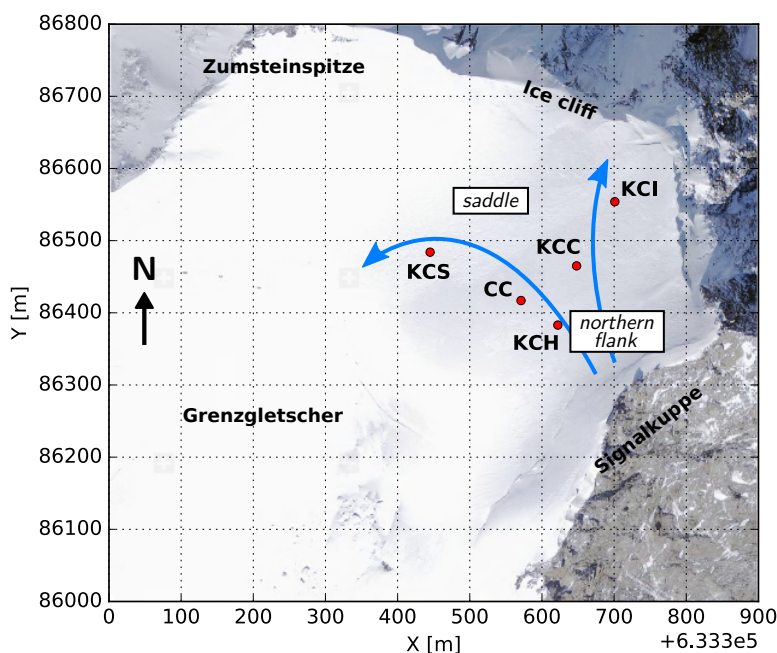


Figure 2.1: North oriented areal imagery of the CG glacier saddle, Monte Rosa massif. The north-exposed flank below Signalkuppe is subject to climatological studies since the 1970s. Coordinates are in the official Swiss coordinate system. Areal imagery from <https://map.geo.admin.ch>.

and comparisons with photographs, the geometry of the glacier was near to steady state at least until the year 2000 [Haerberli et al., 1988; Wagner, 1996; Lüthi, 2000] (more details in section 5.1.2).

The north-exposed slope of the CG saddle, i.e. the area below Signalkuppe, is characterized by a very low surface accumulation (see below) and is subject to climate and environmental ice-core studies since the 1970s [Oeschger et al., 1977; Schotterer et al., 1978; Gäggeler et al., 1983; Wagenbach and Geis, 1989] (see section 2.2). The ice flow of the area is divided in two different directions (blue lines in Figure 2.1 and 2.2, left). While the southern part flows in the direction of Grenzgletscher (westwards), the other part flows in the direction of a steep ice cliff (eastwards). Surface flow velocities are of the order of 1 m a^{-1} (see section 4.1).

Temperature regime

Due to its location well above 4000 m a.s.l., the CG saddle is a *cold glacier*, i.e. the englacial temperatures are well below zero throughout the whole year, and accumulation is exclusively made up by solid precipitation. These are basic prerequisites in order to hold the stratigraphy of the annual layers undisturbed. At the glacier bed the temperatures are in a range of -13°C to -12°C [Hoelzle et al., 2011]. The glacier is therefore frozen to bedrock. However, an accelerated englacial warming is evident, with a rate of 0.05°C per year in the period from 1991 to 2000 and 0.16°C per year in the period from 2000 to 2008 [Hoelzle et al., 2011]. Surface melt is rather uncommon and meltwater percolation is confined to the uppermost annual layer [Bohleber et al., 2013]. According to the classification of the glacier zones (see section 3.1.1), the north-exposed area of CG belongs to the so-called percolation zone.

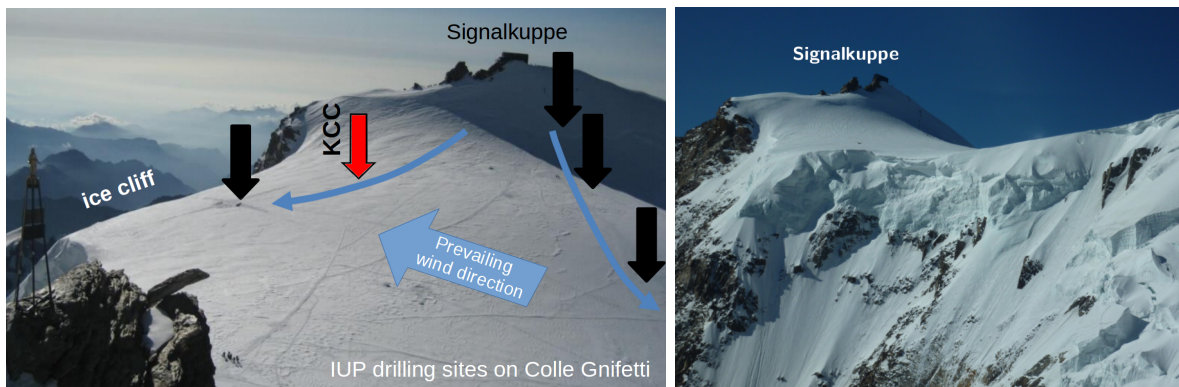


Figure 2.2: The CG glacier saddle. Left: view of the saddle from Zumsteinspitze. Black and red arrows indicate the approximative drilling position of the ice cores recovered within projects led by the IUP Heidelberg. The ice core KCC (red arrow) was recovered in summer 2013 and is the most recent. Right: view of saddle and of the ice cliff from east.

Snow accumulation and upstream effects

Due to strong wind erosion, the net snow accumulation observed at CG is exceptionally low, i.e. ca. 0.15 to 1.2 m w.e. a⁻¹ (meter water equivalent) [Bohleber et al., 2013]. As shown in Figure 2.2 (left) the orientation of the saddle is such that freshly fallen snow can be easily blown across the downwind situated ice cliff and permanently removed from the glacier. Compared to the climatological precipitation rate, at CG the net surface accumulation can be lower by up to a factor of nine [Bohleber et al., 2013].

Since governed by wind erosion, the surface accumulation pattern of CG is highly variable in space and time. Moreover, the wind erosion is more or less efficient depending on the local surface slope and aspect [Alean et al., 1983]. In particular, at areas with enhanced solar irradiation snow consolidation is faster and refreezing surface melt or insolation crusts may protect the snow from wind scouring [Wagenbach et al., 2012]. According to this, wind erosion is in general less efficient during the warm seasons, which are therefore characterized by higher accumulation rates [Preunkert, 1994; Armbruster, 2000; Wagenbach et al., 2012].

Figure 2.3 [Bohleber et al., 2013] illustrates this fact showing systematically higher accumulation rates at the saddle area compared to the north-exposed flank below Signalkuppe. In addition, the mean $\delta^{18}\text{O}$ level, i.e. a proxy of the precipitation temperature, is higher at location with lower accumulation, which indicates that in this latter areas the snow is mainly deposited during the warmer seasons. Note that the area close to the ice cliff (not shown in Figure 2.3) is characterized by very low and summer biased snow accumulation as well.

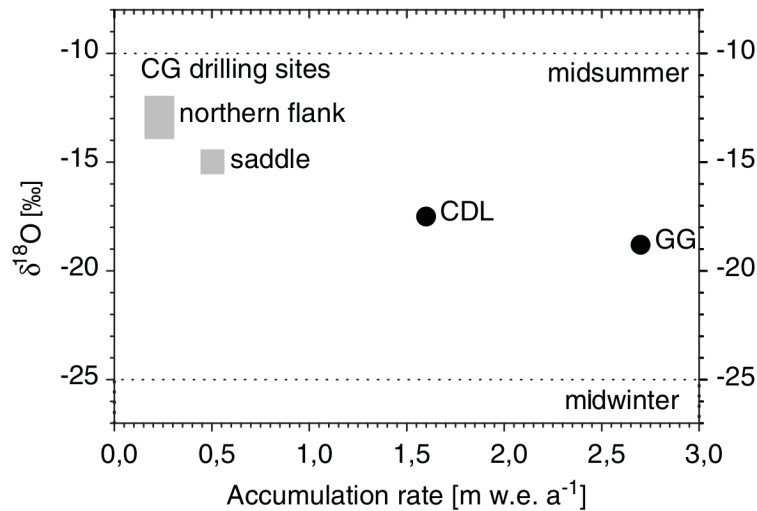


Figure 2.3: Accumulation rate and mean $\delta^{18}\text{O}$ level at CG and other drill sites in the Monte Rosa area: Colle del Lys (CDL) and Grenzgletscher (GG). The accumulation rate observed at CG is much less than at CDL and GG, which are less exposed to wind erosion. Moreover, whereas at CDL and GG the snow deposition is evenly distributed over the year, at CG (in particular in the northern flank area) a consistent part of the snow is deposited during summer. Figure taken from Bohleber et al. [2013].

Taking advantage of the cold glacier temperatures, several ice cores were recovered in the north-exposed area of CG over the last 35 years (see section 2.2). Since the catchment areas of the ice cores are located upstream of the ice cores themselves, the systematic spatial variations in the snow accumulation characteristics and in the deposition pattern discussed above produce so-called *upstream effects*, which need to be taken into account for the reliable interpretation of the respective ice-core records [Bohleber et al., 2013].

2.2 IUP ice-core drilling projects

Figure 2.1 and 2.2 show the approximate drilling position of the five CG ice cores drilled down to bedrock under the responsibility of the IUP Heidelberg. The ice cores are all recovered from the north-exposed flank of CG, to profit of the low net snow accumulation and the undoubted upstream area (the north-exposed flank), mandatory to get undisturbed long-term ice-core records. The drill sites CC (recovered in 1982), KCH and KCS (both recovered in 1995) are placed approximately along a common flowline, i.e. the flowline pointing in the direction of Grenzgletscher (see Figure 2.1 and 2.2). The ice cores KCI (recovered in 2005) and KCC (recovered in 2013) are located in the eastern part of the glacier, both approximately on a common flowline pointing towards the ice cliff. Main characteristics of the five ice cores are summarized in Table 2.1.

Table 2.1: Characteristics of the five ice cores drilled to bedrock at CG in the frame of IUP drilling projects. Data taken from Bohleber et al. [2013] and Bohleber et al. [2017].

Ice-core name	KCC	KCI	KCH	CC	KCS
Total depth (absolute) [m]	72	62	60	64	100
Total depth [m w.e.]	54	48	45	50	79
Year of drilling	2013	2005	1995	1982	1995
Mean accumulation [m w.e. a ⁻¹]	0.22	0.14	0.23	0.22	0.51
Firn-ice-transition [m]	35	27	28	31	43

Due to the low annual deposition rate and its high spatial and temporal variability (see section 2.1), the age–depth relation of the CG glacier is highly non-linear and thus ice core dating becomes very challenging. Ice-core chronologies of KCI, KCH, CC and KCS were estimated on the base of (a) absolute age–depth markers (e.g. the ³H bomb peak of 1963 AD, and the attempt to assign prominent Volcano and Saharan dust events), (b) annual layer counting exploiting trace-substances with a clear seasonal cycle (e.g. NH₄⁺), and (c) simple layer thinning models [Schäfer, 1995; Armbruster, 2000; Keck, 2001; Bohleber, 2008]. The chronologies of those older cores are used in this work to compare with the ice-core chronologies produced using the full Stokes model (see section 7.6).

The KCC ice core

To investigate the age–depth relation of the KCC ice core recovered in 2013 at CG, several partially novel analytical techniques were applied (not included in this work):

- Continuous Flow Analysis (CFA) deployed to measure stable water isotopes, melt-water conductivity, insoluble particle concentration and size distribution, and selected ion species (Ca^{2+} , NH_4^+ , NO_3^- , Na^+) with a resolution of 0.5 to 1.2 cm [Bohleber et al., 2017]. The measurements were conducted at the Division for Climate and Environmental Physics, Physics Institute, at the University of Bern.
- Laser Ablation Inductively Coupled Plasma Mass Spectrometry (LA-ICP-MS) deployed to analyze ^{44}Ca with a resolution better than $120\ \mu\text{m}$ [Bohleber et al., 2017]. The measurements were performed in the WM Keck Laser Ice Facility at the Climate Change Institute (University of Maine).
- Radiocarbon (^{14}C) dating of the microscopic Particulate Organic Carbon (POC) fraction incorporated into the ice matrix. The measurements were conducted at the IUP Heidelberg [Hoffmann, 2016; Hoffmann et al., 2017].
- Crystal-Orientation Fabric (COF) and ice microstructure measurements, conducted for several intervals along the core and covering more than 10% of the core length. The measurements were performed at the Alfred Wegener Institute (AWI) and are described in Kerch [2016].

Combined data sets obtained from CFA and LA-ICP-MS were used for an attempt to date the ice core on the base of annual layer counting, whereas radiocarbon dating was deployed to provide absolute ice age constraints in the bottom part of the ice core. According to radiocarbon measurements, the age of the bottom section of the KCC core is older than 4000 years [Hoffmann et al., 2017]. In the present work, the KCC chronology based on annual layer counting [Bohleber et al., 2017; pers. comm. P. Bohleber, 2017] and the radiocarbon dating results [Hoffmann, 2016; Hoffmann et al., 2017; H. Hoffmann, per. comm.] are used for comparison with the age–depth chronology calculated using the full Stokes model (see results in section 7.6).

Evidence for anisotropic ice fabrics at CG was already found in seismic surveys [Diez et al., 2013]. According to COF measurement results [Kerch, 2016], in the deep part of the KCC core the c -axes of the ice crystals tend to have a strong preferred orientation in the vertical direction (single-maximum fabrics). The elements of the second-order orientation tensor measured at KCC [Kerch, 2016] are used in this work as input to run tests using the anisotropic flow law GOLF (see section 7.1.3).

2.3 Previous ice-flow modeling studies at CG

The first ice-flow calculations of the CG glacier were made by Haeberli et al. [1988]. The hereby established model was dedicated to calculate ice particles trajectories and ages of ice samples from ice cores. The geometry of the glacier bed was known from

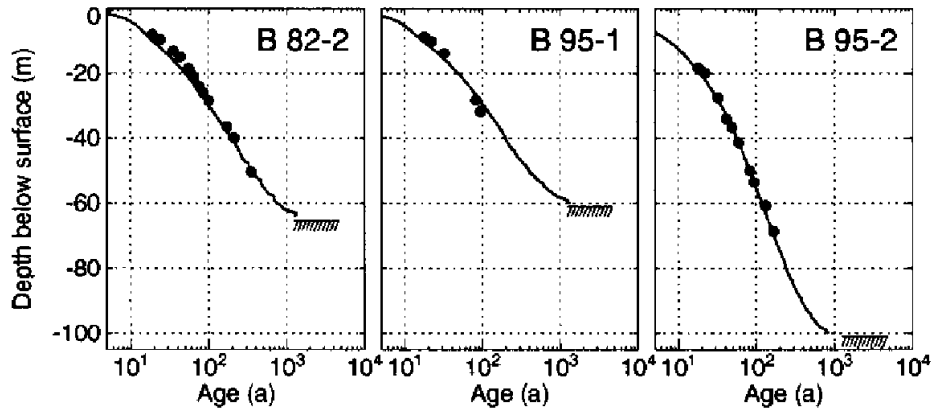


Figure 2.4: Ice-core chronologies of three CG ice cores calculated using the full Stokes model presented in Lüthi [2000] and Lüthi and Funk [2000], and compared to experimental dating results (black dots). Note that B82-2 corresponds to the CC core, B95-1 to KCH and B95-2 to KCS. Figure taken from Lüthi and Funk [2000].

radio-echo soundings. The trajectory calculation was based on a simple parallel slab approximation using Glen’s law (two-dimensional, see Glen’s law description in section 3.5.1) and assuming zero flow velocities at bedrock (glacier frozen to bedrock). The surface velocity field required for the calculations was determined by surveying a network of 30 stakes.

The first three-dimensional ice-flow model of CG was produced in the 1990s [Wagner, 1996]. The three-dimensional glacier geometry was based on a new surface and bedrock topography, measured in 1989–1990. The calculations were performed using a Finite Element software. Glen’s law was used, whereas the Glen’s parameter A and n were adjusted in order to better reproduce the measured flow field. The prescribed temperature field was based on data available from Haeberli and Funk [1991]. The calculated flow field was deployed to calculate source trajectories and chronologies of the ice core CC.

A successive and more complex modeling study of the CG glacier is described in Lüthi [2000], Lüthi and Funk [2000] and Lüthi and Funk [2001]. The study included two-dimensional flowline simulations, as well as three-dimensional simulations. The modeling approach was similar to the modeling approach of the here presented work, i.e. full Stokes and deploying the Finite Element method. Firn rheology was taken into account using the compressible firn flow law proposed in Gagliardini and Meyssonier [1997] and bubble close-off was considered. This represents a huge improvement compared to previous studies, which used the incompressible Glen’s law.

While the calculated surface velocity field was in agreement with surface velocities measured using stakes, manual adjustments of the bedrock topography in the north-eastern part of the glacier (poorly constrained by measurements) were necessary. The model was also able to calculate density profiles, by coupling the flow model with the den-

sification model, and the calculated density profiles were in good agreement with ice core density profiles. The model was applied to calculate backward trajectories and ice-core chronologies of the CC, KCH and KCS ice cores, which are shown in Figure 2.4 [Lüthi and Funk, 2000]. The agreement with experimental dating results was very good, however not enough experimental data were available to validate the calculated basal ages.

The model was further employed to calculate the temperature field of CG [Lüthi and Funk, 2001]. Some results are shown in Figure 2.5. Taking into account atmospheric temperature changes (transient simulation), temperature profiles calculated at the drilling sites B95-1 and B95-2 (i.e. KCH and KCS) were in good agreement with measurements (dots and triangles). Further, a borehole temperature profile measured in 1982 was well reproduced by a steady state simulation (thin dashed line) indicating that the CG temperature field was close to steady state in 1982.

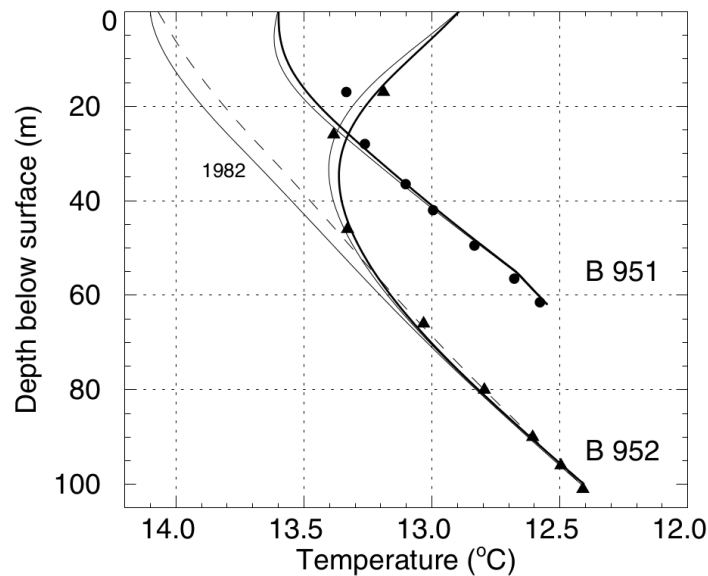


Figure 2.5: Englacial temperatures calculated for CG using the heat flow model presented in Lüthi and Funk [2001]. The thick lines are model calculations for the year 1997. Dots and triangles represent field measurements. A temperature profile measured in 1982 (thin solid line) is compared with a steady state temperature profile (thin dashed line). Figure taken from Lüthi and Funk [2001].

The work presented in Konrad [2011] and Konrad et al. [2013] was the most recent ice-flow modeling study developed for CG, and was based on a totally different approach compared to Lüthi and Funk [2000] and the present study. The model was two-dimensional and based on the parallel slab approximation (using Glen’s law), however more complex since limited uphill (which implies surface accumulation) and with an additional parameter accounting for transversal mass fluxes. The model required as input bedrock and surface topography, accumulation rate, density and lateral flux

parameters. Bedrock and surface topography were approximated by a piecewise linear function (piecewise ice slab). From this, the model could calculate trajectories, isochrones and vertical age distributions (virtual ice-core chronologies). The calculated isochrones were compared to GPR-derived isochrones up to ages of 44 years, showing a general good agreement in the shape of the isochrones.

3 Glacier dynamics

In the following, synthesis is given on the mechanical and thermodynamical principles which determine the dynamic behaviour of Alpine Glaciers, following mainly the standard works of Greve and Blatter [2009] and Cuffey and Paterson [2010].

3.1 Firn and ice

3.1.1 Glacier zones

Since single glaciers may extend over a wide altitudinal range, it is helpful to classify zones of glaciers, rather than entire glaciers. Classifications of glacier zones were proposed in different studies [Benson, 1962; Müller, 1962; Shumskii, 1964]. Here I present the classification described in Cuffey and Paterson [2010]:

- *Dry-snow zone* (or *recrystallization zone*): the air temperatures are low enough, that no surface melting occurs at all. The surface of the dry-snow zone therefore exclusively consists of snow/firn¹. Examples are the central parts of Greenland and Antarctica, as well as very high mountain summits.
- *Percolation zone* (or *recrystallization-infiltration zone*): surface melt may occur. However, meltwater percolation is restricted to the uppermost firn layers. Meltwater refreezing produces *ice layers* (or *ice lenses*).
- *Wet-snow zone*: meltwater infiltrates deeper into the snow, even more than one annual layer, warming the last annual layer up to 0 °C.
- *Superimposed-ice zone*: the meltwater production is so high, that the ice layers merge to a continuous ice mass. The boundary between the wet-snow zone and the superimposed-ice is called the *firn-line* and corresponds to the visible boundary line between firn and ice at the glacier surface at the end of the melt season.
- *Ablation zone*: the zone of the glacier below the *equilibrium-line*², thus the zone with net mass loss. The glacier surface of the ablation zone is typically made of ice.

¹Aged snow, deposited at least before the last warm season

²Boundary between accumulation and ablation zone, where accumulation and ablation are equal

3.1.2 Firn to ice transformation in the dry-snow zone

In the dry-snow zone the transformation of surface firn (typical density $\sim 400 \text{ kg m}^{-3}$) to glacier ice ($\rho_{ice}=917 \text{ kg m}^{-3}$) takes place without meltwater formation and infiltration. The transformation process follows the thermodynamic principle of minimizing the free energy of the system, which implies the reduction of the total surface area of individual ice crystals and ultimately of the ice body [Cuffey and Paterson, 2010]. At low densities, i.e. in the initial stage of firn compaction, the reduction of the total surface area occurs by smoothing and rounding of the ice crystals, and settling is the major process of densification [Cuffey and Paterson, 2010]. According to packing experiments, settling of spherical ice particles can increase the firn density up to 550 kg m^{-3} [Cuffey and Paterson, 2010]. A further reduction of the total surface area of the system is achieved by creating bonds between the spherical particles (already before reaching 550 kg m^{-3}). At low densities, sublimation and recondensation is the driving mechanism of bonds formation, by transporting material from the convex spherical particle boundaries to the concave necks between the spheres.

By increasing the density, sublimation is greatly reduced, due to the more limited vapour diffusion. At this stage recrystallization and deformation are the dominant processes of densification. At about 730 kg m^{-3} most of the residual air resides in thin channels [Cuffey and Paterson, 2010]. At $\sim 830 \text{ kg m}^{-3}$, the so-called close-off density, the remaining interstitial air is sealed off in air bubbles (*pore close-off*) [Cuffey and Paterson, 2010; Schaller et al., 2017] and the firn has become glacier ice. Under pressure, the ice density can be further increased by compression of the air bubbles, which produces an increase of air pressure in the bubbles. Implications of bubble close-off for the ice rheology are discussed in section 3.5.4. At sufficiently high depths (900 to 1600 m in central Greenland and 500 to 1200 m in central East Antarctica [Kipfstuhl et al., 2001], i.e. on the millennial time scale) the gas molecules are incorporated in the crystal lattice and form *clathrate hydrates* [Miller, 1969], inducing the disappearance of the bubbles [Cuffey and Paterson, 2010].

3.2 Ice deformation

Single crystal deformation

The crystalline structure of ice consists of layers of hexagonal rings [Greve and Blatter, 2009]. The plane identified by the layers is called *basal plane*, whereas the *c*-axis represents the direction perpendicular to the basal planes. The mechanical properties of single ice crystals are highly anisotropic. In comparison to other planes, applying a shear stress to the basal planes produces much more rapid deformation of the crystal, since the basal planes can easily glide one upon each other [Greve and Blatter, 2009]. The basal planes can slip on top of each other because of defects in the crystal lattice known as *dislocations*. In general, the more dislocations exist, the easier it is to deform the ice. Moreover, the number of dislocations increases with increasing deformation.

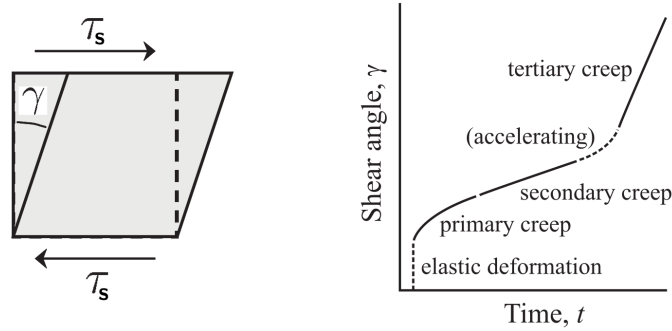


Figure 3.1: Deformation of a polycrystalline ice sample (schematic representation) under application of a constant shear stress τ_s . Right: the creep curve $\gamma(t)$. Figure modified from Greve and Blatter [2009].

Creep of polycrystalline ice

Natural glacier ice is made of a large number of ice crystals and is therefore called *polycrystalline ice* [Greve and Blatter, 2009]. The typical size of the single ice crystals (also called *grains*) varies from the mm- to the cm-scale. In polycrystalline ice, the *c*-axes of single ice crystals have different orientations. If the *c*-axes are randomly oriented, the macroscopic behaviour of polycrystalline ice is isotropic.

Figure 3.1 shows the typical behaviour of a polycrystalline ice sample under application of a constant shear stress τ_s . The deformation is quantified with the shear angle γ , whereas the time evolution of γ is described by the creep curve $\gamma(t)$ (Figure 3.1, right). After an initial instantaneous elastic deformation, the shear rate $\dot{\gamma}$ decreases continuously, due to the presence of unfavourably oriented crystals (i.e. *c*-axes). This phase is called *primary creep*. The shear rate decreases until a minimum is reached. In the following phase, called *secondary creep*, the deformation increases linearly with time. In a later stage, if temperature and/or stress conditions are high enough, recrystallization may occur. This produces ice crystals favourably oriented for deformation, leading to an accelerated creep. Finally, a constant shear rate is reached again (*tertiary creep*), however a much higher rate than the secondary creep rate.

3.3 Stress and strain-rate tensor

The stress tensor

The *Cauchy stress tensor* $\boldsymbol{\sigma}$ (or *stress tensor*) is a tensor of second order. The three-dimensional stress tensor has the form:

$$\boldsymbol{\sigma} = \begin{pmatrix} \sigma_{xx} & \sigma_{xy} & \sigma_{xz} \\ \sigma_{yx} & \sigma_{yy} & \sigma_{yz} \\ \sigma_{zx} & \sigma_{zy} & \sigma_{zz} \end{pmatrix} \quad (3.1)$$

The physical meaning of the components of the stress tensor is visualized in Figure 3.2: the first index indicates the surface on which the stress is applied, the second index

indicates the stress direction. The three diagonal elements (σ_{xx} , σ_{yy} and σ_{zz}) are called normal stresses, whereas the six off-diagonal elements (σ_{xy} , σ_{yx} , σ_{xz} , σ_{zx} , σ_{yz} and σ_{zy}) are called shear stresses. The stress tensor is symmetric ($\sigma_{ij} = \sigma_{ji}$) because of the balance of angular momentum [Greve and Blatter, 2009], i.e. only six of the tensor components are independent. The stress tensor can be decomposed into a deviatoric part $\boldsymbol{\tau}$ and an isotropic part $p\mathbf{I}$:

$$\boldsymbol{\sigma} = \boldsymbol{\tau} - p\mathbf{I} \quad (3.2)$$

with the isotropic pressure $p = -tr(\boldsymbol{\sigma})/3$ (with $tr(\cdot)$ the trace of the tensor) and \mathbf{I} the unity matrix. The first invariant of the deviatoric stress tensor is $tr(\boldsymbol{\tau}) = 0$. The second invariant is defined as $\tau^2 = \frac{1}{2}\tau_{ij}\tau_{ij}$ (using summation convention).

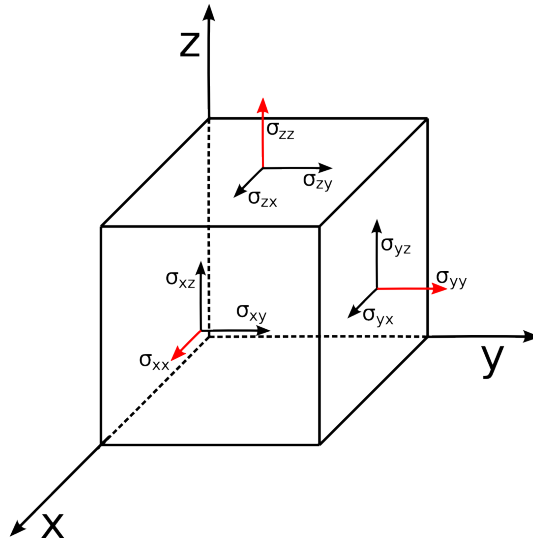


Figure 3.2: Physical meaning of the components of the Cauchy stress tensor.

The strain-rate tensor

The *strain-rate tensor* $\dot{\boldsymbol{\epsilon}}$ describes the rate of deformation of a sample (physical dimension $time^{-1}$) and is calculated from the spatial gradients of the velocity \vec{v} [Cuffey and Paterson, 2010]:

$$\dot{\epsilon}_{ij} = \frac{1}{2} \left(\frac{\partial v_i}{\partial x_j} + \frac{\partial v_j}{\partial x_i} \right). \quad (3.3)$$

Evidently, the strain-rate tensor is symmetric. Analogously to the stress tensor, the strain-rate tensor can be decomposed into a deviatoric part $\dot{\boldsymbol{\epsilon}}$ and an isotropic part $\frac{\dot{\epsilon}_m}{3}\mathbf{I}$:

$$\dot{\boldsymbol{\epsilon}} = \dot{\boldsymbol{\epsilon}} + \frac{1}{3}\dot{\epsilon}_m\mathbf{I} \quad (3.4)$$

with $\dot{\epsilon}_m = tr(\dot{\boldsymbol{\epsilon}})$ corresponding to the change in volume of the sample. For incompressible materials is $\dot{\epsilon}_m = 0$.

Simple shear and pure shear

Two important types of deformation are sketched in Figure 3.3: *simple* and *pure shear*. Pure shear is a special case of deformation, with compression in one direction and extension in a direction perpendicular to the previous one. Considering the two-dimensional example of Figure 3.3, for pure shear is $\dot{\epsilon}_{xx} \neq 0$, $\dot{\epsilon}_{zz} \neq 0$ and $\dot{\epsilon}_{xz} = \dot{\epsilon}_{zx} = 0$ (if incompressible ice, then $\dot{\epsilon}_{xx} = -\dot{\epsilon}_{zz}$). On the contrary, for simple shear other strain components are involved: $\dot{\epsilon}_{xz} = \dot{\epsilon}_{zx} \neq 0$ and $\dot{\epsilon}_{xx} = \dot{\epsilon}_{zz} = 0$. Whereas pure shear is common near the glacier surface, the ice close to the base deforms mainly in simple shear, especially if the glacier is frozen to the bedrock.

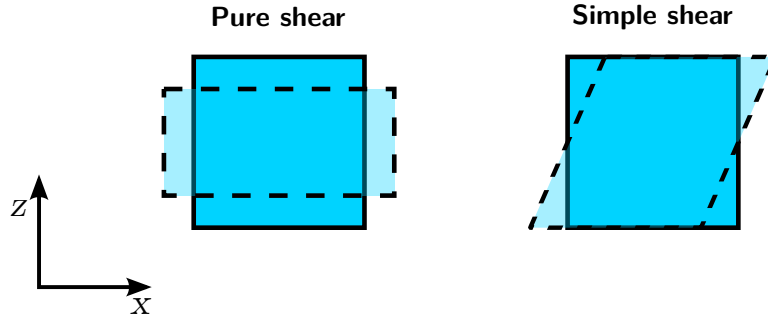


Figure 3.3: Pure and simple shear deformation. Pure shear is common close to the glacier surface, whereas simple shear is frequent close to the base.

3.4 Field equations

3.4.1 Momentum, mass and energy conservation

The consideration of momentum, mass and internal energy balance leads to the following field equations:

- The *Stokes equation* (momentum conservation):

$$\nabla \cdot \boldsymbol{\sigma} + \rho \vec{g} = 0 \quad (3.5)$$

with the stress tensor $\boldsymbol{\sigma}$, the density ρ and the gravitational acceleration \vec{g} . In equation (3.5), the acceleration term $\partial(\rho \vec{v})/\partial t$ is omitted, since not relevant for glaciers dynamics (too slow).

- The *continuity equation* (mass conservation):

$$\frac{\partial \rho}{\partial t} + \nabla \cdot (\rho \vec{v}) = 0 \quad (3.6)$$

with the velocity \vec{v} and t the time variable. For incompressible materials the density is constant ($\dot{\rho} = 0$) and equation (3.6) reduces to $\nabla \cdot \vec{v} = 0$.

- The *temperature equation* (internal energy conservation):

$$\rho C \left(\underbrace{\frac{\partial T}{\partial t} + \vec{v} \cdot \nabla T}_{\text{advection}} \right) = \underbrace{\nabla \cdot (k \nabla T)}_{\text{diffusion}} + \underbrace{\text{tr}(\boldsymbol{\sigma} \dot{\boldsymbol{\epsilon}})}_{\substack{\text{strain} \\ \text{heating}}} + \underbrace{Q_{\text{lat}}}_{\substack{\text{meltwater} \\ \text{refreezing}}} \quad (3.7)$$

with the temperature T , the heat capacity C (see section 3.6), the ice velocity \vec{v} and the thermal conductivity k (see section 3.6). The ice temperature depends on ice advection and heat diffusion with addition of source terms. The heat source term due to internal friction (strain heating or deformational heat) is calculated from the stress tensor $\boldsymbol{\sigma}$ and the strain-rate tensor $\dot{\boldsymbol{\epsilon}}$. The source term Q_{lat} accounts for latent heat released by meltwater refreezing. Note that in this work we calculate the heat flow using the enthalpy formulation introduced by Aschwanden et al. [2012] (see section 3.4.2), which is more convenient than the temperature-based formulation of equation (3.7), if the ice temperature reaches the pressure melting point.

Considering equations (3.5) and (3.6), the ice flow is described by 4 equations (one three-components vector and one scalar equation) with 10 unknown fields (the scalar density, three velocity components and six components of the symmetric stress tensor). The system is therefore highly under-determined [Greve and Blatter, 2009]. The system of equations can be closed considering the *constitutive equation* or *material equation*, which depends on the properties of the creeping material (whereas the field equations are universal) [Greve and Blatter, 2009]. In particular, the constitutive equation gives the relation between the six components of the stress-tensor and the six components of the strain-rate tensor (see equation (3.3) for the relation between strain-rate and velocity). Examples of constitutive equations for glaciers are the Glen’s law (see section 3.5.1) and the firn flow law (see section 3.5.3).

The three field equations (3.5), (3.6) and (3.7) are intimately coupled through density and temperature. According to the continuity equation (3.6) the density evolution depends on the velocity field. But the density influences the velocity field as well. This because density is present as a state variable in the Stokes equation (3.5), in the temperature equation (3.7) and occasionally in the constitutive equation (e.g. considering the firn flow law, see section 3.5.3). Furthermore, the temperature calculated using equation (3.7) influences the flow velocity (see temperature dependence of the creep parameter A in Figure 3.4), and the velocity variable appears in the advection term of the temperature equation too. Finally, the heat capacity C depends on temperature and the thermal conductivity k is dependent on temperature and density (see section 3.6).

3.4.2 Enthalpy transport

In this work, the temperature field of CG is calculated using the enthalpy formulation introduced by Aschwanden et al. [2012]. The enthalpy method was already success-

fully applied on high Alpine glaciers [Gilbert et al., 2014a; ?] and is implemented in Elmer/Ice, the Finite Element software used in this work for the numerical simulations (see section 6.1). The enthalpy method represents an alternative approach to the temperature-based *cold-ice* models, where the temperature is the variable of the differential equation (see equation (3.7)) [Aschwanden et al., 2012].

The enthalpy formulation offers advantages when dealing with temperate ice, since temperature-based models cannot take into account energy content variations due to changes in the solid and liquid fraction at pressure melting point, and are therefore not energy-conserving when temperate ice is present [Aschwanden et al., 2012]. The enthalpy transport is governed by the following equation (same structure as equation (3.7), see also description in section 3.4.1):

$$\rho \left(\frac{\partial H}{\partial t} + \vec{v} \cdot \nabla H \right) = \nabla \cdot (\kappa \nabla H) + tr(\boldsymbol{\sigma} \dot{\boldsymbol{\epsilon}}) + Q_{lat} \quad (3.8)$$

where ρ is the firm density in kg m^{-3} , H the enthalpy variable in J kg^{-1} , \vec{v} the ice velocity field and κ the enthalpy diffusivity (see section 3.6). The last two terms are energy source terms: the strain heating $tr(\boldsymbol{\sigma} \dot{\boldsymbol{\epsilon}})$ and the latent heat Q_{lat} due to refreezing of meltwater.

3.4.3 Free-Surface equation

The topography evolution of the glacier surface is described by the free-surface equation [Greve and Blatter, 2009]:

$$\frac{\partial s}{\partial t} + v_{sx} \frac{\partial s}{\partial x} + v_{sy} \frac{\partial s}{\partial y} - v_{sz} = a_s \quad (3.9)$$

where $s(x, y, t)$ represents the surface elevation, v_{sx} , v_{sy} and v_{sz} the three components of the surface velocity $\vec{v}_s(x, y, t)$, and $a_s(x, y, t)$ the surface snow accumulation (x and y are the horizontal coordinates and t the time). The change in surface elevation is given by the balance between altitude loss due to ice flowing away with velocity \vec{v}_s and altitude gain due to accumulation.

Equation (3.9) can be used for different purposes. If surface velocity field and accumulation are known, the free-surface equation can be used to calculate the surface evolution. In this work the free-surface equation is used differently, namely to calculate the accumulation required to hold the surface elevation in steady state ($\frac{\partial s}{\partial t} = 0$), according to the velocity field calculated with the full Stokes model (see section 7.2).

3.4.4 Dating equation

The age field of the glacier can be calculated considering the age of the ice as a scalar quantity advected with the flow [Zwinger et al., 2007; Elmer/Ice-Wiki, 2017]:

$$\frac{\partial \mathcal{A}}{\partial t} + \nabla \cdot (\mathcal{A} \vec{v}) + \gamma \mathcal{A} = \sigma \quad (3.10)$$

with \mathcal{A} the age of the ice, \vec{v} the velocity field, t the time variable, the source term $\sigma=1$ and the reaction term $\gamma = -\dot{\epsilon}_m$ (with $\dot{\epsilon}_m$ the trace of the strain-rate tensor $\dot{\epsilon}$). For incompressible materials is $\gamma = -\dot{\epsilon}_m = 0$.

3.5 Constitutive equations

3.5.1 Glen's flow law

A well established flow law for isotropic polycrystalline ice is the so-called *Glen's flow law* [Glen, 1955; Nye, 1957; Cuffey and Paterson, 2010]:

$$\dot{\epsilon}_{ij} = A\tau^{n-1}\tau_{ij} \quad (3.11)$$

with $\dot{\epsilon}$ the strain-rate tensor, τ the deviatoric stress tensor, τ the second invariant of τ (see section 3.3), n the *creep exponent* and A the temperature dependent *flow parameter*, also called *creep parameter* or *rate factor*. In Glen's law only deviatoric stresses produce deformation, and no contribution comes from the isotropic pressure p . The viscosity η of a viscous fluid is defined such that $\dot{\epsilon}_{ij} = \frac{1}{2\eta}\tau_{ij}$. Therefore, according to equation (3.11), the viscosity of polycrystalline ice is [Greve and Blatter, 2009]:

$$\eta = \frac{1}{2A\tau^{n-1}} \quad (3.12)$$

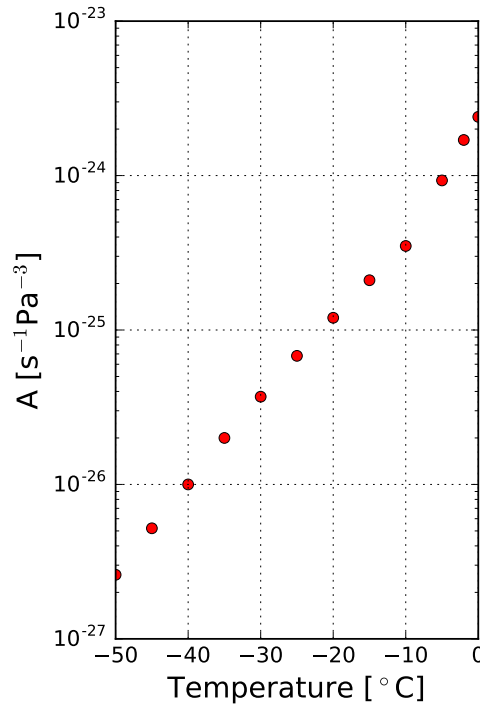


Figure 3.4: Recommended values for the creep parameter A for different ice temperatures. Data taken from Cuffey and Paterson [2010].

For glacier ice the creep exponent n is usually set to $n=3$ [Cuffey and Paterson, 2010]. This implies that the ice viscosity depends on the applied stress and that the flow law is highly non-linear (*power-law*). Such viscous fluids are called *non-Newtonian*, in contrast to Newtonian fluids, like water, where $n=1$ and strain and stress are linearly related. The creep parameter A varies by several orders of magnitude and is mainly dependent on temperature. Recommended values for different ice temperatures are given in Cuffey and Paterson [2010] and plotted in Figure 3.4.

3.5.2 Ice slab model

In this section an exemplary application of Glen’s flow law together with the Stokes and the continuity equation is presented. We consider a simplified geometry of an idealized Alpine glacier, consisting of an ice slab (see Figure 3.5), with inclined parallel surface and bedrock, and with infinite extension in the horizontal x - and y -direction (see Figure 3.5). Further, the glacier is frozen to bedrock (i.e. the velocity is zero at bedrock), and is made of purely incompressible ice ($\nabla \cdot \vec{v}=0$). The glacier thickness h is constant over space and time (steady state).

Due to the infinite horizontal extension, all derivatives with respect to x and y vanish (translational symmetry). Moreover, since the slab is not inclined in y -direction, no deformation occurs in that direction and $\dot{\epsilon}_{yz} = \dot{\epsilon}_{zy} = 0$. Combining the translational symmetry with the incompressibility condition, it follows that:

$$\begin{aligned} \nabla \cdot \vec{v} &= \underbrace{\frac{\partial v_x}{\partial x}}_{=0} + \underbrace{\frac{\partial v_y}{\partial y}}_{=0} + \frac{\partial v_z}{\partial z} = 0 \\ \Rightarrow \frac{\partial v_z}{\partial z} &= 0 \quad \text{and} \quad \dot{\epsilon}_{zz} = 0 \quad . \end{aligned} \quad (3.13)$$

Since the glacier is assumed as frozen to bedrock, from equation (3.13) results $v_z = 0$

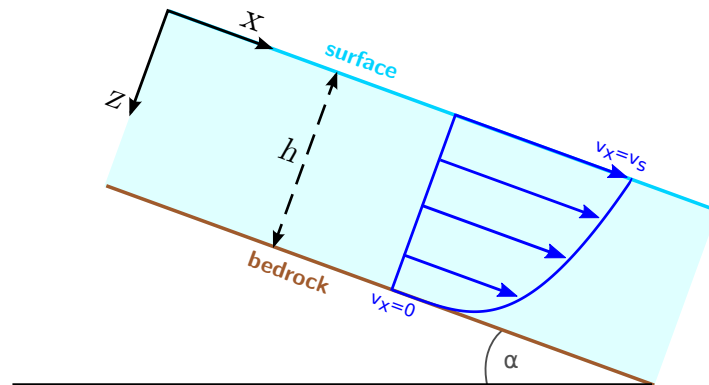


Figure 3.5: Ice slab geometry as simplification of an Alpine glacier. The glacier has infinite extension in x - and y -direction and is frozen to bedrock. The z^4 -profile of the horizontal velocity v_x is sketched in blue.

everywhere, which implies the absence of accumulation. The only non-vanishing strain components are therefore $\dot{\epsilon}_{zx} = \dot{\epsilon}_{xz} \neq 0$. As a consequence of Glen's law (equation (3.11)), also the components of the deviatoric stress tensor are all zero except $\tau_{zx} = \tau_{xz}$. The second invariant of $\boldsymbol{\tau}$ is then $\tau = \tau_{zx}$.

Deploying the Stokes equation (3.5) and considering the inclination α of the ice slab, it follows (note that $\sigma_{zx} = \tau_{zx}$ and $\tau_{zx} = 0$ at the surface):

$$\begin{aligned} \frac{\partial \tau_{zx}}{\partial z} &= -\rho g \sin \alpha & (3.14) \\ \Rightarrow \tau_{zx}(z) &= -\rho g \sin \alpha z \quad . \end{aligned}$$

At this point Glen's law is applied:

$$\begin{aligned} \dot{\epsilon}_{zx} &= A\tau^{n-1}\tau_{zx} & (3.15) \\ \Rightarrow \frac{1}{2} \frac{\partial v_x}{\partial z} &= A(-\rho g \sin \alpha z)^n \quad . \end{aligned}$$

Integrating over the ice thickness and setting the surface velocity to $v_x(0) = v_s$:

$$v_x(z) = v_s + \int_0^z 2A(-\rho g \sin \alpha z')^n dz' \quad (3.16)$$

$$= v_s + 2A(-\rho g \sin \alpha)^n \frac{z^{n+1}}{n+1} \quad . \quad (3.17)$$

With $n=3$ and with the bedrock boundary condition $v_x(h) = 0$, the surface velocity v_s is:

$$v_s = \frac{A}{2} (\rho g \sin \alpha)^3 h^4 \quad . \quad (3.18)$$

Note how v_s depends on the glacier thickness h . The vertical profile of the horizontal velocity has the form:

$$v_x(z) = v_s \left(1 - \left(\frac{z}{h} \right)^4 \right) \quad . \quad (3.19)$$

In Figure 3.5 the z^4 -profile of the horizontal velocity v_x (blue line) is sketched. Since the glacier is frozen to bedrock, shearing is maximal close to the bedrock (simple shear), whereas the vertical velocity gradients are much smaller close to the surface.

3.5.3 Rheology of compressible firn

The compressible firn flow law deployed in this work is based on the work of Duva and Crow [1994], Gagliardini and Meyssonier [1997] and Zwinger et al. [2007]. The strain-rates $\dot{\epsilon}_{ij}$ are calculated from the deviatoric stress components τ_{ij} using the following relation (δ_{ij} is the Kronecker delta):

$$\dot{\epsilon}_{ij} = B\sigma_D^{n-1} \left(\frac{a}{2}\tau_{ij} - \frac{b}{3}p\delta_{ij} \right) \quad (3.20)$$

The *fluidity parameter* B is derived from the creep parameter A in Glen's Law (see equation (3.11)) using the relation $B=2A$, whereas n is the creep exponent. The stress invariant σ_D is calculated using the isotropic pressure p and the second invariant of the deviatoric stress tensor τ (see section 3.3):

$$\sigma_D^2 = a\tau^2 + bp^2 \quad (3.21)$$

The parameters a and b are dependent on the firn relative density $D = \rho/\rho_{ice}$, where ρ is the variable firn density and ρ_{ice} the density of pure glacier ice ($\rho_{ice}=917 \text{ kg m}^{-3}$ [Cuffey and Paterson, 2010]). For high relative densities ($D>0.81$), a and b are determined analytically [Duva and Crow, 1994], whereas for lower relative densities ($D \leq 0.81$) a parametrization is used [Zwinger et al., 2007]:

$$a(D) = \begin{cases} e^{13.22240 - 15.78652 D} & , D \leq 0.81 \\ \left(1 + \frac{2}{3}(1 - D)\right) D^{-2n/(n+1)} & , D > 0.81 \end{cases} \quad (3.22)$$

$$b(D) = \begin{cases} e^{15.09371 - 20.46489 D} & , D \leq 0.81 \\ \frac{3}{4} \left(\frac{(1-D)^{1/n}}{n(1-(1-D)^{1/n})} \right)^{2n/(n+1)} & , D > 0.81 \end{cases} \quad (3.23)$$

Equation (3.22) and (3.23) are visualized in Figure 3.6. At the limit case $D=1$, i.e. if the density reaches the ice density, the parameters converge to $a=1$ and $b=0$. In this

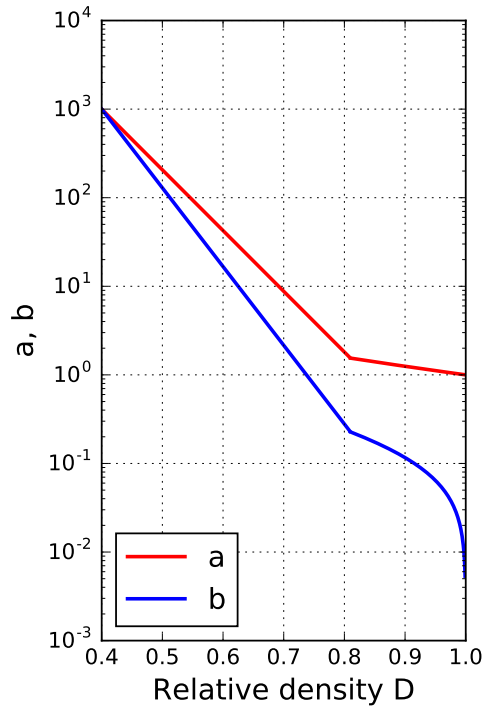


Figure 3.6: The parameters a and b in the firn flow law as function of relative density D (equation (3.22) and (3.23) with $n = 3$).

limit case, the firm flow law (equation (3.20)) reduces to Glen's Law (equation (3.11)).

According to equation (3.20) (and using $tr(\boldsymbol{\tau})=0$), the trace $\dot{\epsilon}_m$ of the strain-rate tensor $\dot{\boldsymbol{\epsilon}}$ is:

$$\dot{\epsilon}_m = -bB\sigma_D^{n-1}p \quad (3.24)$$

which represents the relative volume change of the sample. Note that at the pure ice density $D=1$ it holds $\dot{\epsilon}_m = 0$ (incompressibility). The strain invariant $\dot{\epsilon}_D$ is defined as:

$$\dot{\epsilon}_D^2 = \frac{\dot{\gamma}_e^2}{a} + \frac{\dot{\epsilon}_m^2}{b} \quad (3.25)$$

with $\dot{\gamma}_e^2 = 2\dot{\epsilon}_{ij}\dot{\epsilon}_{ij}$, the second invariant of the deviatoric strain-rate tensor. Further relations between stress and strain invariants are:

$$p = -\frac{1}{b}B^{-\frac{1}{n}}\dot{\epsilon}_D^{\frac{1-n}{n}}\dot{\epsilon}_m \quad (3.26)$$

and

$$\dot{\epsilon}_D = B\sigma_D^n \quad (3.27)$$

Using the relations between invariants (3.26) and (3.27), equation (3.20) can be inverted:

$$\tau_{ij} = 2\eta \left(\dot{\epsilon}_{ij} - \frac{\dot{\epsilon}_m}{3}\delta_{ij} \right) \quad (3.28)$$

with

$$\eta = \frac{B^{-1/n}}{a}\dot{\epsilon}_D^{(1-n)/n} . \quad (3.29)$$

3.5.4 The role of bubble close-off

During the process of densification and transformation from firn to glacier ice, the interstitial air between the ice particles gets enclosed in isolated bubbles. This process is known as bubble close-off [Cuffey and Paterson, 2010] and occurs when approaching the close-off density ρ_c (see section 3.1.2). Further compression and densification reduces the volume of the bubbles and increases the air pressure p_b within the bubbles, making the ice stiffer.

The bubble pressure p_b can be calculated from the state equation of ideal gases and the conservation of mass [Salamatin and Duval, 1997; Lüthi, 2000; Lüthi and Funk, 2000]:

$$\begin{aligned} \frac{p_b(1-D)}{TD} &= \text{const.} \\ \Rightarrow p_b &= \frac{(1-D_c)TD}{(1-D)T_cD_c}p_c \end{aligned} \quad (3.30)$$

with D the relative density (see section 3.5.3), D_c the relative close-off density ($D_c = \rho_c/\rho_i$), T the englacial temperature, T_c the close-off temperature and p_c the close-off pressure. It is evident how the bubble pressure p_b depends on the current state (D

and T), as well as on the conditions during the close-off process (ρ_c , p_c and T_c). Bubble close-off occurs typically at a density of $\rho_c \approx 830 \text{ kg m}^{-3}$ [Cuffey and Paterson, 2010; Schaller et al., 2017], whereas the close-off pressure p_c depends on the mean atmospheric pressure of the study site.

The bubble pressure p_b counteracts the external pressure due to the overlying ice, resulting in a lowered effective pressure. In order to take into account the effect of bubble close-off in the compressible firn flow law, for densities D higher than the close-off density D_c the isotropic pressure p is reduced by the increment of pressure in the bubbles (modified from Lüthi [2000] and Lüthi and Funk [2000]):

$$p_{co} = \begin{cases} p & , \text{ if } D \leq D_c \\ p - p'_b & , \text{ if } D > D_c \end{cases} \quad (3.31)$$

with $p'_b = (p_b - p_c)$. Note that the subscript *co* stays for close-off. Further, according to the modified isotropic pressure, equation (3.20) and (3.21) modify to:

$$\sigma_{D,co}^2 = a\tau^2 + bp_{co}^2 \quad (3.32)$$

and

$$\dot{\epsilon}_{ij,co} = B\sigma_{D,co}^{n-1} \left(\frac{a}{2}\tau_{ij} - \frac{b}{3}p_{co}\delta_{ij} \right) . \quad (3.33)$$

Note that the deviatoric stress tensor $\boldsymbol{\tau}$ is not influenced by the bubble pressure.

At sufficiently high depths the gas molecules are incorporated in the ice crystal lattice (see clathrate hydrates in section 3.1.2), the bubbles disappear and the density reaches the ice density ($D=1$). Obviously, this process is not considered in equation (3.30), where for densities close to the ice density the bubble pressure becomes unrealistic high. The simplified approach outlined in this section is therefore not valid if the relative density gets close to 1.

3.5.5 Anisotropic flow: GOLF

A single ice crystal is much easier to deform along the basal planes, than in the direction of the c -axis (see section 3.2). Therefore, considering anisotropic polycrystalline ice, the preferred orientation of the c -axes has a strong influence on the ice viscosity. According to laboratory tests on ice samples with c -axes pointing in one preferred direction (*single-maximum* fabric), the creep rate may change by more than a factor of 100 depending on the stress direction [Shoji and Langway, 1988].

A widely used flow law to describe the rheology of anisotropic ice is the non-linear General Orthotropic Flow Law (GOLF) [Gillet-Chaulet et al., 2006; Ma et al., 2010], which is also implemented in Elmer/Ice, the Finite Element software used in this work for the ice-flow simulations (see section 6.1). As input, GOLF requires the fabric distribution of the ice, which is described by the second- and fourth-order orientation tensors $\bar{\mathbf{A}}^{(2)}$ and $\bar{\mathbf{A}}^{(4)}$:

$$\bar{\mathbf{A}}^{(2)} = \langle \vec{\mathbf{c}} \otimes \vec{\mathbf{c}} \rangle \quad (3.34)$$

$$\bar{\mathbf{A}}^{(4)} = \langle \vec{\mathbf{c}} \otimes \vec{\mathbf{c}} \otimes \vec{\mathbf{c}} \otimes \vec{\mathbf{c}} \rangle \quad (3.35)$$

with $\bar{\mathbf{c}}$ the c -axis of a single grain, \otimes the dyadic product, and $\langle \rangle$ the average over all grains of the polycrystal, weighted with the volume occupied by the grain in the polycrystal (note that in this section quantities with the overbar symbol are macroscopic quantities averaged over all grains). Since the average over all grains is calculated with a normalized distribution function, $tr(\bar{\mathbf{A}}^{(2)}) = 1$ [Gillet-Chaulet et al., 2006]. In case all c -axes point in z -direction, the components of $\bar{\mathbf{A}}^{(2)}$ are all zero except $\bar{A}_{33}^{(2)} = 1$. As a further example, for isotropic distribution of the c -axes the diagonal elements of $\bar{\mathbf{A}}^{(2)}$ are $\bar{A}_{ii}^{(2)} = 1/3$, whereas all other elements are zero.

The formulation of GOLF reads:

$$\bar{\boldsymbol{\tau}} = \bar{\eta}_0 \sum_{r=1}^3 \left[\bar{\eta}_r tr(\bar{\mathbf{M}}_r \cdot \bar{\boldsymbol{\varepsilon}}) \bar{\mathbf{M}}_r^D + \bar{\eta}_{r+3} (\bar{\boldsymbol{\varepsilon}} \cdot \bar{\mathbf{M}}_r + \bar{\mathbf{M}}_r \cdot \bar{\boldsymbol{\varepsilon}})^D \right] \quad (3.36)$$

with $\bar{\boldsymbol{\tau}}$ the deviatoric stress tensor and $\bar{\boldsymbol{\varepsilon}}$ the strain-rate tensor. The exponent D indicates the deviatoric part of the tensor. The three structure tensors $\bar{\mathbf{M}}_r$ are given by the dyadic product of the three eigenvectors of $\bar{\mathbf{A}}^{(2)}$. The six dimensionless viscosities $\bar{\eta}_r$ and $\bar{\eta}_{r+3}$ (relative to the reference viscosity $\bar{\eta}_0$) are functions of the eigenvalues of $\bar{\mathbf{A}}^{(2)}$ and are calculated deploying μ - M models (micro-macro models). According to Gagliardini et al. [2011], the most realistic polycrystalline response is obtained using the visco-plastic self-consistent models (VPSC) [Castelnau et al., 1996, 1998].

For isotropic fabric, the dimensionless viscosities are $\bar{\eta}_1 = \bar{\eta}_2 = \bar{\eta}_3 = 0$ and $\bar{\eta}_4 = \bar{\eta}_5 = \bar{\eta}_6 = 1$, and equation (3.36) reduces to:

$$\begin{aligned} \bar{\boldsymbol{\tau}} &= \bar{\eta}_0 \sum_{r=1}^3 (\bar{\boldsymbol{\varepsilon}} \cdot \bar{\mathbf{M}}_r + \bar{\mathbf{M}}_r \cdot \bar{\boldsymbol{\varepsilon}})^D \\ &= 2\bar{\eta}_0 \bar{\boldsymbol{\varepsilon}} \end{aligned} \quad (3.37)$$

which corresponds to Glen's law (see equation (3.11) in section 3.5.1) for $\bar{\eta}_0 = \frac{1}{2A}$ and $n=1$.

3.6 Thermal properties of firn and ice

In the present study, the temperature field of the glacier is calculated using the enthalpy method [Aschwanden et al., 2012] (see equation (3.8) in section 3.4.2). The heat flow depends on the thermal properties of the glacier. In this section the relation between temperature and enthalpy is introduced, and the dependencies of the thermal properties of ice and firn are outlined. A summary of the introduced quantities (with the corresponding physical units) is given in Table 3.1. The content of this section is mainly based on the description of the enthalpy method given in Gilbert et al. [2014a].

The enthalpy H is a function of temperature T and water content ω :

$$H(T, \omega) = \begin{cases} \int_{T_0}^T C_p(T) dT & , \text{ if } H < H_f(p) \\ \int_{T_0}^{T_m(p)} C_p(T) dT + \omega L & , \text{ if } H \geq H_f(p) \end{cases} \quad (3.38)$$

with the heat capacity C_p , the latent heat of fusion L , the reference temperature for enthalpy T_0 (here 200 K) and the pressure variable p . The enthalpy of fusion H_f , defined as the enthalpy of temperate ice without liquid water, is given by:

$$H_f(p) = \int_{T_0}^{T_m(p)} C_p(T) dT \quad (3.39)$$

with the pressure melting-point temperature T_m determined using the Clausius-Clapeyron relationship:

$$T_m = T_{prt} - \beta(p - p_{prt}) \quad (3.40)$$

where β is the Clausius-Clapeyron constant, T_{prt} the triple point water temperature and p_{prt} the triple point water pressure. The temperature dependence of the heat capacity C_p is expressed with the following function (T in Kelvin) [Yen, 1981]:

$$C_p = 152.5 + 7.122 T \quad (3.41)$$

The enthalpy diffusivity κ in equation (3.8) is defined as:

$$\kappa = \begin{cases} \frac{k(\rho, T)}{C_p(T)} & , \text{ if } H < H_f(p) \\ \kappa_0 & , \text{ if } H \geq H_f(p) \end{cases} \quad (3.42)$$

with k the thermal conductivity and κ_0 the moisture diffusivity in temperate ice. The dependencies of the conductivity k on temperature and density are decoupled in multiplicative factors:

$$k(\rho, T) = \frac{k_{ice}(T)}{k_{ice}(T_{ptr})} k(\rho) \quad (3.43)$$

where (ρ in kg m^{-3}) [Calonne et al., 2011]:

$$k(\rho) = 2.5 \cdot 10^{-6} \rho^2 - 1.23 \cdot 10^{-4} \rho + 0.024 \quad (3.44)$$

and (T in Kelvin) [Cuffey and Paterson, 2010]:

$$k_{ice}(T) = 9.828 \exp(-5.7 \cdot 10^{-3} T) \quad (3.45)$$

assuming that firn and ice have the same temperature dependence.

Table 3.1: Summary of the quantities introduced in this section and required for the enthalpy method, with the respective symbol, unit and numerical value (if fixed constant). Modified from Gilbert et al. [2014a].

Quantity	Symbol	Values and units
Clausius-Clapeyron constant	β	$9.7456 \cdot 10^{-8} \text{ K Pa}^{-1}$
Ice heat capacity	C_p	$\text{J kg}^{-1} \text{ K}^{-1}$
Enthalpy	H	J kg^{-1}
Enthalpy of fusion	H_f	J kg^{-1}
Firn/ice conductivity	k	$\text{W K}^{-1} \text{ m}^{-1}$
Latent heat of fusion	L	$3.34 \cdot 10^5 \text{ J kg}^{-1}$
Pressure	p	Pa
Pressure of water triple point	p_{prt}	$6.11 \cdot 10^2 \text{ Pa}$
Firn/ice temperature	T	K
Reference temperature for enthalpy	T_0	200 K
Temperature of water triple point	T_{prt}	273.16 K
Pressure melting point temperature	T_m	K
Enthalpy diffusivity	κ	$\text{kg m}^{-1} \text{ s}^{-1}$
Moisture diffusivity	κ_0	$1.045 \cdot 10^{-4} \text{ kg m}^{-1} \text{ s}^{-1}$
Firn density	ρ	kg m^{-3}
Water content	ω	-

4 Field measurements (2014–16)

The CG glacier saddle has been subject to ice-core studies since the 1970s [Wagenbach et al., 2012], therefore the amount of available field measurements is very broad. In the frame of this work three field campaigns were carried out in September 2014, September 2015 and September 2016, mainly focusing on the area in the vicinity of the drilling sites KCC and KCI (see Figure 4.1). Measurements gathered within this work are summarized in this chapter: horizontal surface velocities (section 4.1), surface topography (section 4.2) and borehole inclination angles (section 4.3). In addition, measured surface accumulation data are presented in appendix A.2. Primary purpose of the measurements is to provide new data to run and validate the full Stokes model presented here.

4.1 Horizontal surface velocities

Surface velocity measurements are mandatory to validate surface velocities calculated with the full Stokes model. A conventional method to measure surface flow velocities of glaciers consists in installing markers, such as aluminium stakes, on the glacier surface and surveying their successive position changes afterwards [Gudmundsson, 1994; Zwinger et al., 2014]. Measuring flow velocities of order 1 m a^{-1} , as it is the case at CG, requires to determine the position of the stakes with cm-scale accuracy. This is possible with infrared distance meter or differential GPS (DGPS) [Haeberli et al., 1988; Lüthi, 2000; Vincent et al., 2007a].

Previous measurements at CG (1980–1999)

First measurements of the surface velocity field at CG are documented in Haeberli et al. [1988]. The stakes were installed on a regular grid in the central saddle area in August 1980 and their position was remeasured in 1981. At locations with lower accumulation the stakes could be resurveyed in 1982, 1983, 1985 and 1987. After 1987, further campaigns were performed covering different parts of the saddle:

- In the period 1989–1990 stake position measurements covered the northern part of the saddle and the region close to the western outflow towards Grenzletscher [Wagner, 1996].
- In 1995 stakes were installed along the flowline connecting the drilling positions of the ice cores KCH and KCS drilled in 1995, and the ice core CC of 1982 [Lüthi, 2000; Lüthi and Funk, 2000].
- Stakes installed in 1998 covered the KCH-KCS flowline as well, however with more focus on the catchment area [Keck, 2001].

Observed surface flow velocities in the period 1980–1999 are summarized in Figure 4.1.

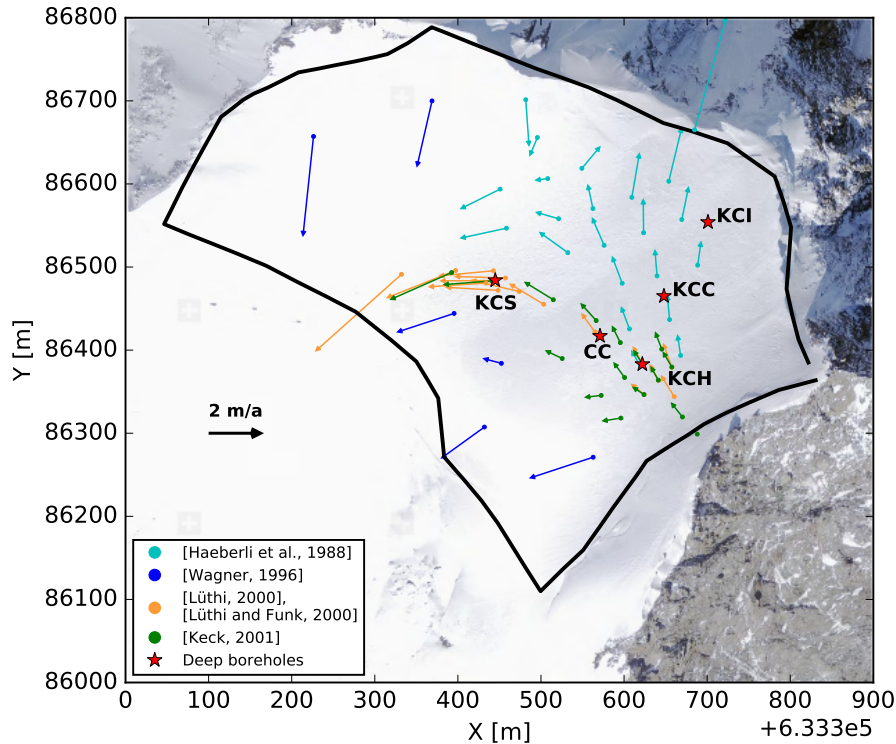


Figure 4.1: Surface velocities measured at CG in the period 1980–1999 based on stake position measurements. Reported stakes were surveyed in the years 1980–81 (in places of low accumulation 1980–87) [Haeberli et al., 1988]; 1989–90 [Wagner, 1996]; 1995–96 [Lüthi, 2000; Lüthi and Funk, 2000] and 1998–99 [Keck, 2001]. Coordinates are in the official Swiss coordinate system. Areal imagery from <https://map.geo.admin.ch>.

Measurements in the 2014–2016 period

Within this work, a new series of surface velocity measurements was started in September 2014. The positions of the 20 newly installed stakes are presented in Figure 4.2 as blue dots. Main objectives of the new measurements are:

- To characterize the flow pattern in the area surrounding the KCC and KCI drilling sites and along the flowline linking both sites.
- To constrain surface velocities in the eastern part of the glacier, where no data are available from previous investigations.
- To remeasure flow velocities along the KCH-KCS flowline to evaluate the stationarity of the ice flow, by comparison with measurements from the period 1995–1999.

In September 2015 the positions of only 13 stakes could be resurveyed. Some stakes could not be found due to an unusual high snow accumulation. Three stakes close

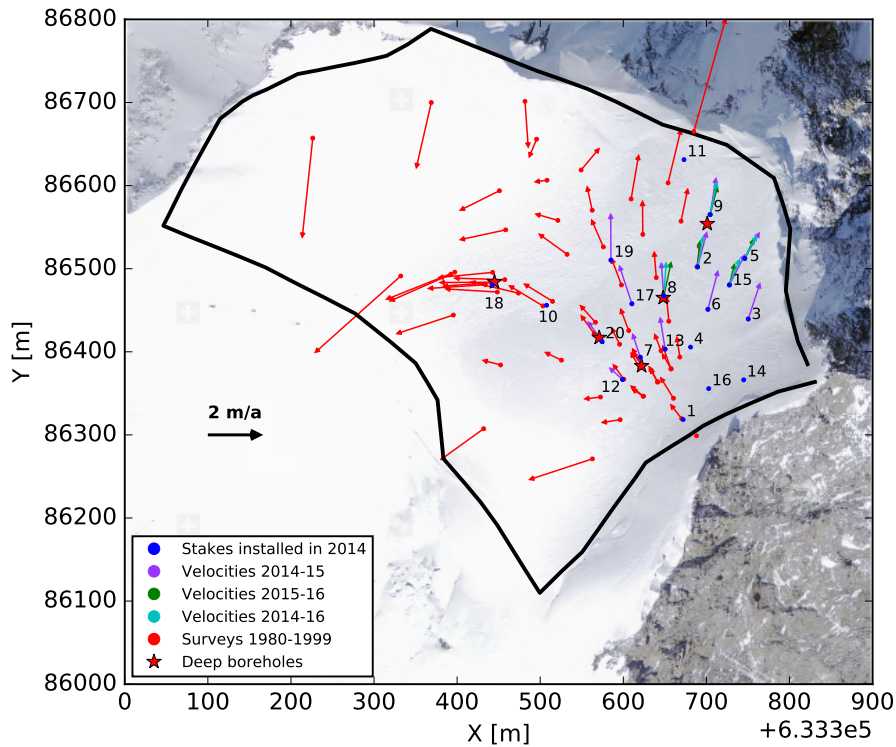


Figure 4.2: Surface velocities measured at CG in the period 2014–2016 (violet, green and cyan arrows) compared with measurements of the period 1980–1999 (red arrows). The blue dots represent the position of all the stakes installed in 2014. Some stakes (1, 16, 14, ...) got lost and could not be resurveyed in 2015.

to the bergschrund were also lost, probably not submerged by snow, but more likely pulled down by wind. A single stake very close to the ice cliff could not be measured, because it was out of view of the surveying system. In September 2016 only five stakes were still visible. Flow velocities measured in the period 2014–2016 (Figure 4.2) are consistent with measurements of the period 1980–1999. The accompanying values and their uncertainties can be found in Table A.1, A.2 and A.3 (appendix A.1).

Measuring methods

The position of the stakes are surveyed combining a Leica TPS1100 total station (electronic theodolite integrated with an infrared distance meter with prism reflector) with a DGPS. The Leica station was positioned close to the saddle point of the glacier, slightly on the slope towards Zumsteinspitze, and high enough to have a wide view on all the stakes on the southern part of the glacier. Stake positions are determined using the following procedure:

- Measure the relative positions of all the stakes with respect to the Leica station by positioning the prism reflector on top of each stake.
- Measure the absolute position of a few stakes a second time using the DGPS.

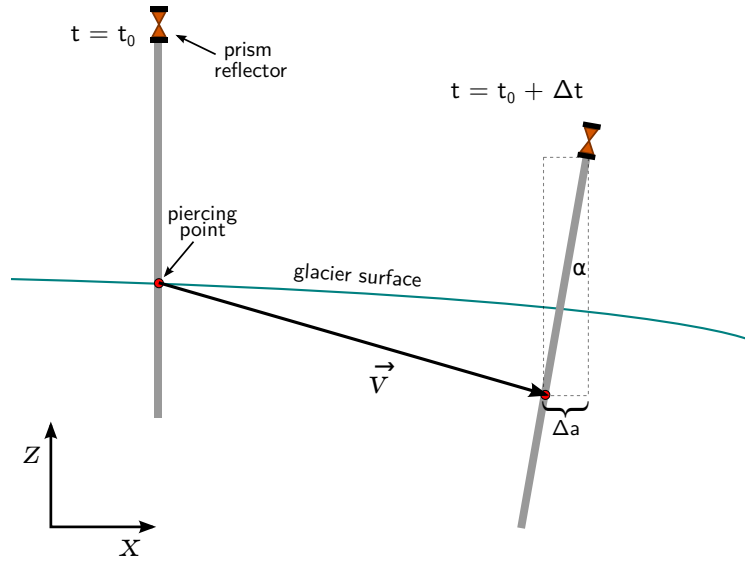


Figure 4.3: Principle of surface velocity measurements using stakes as marker. The marker, tracked between $t = t_0$ and $t = t_0 + \Delta t$, is the initial intersection point (piercing point) between stake and glacier surface (red dot). The stakes tend to incline in the direction of flow (tilt angle α). The positions measured with the prism reflector on top of the stake need to be corrected, subtracting the displacement Δa .

- Rotate and translate the Leica coordinate frame into the official Swiss coordinate system.
- Correct the evaluated position taking into account the inclination of the stakes (angle α in Figure 4.3).

The stakes measured a second time with the DGPS serve as reference to anchor all measurements to an absolute coordinate system. Since this procedure is highly time consuming if cm-scale accuracy is required, only few stakes were surveyed with the DGPS. Rotation angle and translation vector for the transformation from the Leica frame into the official Swiss coordinate system are estimated by minimizing the discrepancy between the transformed positions of the reference stakes measured with the Leica station, and the absolute positions measured with the DGPS. Due to vertical gradients of the ice-flow velocity, the stakes tend to get inclined in the direction of flow, thus producing a potential overestimation of the flow velocities (see the displacement Δa in Figure 4.3). For inclined stakes, the tracked marker is the initial intersection point between stake and glacier surface in September 2014 (see red dot in Figure 4.3).

Error estimation

The position of the stakes is measured with an uncertainty of 15 to 30 cm. The accuracy of the measurements is limited by the following uncertainties (1σ):

- Accuracy of the infrared distance meter within the Leica station: $\mathcal{O}(1\text{ cm})$.

- Accuracy of the DGPS: $\mathcal{O}(1 \text{ to } 80 \text{ cm})$ depending on measuring time.
- Out of plumb positioning of the prism reflector mounting: $\mathcal{O}(10 \text{ cm})$.
- Oscillations of the stake during the survey due to wind forcing: $\mathcal{O}(10 \text{ cm})$.
- Error of the stakes inclination angle: 3° a^{-1} (arbitrarily chosen).

Uncertainties in the measured stake position due to the points listed above are estimated from the mean residual discrepancy between transformed and absolute positions of the respective reference stakes. Compared to the other uncertainty sources, the error derived from the accuracy of the infrared distance meter is negligible. No stake inclination measurements are available for the period 2014–2016. The inclination of the stakes is estimated assuming for all stakes perfect perpendicular initial positioning and successive $5^\circ \pm 3^\circ \text{ a}^{-1}$ inclination in the direction of flow. The inclination rate is arbitrarily chosen, referring to previous measurements in 1995–1996 [Lüthi, 2000] and 1998–1999 [Keck, 2001; IUP glaciology group database], where the measured stakes inclination rate was less than 8° a^{-1} . The total uncertainty of the velocity measurements is calculated using Gaussian error propagation.

Discussion of the surface velocity measurements

If compared with previous measurements made in the 1980s and 1990s, surface velocities measured in the frame of this work show no dramatic changes in the flow regime of the glacier (see Figure 4.2). Looking at specific stakes, the flow direction measured at stake 19 could suggest a slightly enhanced flow towards the east. However, since this is the only stake showing this trend, it is not enough for asserting changes in the flow regime of the glacier.

On a shorter time scale, surface velocities measured in the period 2014–2015 are significantly higher, about 20–30%, than velocities measured the year after. This observation is consistent with the two to three times higher surface snow accumulation registered in the period 2014–2016 (see Table A.4 in appendix A.2), since deformation occurs faster for a thicker layer of low density firn. Measurements at stake 8 show short term changes in the flow direction. However, since the stake was partly dug out in September 2015 and 2016 in order to access the KCC borehole, it cannot be excluded that the inclination of the stake was changed by accident (e.g. away from the flow direction), resulting in a change of the evaluated displacement.

Looking at Table A.1, A.2 and A.3 in appendix A.1, surface velocities measured in the period 2014–2015 are affected by a slightly larger uncertainty ($\sim 25\%$) compared to measurements of the following year ($\sim 17\%$). The main reason for that is the shorter measuring time of the reference stakes in 2014 using the DGPS. Further, uncertainties in y -direction (to the north) are larger than in x -direction (to the east). This is due to the poorly known stake inclination angles: the measured ice flow is prevailing northwards, inducing enhanced stakes inclination in y -direction rather than in x -direction, thus producing larger uncertainties in y -direction.

4.2 Surface topography

Topography measurements are important to define the glacier geometry used as input for the full Stokes model. The glacier surface topography was surveyed three times in the period 2014–2016 with focus on the area surrounding the ice cores drilling positions. The recorded surface tracks are presented in Figure 4.4. Measurements were made in parallel to the stake measurements (see section 4.1) with the Leica TPS1100 station, by walking from stake to stake, carrying the prism reflector mounted on a long vertical pole in the hand. The transformation from the Leica coordinate frame into the official Swiss coordinate system is performed using the same rotation angle and translation vector as used for the evaluation of the stakes positions presented in section 4.1.

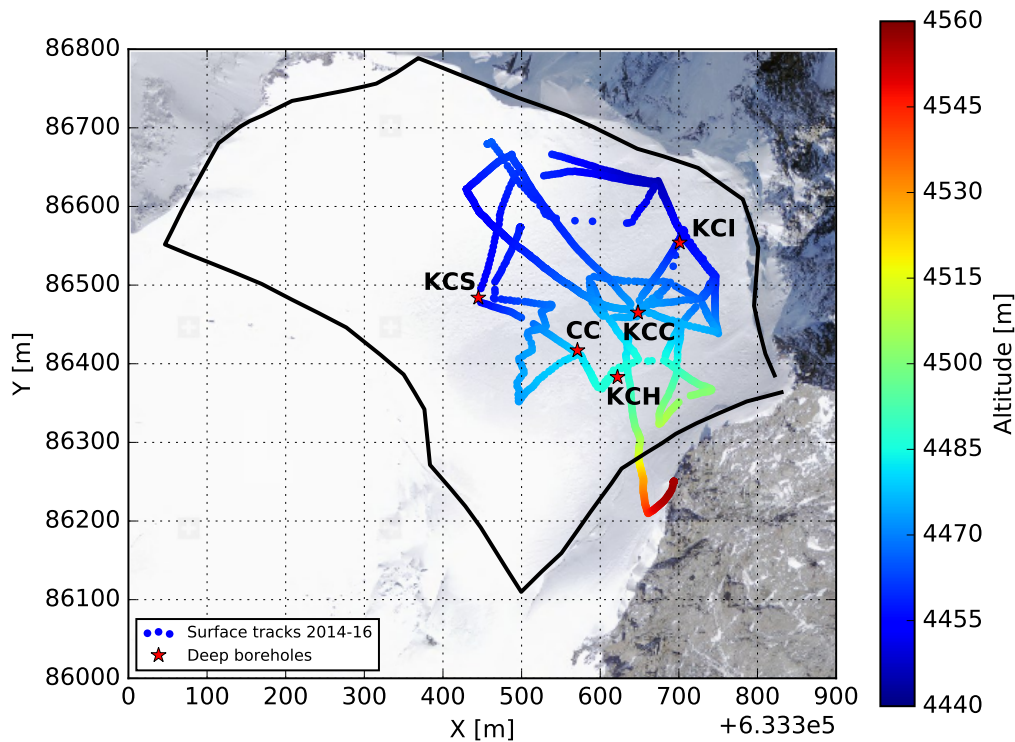


Figure 4.4: Surface topography measurements. Tracks recorded in the period 2014–2016 are mainly concentrated in the central region of the glacier.

Error estimation

In addition to the uncertainty sources listed in section 4.1 for the static stake positions, the accuracy of the horizontal positions of the track surface points is limited by oscillations of the prism reflector on top of the pole. This is inevitable while walking on the glacier surface. Accounting for this, the total horizontal error is estimated to be 50 cm in each horizontal direction. The vertical positioning error of the measured surface points is influenced by:

- The accuracy of the infrared distance meter within the Leica station: $\mathcal{O}(1\text{ cm})$.

- The uncertainty in the vertical position of the reference stakes measured with the DGPS¹: $\mathcal{O}(1 \text{ to } 130 \text{ cm})$, which depends on the measuring time, and which is generally larger than in the horizontal directions.
- Vertical oscillation of the hand held prism reflector while walking on and sinking in the snow: $\mathcal{O}(20 \text{ cm})$.

Since uncertainties due to the accuracy of the infrared distance meter are negligible and vertical oscillations attenuate after surface interpolation, the uncertainty of the measured surface elevation is mainly limited by the uncertainty of the vertical position of the reference stakes. Analogously to the error estimation for the horizontal positions of the stakes outlined in section 4.1, the vertical uncertainty of the surface points is estimated as the mean discrepancy between translated altitudes measured with the Leica station and altitudes measured with the DGPS. The calculated vertical error is of order 50 cm.

Surface elevation changes

Surface elevation changes in the period 2014–2016 are estimated comparing the altitudes of single surface points measured in different years, if their horizontal distance is shorter than 2 m. The observed elevation variations are of order 1 m, therefore quite small compared to the measurement error (0.5 m). Nevertheless, the data show evidences for a surface elevation gain of a bit more than 1 m (0.5 to 1.8 m) from September 2014 to September 2015, and thereafter an elevation loss of a bit less than 1 m (0.2 to 1.4 m) until September 2016. This observation is consistent with snow accumulation changes measured at CG over the same timespan using stakes (see Table A.4 in appendix A.2), which show a much higher snow accumulation between September 2014 and September 2015, than in the following year.

While surface topography measurements made in 1989 [Wagner, 1996] and in 1996 [Lüthi, 2000; Lüthi and Funk, 2000] gave no evidence of a substantial change (within the uncertainty of 0.5 m [Lüthi, 2000]), compared to these prior data our measurements suggest a surface elevation gain of $\sim 5 \text{ m}$ (4 to 6 m) in the last 20 years. Although systematic biases due to different evaluation methods cannot be excluded (for example the assumed Geoid Height for the evaluation of the altitudes of the reference stakes using the DGPS), this gain is consistent with the warmer meteorological conditions today compared to the end of last century (see the rising trend of the englacial temperatures in the Monte Rosa area documented in Hoelzle et al. [2011]). Warmer atmospheric conditions facilitate firn compaction at surface and reduce the efficiency of wind erosion, thus increasing the amount of net snow accumulation. With a twice higher accumulation in the period after 1977 as compared to the period 1901–1977, evidences for enhanced surface accumulation at CG in the last decades resulted from the analysis of the ice core KCI as well [Bohleber, 2008]. More about surface elevation changes at CG on a longer time scale is discussed in section 5.1.2.

¹Assumed Geoid Height (52.24 m) after Rapp [1997] and taken from <https://www.unavco.org/software/geodetic-utilities/geoid-height-calculator/geoid-height-calculator.html>

4.3 Borehole inclination angles

The shape of a borehole drilled in the ice evolves with time according to the flow of the surrounding ice. Therefore, borehole inclination measurements provide direct information of the glacier dynamics. For example, assuming simple shear in x-direction and neglecting horizontal velocity gradients (only non-zero strain components: $\dot{\epsilon}_{xz} = \dot{\epsilon}_{zx} = \partial v_x / \partial z$), the borehole tilt rate $\dot{\alpha}$ is directly correlated with the vertical gradient of the horizontal velocity v_x : $\tan(\dot{\alpha}) = \partial v_x / \partial z$ [Cuffey and Paterson, 2010].

At CG, first borehole inclination measurements were performed in the KCS borehole several times between 1996 and 1997 [Lüthi, 2000; Lüthi and Funk, 2000]. In my work, borehole inclination angles were measured at KCC (in 2016) and at KCI (in 2015 and 2016). In section 7.1.4 measured inclinations are compared with inclination angles derived from the full Stokes model.

Measuring methods

The deployed inclinometer probe, the DIgital BOrehole Sensor System DIBOSS, was made available by the VAW (Versuchsanstalt für Wasserbau, Hydrologie und Glaziologie), ETH Zürich. More details about DIBOSS and the inclinometer calibration procedures can be found in Ryser [2014] and Ryser et al. [2014]. The probe is equipped with additional sensors for pressure and temperature. However, for the measurements at CG only the inclinometer and the magnetometer were deployed. The probe is inserted into an aluminium pipe with smoothed extremities in order to minimize the risk to get stuck in the borehole. It is preferable to use a longer pipe to favor the positioning of the probe to be as parallel as possible with respect to the borehole. In addition, long pipes allow to measure averaged angles and avoid to detect insignificant short scale inclination variations. Nevertheless, the pipe has to be short enough to pass through strongly bent and highly deformed borehole segments.

For the measurements at CG in September 2016 the pipe length was decided to be 60 cm, whereas in September 2015 the pipe was 2 m long. In addition, for a better positioning of the probe in the borehole, the 60 cm aluminium pipe was equipped with two centralizers (manufactured by the IUP mechanical workshop, see Figure 4.5, left). The probe is arranged inside the pipe and hangs on a long cable, which has the multi function of mechanical support, ribbon, and live data transfer to the surface. The probe is slowly let down into the borehole using a tripod with a pulley (see Figure 4.5, right). Borehole angles are measured every 5 m depth, downwards from top to bottom and upwards from bottom to top of the borehole. The actual depth of the probe is estimated using the length markers of the cable.

Results

Inclination angles measured at the borehole KCC in September 2016, three years after drilling, are presented in Figure 4.6, whereas angles measured at KCI in September 2015 and 2016, respectively ten and 11 years after drilling, are shown in Figure 4.7. The borehole KCC was completely measured down to the bottom. In contrary at KCI, due to too strong borehole deformation, measurements were possible only down to ~ 50 m,

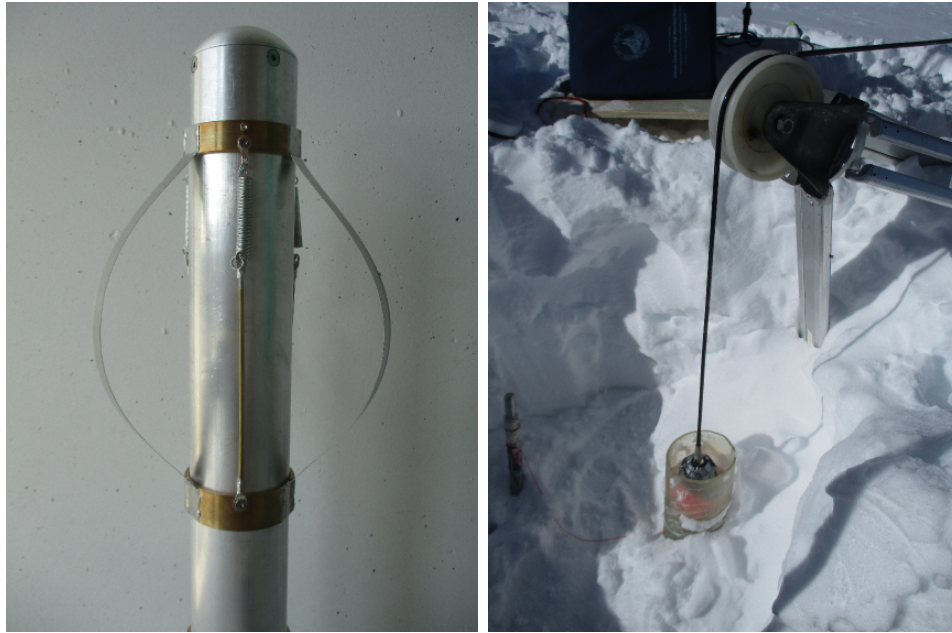


Figure 4.5: The inclinometer probe. Left: single centralizer fixed at the aluminium pipe. The inclinometer probe is allocated inside the pipe. Right: operation of the inclinometer probe in the field. The probe is let down using a tripod with pulley. Raw data are instantly transferred to the surface.

whereas the KCI core length is 62 m [Bohleber et al., 2013]. The considered inclination angles are given with respect to the plumb line. Blue and cyan markers in Figures 4.6 and 4.7 identify downwards measurements, red and yellow markers upwards measurements.

Data quality

The quality of the inclination measurements is estimated by evaluating the orientation of the probe during the measurements, using the magnetometer integrated in the probe. Orientation angles measured at KCC and KCI are presented in appendix A.3 (Figure A.1 and A.2). Considering the close to northwards surface flow directions measured at KCC and KCI (see section 4.1), both boreholes, moving from the top to the bottom, are expected to be approximately oriented southwards. Orientation angles differing in a significant way from the expected southwards orientation indicate a mispositioning of the probe inside the borehole. Therefore, inclination angles with corresponding unreliable orientation angles are eliminated from the dataset (transparent markers in Figure 4.6).

Error estimation

Uncertainties in the inclination measurements are dominated by mispositioning of the probe inside the borehole. In comparison to that, the influence of the sensor resolution is negligible. The maximal error is estimated by means of geometrical considerations,

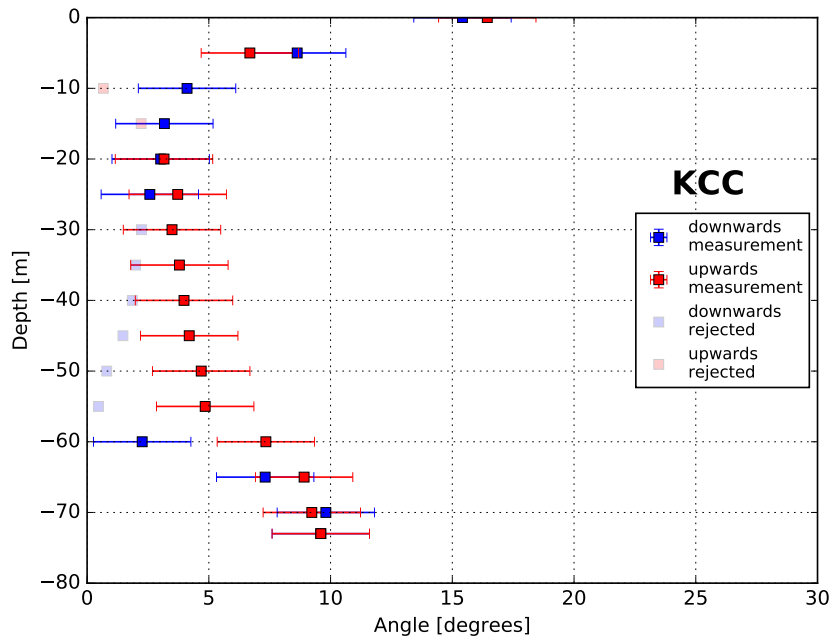


Figure 4.6: Measured inclination angles at KCC in September 2016, i.e. ~ 3 years after drilling. A few measurement points are eliminated from the dataset due to unrealistic orientation angles (transparent markers), indicating mispositioning of the probe (see text and Figure A.1).

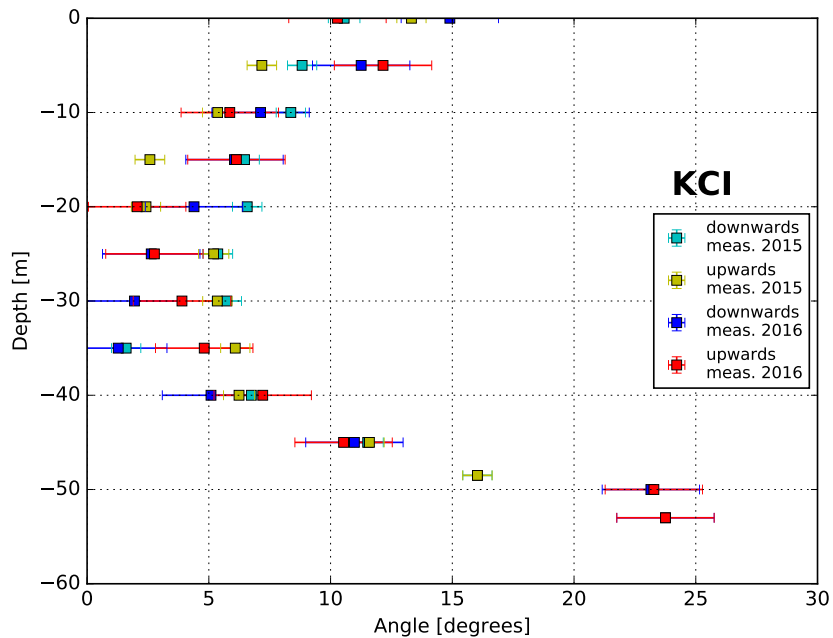


Figure 4.7: Measured inclination angles at KCI in September 2015 and 2016, i.e. ~ 10 and ~ 11 years after drilling. A sharp bend of the borehole hampered the inclinometer probe to reach depths deeper than 53 m.

calculating the maximal possible inclination of the aluminium pipe with respect to the borehole. From a pipe diameter of 6 cm, pipe length of 60 cm and original borehole diameter of 12 cm (no borehole closure measurements available), it results a maximum inclination error of 5.7° (3σ). For the 2 m long aluminium pipe, the maximum mispositioning angle is 1.7° (3σ). Errorbars shown in Figure 4.6 and 4.7 are 1σ -errors.

Discussion of borehole inclination measurements

As expected, the shape of the boreholes is most inclined close to the surface, due to rapid changes in the firn density, and at the bottom of the borehole, since the glacier is frozen to bedrock and flow velocities must drop to zero. The measurements show significantly larger angles in the bottom region of KCI, compared with the bottom region of KCC. This is expected since the borehole KCI is much older than the borehole KCC (in 2016 the borehole KCI is 11 years old, whereas the borehole KCC is only 3 years old). The deformation in the bottom region of the KCI borehole is so strong, that even with the 60 cm aluminium pipe it was not possible to access the last 10 m above bedrock. However, despite their age difference, the KCC and the KCI borehole show a similar inclination profile (about 5°) at medium depths. This observation suggests a governing flow field with low vertical gradients of the horizontal flow velocities at depths far from surface and bedrock.

Inclination angles of the borehole KCI were measured twice, in 2015 and in 2016. Errors of the measurements in 2015 are smaller, since a 2 m long pipe instead of 60 cm was used. However, due to the large measuring errors, it is not possible to clearly identify an increase of inclination after one year. In order to measure temporal inclination changes of boreholes more precisely, it would be more convenient to use permanently installed tilt meters [Gudmundsson et al., 1999; Lüthi and Funk, 2000; Ryser et al., 2014], where the measuring error due to the positioning of the probe inside the borehole would not be repeated at each measurement.

Measuring errors of the inclination angles are dominated by the mispositioning of the inclinometer probe inside the borehole. The discrepancy between downwards and upwards measurements, which are expected to be equal at equal depths, emphasizes this problem. In general upwards measurements are expected to be more accurate than downwards measurements, since pulling up the probe using a cable anchored on the top facilitates its positioning parallel to the borehole walls. In contrast, downwards measurements are less reliable, since the probe is likely to lean with only one extremity on the borehole side wall, if pushed down only under its own weight. This possibility is confirmed by orientation measurements shown in Figure A.1 and A.2, since most of the unreliable data eliminated from the dataset are measured downwards. Furthermore, larger angles are easier to measure, since it is more likely for the inclinometer probe to lean on the borehole wall with both extremities, and therefore to lie parallel to the borehole. Inclination measurement at KCI are therefore more reliable than at KCC. This possibility is confirmed by the orientation measurements shown in Figure A.1 and A.2: most of the data rejected due to unrealistic orientation of the probe are measured at KCC and at relative depths where inclination angles are expected to be very small.

5 Ice-flow modeling of Colle Gnifetti

Input data, assumptions and procedures used within this work to build and run the full Stokes model of CG are presented in this chapter. The defined glacier geometry, i.e. surface and bedrock Digital Elevation Model (DEM), is introduced in section 5.1. Details about the mechanical and thermodynamic boundary conditions of the model are described in sections 5.2 and 5.3. Finally, in section 5.4 I discuss how the field equations outlined in chapter 3 are combined within the model in order to get a fully thermo-mechanically coupled solution.

5.1 Glacier geometry

5.1.1 Glacier sectors

A north-oriented aerial imagery of CG is presented in Figure 5.1. The saddle is spanned between Signalkuppe in the south, with the Margherita Hut on top, and Zumsteinspitze in the north. The investigated area is situated within the thick black lines in Figure 5.1. The boundaries freely follow the geometry already used in Lüthi [2000] and Lüthi and Funk [2000]. The study area is divided into five sectors, aiming to simplify the presentation in the next sections:

- The **central region** (sector 1): the sector representing the main subject of interest in this study, since it includes all drill sites and offers a rather high spatial density of measurements.
- The **ice cliff** (sector 2): the area contiguous to the ice cliff, which governs the outflow of the KCC and KCI drill sites towards the east.
- The **GG-outflow** (sector 3): the area, which governs the outflow towards Grenzgletscher, and which is confined downstream by a big crevasse.
- The **northern half** (sector 4): the northern side of the saddle below Zumsteinspitze. The majority of the measurements of this area was done in the 1990s.
- The **southern edge** (sector 5): an area for which sensitivity studies (modifying bedrock and surface DEM) suggest only marginal influence on the flow behaviour of the glacier.

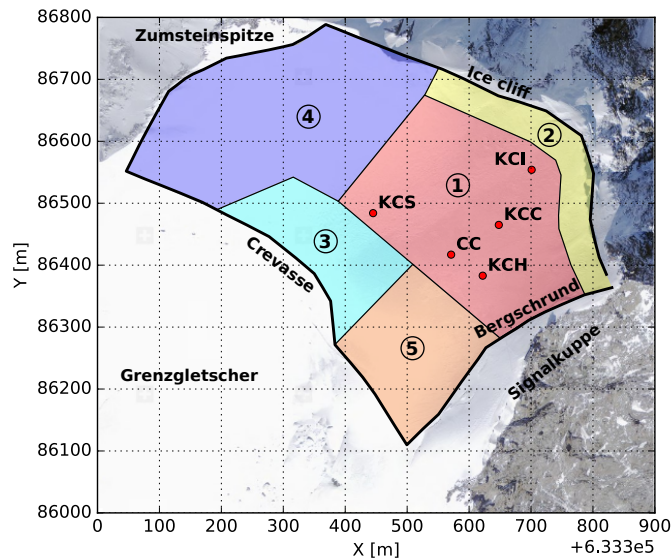


Figure 5.1: Map of the CG saddle. By reason of simplicity, the investigated area is partitioned into five sectors (see text). The boundaries follow the geometry already used in [Lüthi, 2000] and Lüthi and Funk [2000]. Coordinates are in the official Swiss coordinate system. Areal imagery from <https://map.geo.admin.ch>.

5.1.2 Stationarity

In this study the glacier geometry is assumed to be in steady state. This assumption is corroborated by previous studies [Haeberli et al., 1988; Wagner, 1996; Lüthi, 2000; Lüthi and Funk, 2000; Konrad et al., 2013]. The surface topography of CG was surveyed several times in the past, thus allowing a quantitative estimation of possible elevation changes. Geodetic measurements show a lowering of the surface altitude of 3 m during the period 1980–89 [Wagner, 1996], whereas no notable changes were observed in the period 1989–96 [Lüthi, 2000]. Surface topography measurements performed in the frame of this work (2014–2016) suggest a gain in surface elevation of about 5 m compared to the surveys of 1996 (however it cannot be excluded that this gain in ice mass is at least partly due to an artificial elevation offset between the recent and the 1996 measurements, see section 4.2). On a longer time scale, the comparison of the current glacier geometry with a picture of August 1893 [Mosso, 1899] shows no dramatic changes [Haeberli et al., 1988; Wagner, 1996]. Considering the tremendous retreat and mass loss over the last roughly 20 years of other Alpine glaciers located at lower elevations [Braithwaite et al., 2013; Vincent et al., 2017], CG has shown until now robustness with respect to mass loss against recent atmospheric temperature changes [Böhm et al., 2010] (however, with evident warming of englacial temperatures [Hoelzle et al., 2011]). This is in accordance to what is observed at the very high-elevation Mont Blanc glaciated areas which, similar to CG, are situated well above 4000 m a.s.l.. Namely, in the Mont Blanc area climate

warming had an impact on englacial temperatures [Vincent et al., 2007b], but produced only small ice thickness changes (on average less than 3 m between 1905 and 2005 [Vincent et al., 2007a]). All these findings support the steady state assumption for the present modeling study.

5.1.3 Surface topography

The surface topography used as input in the numerical model is represented in Figure 5.2. Table 5.1 offers an overview of data and methods used to estimate the surface DEM for each glacier sector. At locations where surface measurements are too sparse or totally missing, the surface topography is (necessarily) manually estimated, as generally done when lack of direct measurements exists. The estimation is performed by minimizing the discrepancy between (a) measured surface flow velocities and velocities calculated with the full Stokes model, and (b) measured and calculated accumulation rates (see validation of the model results in section 7.1.1 and 7.2).

In the central region, the best documented part of the glacier, the reconstructed topography is cubically interpolated from measurements performed between 2014 and 2016. Surface elevations of the ice cliff area are not supported by direct measurements at all and are therefore manually estimated, as outlined above. This area is of fundamental importance since governing the outflow across the ice cliff of the flowline comprehending the KCC and KCI drilling sites. The surface topography of the northern half of the glacier and of the GG-outflow sector is obtained from the elevation model used in

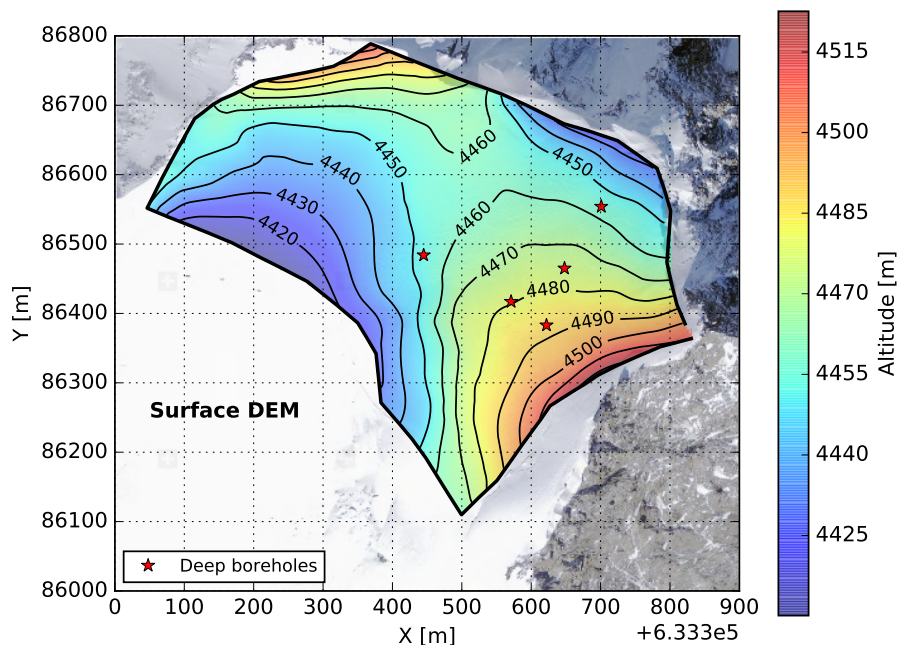


Figure 5.2: Surface DEM used as input in the numerical model. The topography of the area surrounding the ice-core drilling sites is based on surveys of the period 2014–2016.

[Wagner, 1996], Lüthi [2000] and Lüthi and Funk [2000], and completed by manual estimation (see above) at the boundaries. In contrary, the topography of the southern edge is entirely manually estimated based on photographs. This sector is the least known part of the glacier. However, note that the validity of the model is not compromised, since the topography of the southern edge only influences the flow behaviour of the whole glacier in a marginal way (see section 5.1.1).

Table 5.1: Summary of data sources used to estimate the surface DEM for the glacier sectors defined in section 5.1.1 (see also Figure 5.1). For “manual estimation” see text.

Sector	Surface DEM based on:
1	Leica station and DGPS measurements (this work, 2014–2016)
2	Manual estimation and photographs
3	Geodetic surveys (1989) ¹ and manual estimation
4	Geodetic surveys (1989) ¹ and manual estimation
5	Hand-tuning and photographs

¹ [Wagner, 1996; Lüthi, 2000; Lüthi and Funk, 2000]

5.1.4 Bedrock topography and glacier thickness

Table 5.2 summarizes data sets and methods used to derive the bedrock DEM for each glacier sector. Similar as for the surface topography (see section 5.1.3), for locations with insufficient data coverage the bedrock DEM is manually adjusted, in view to reproduce measured surface velocities and snow accumulation rates as good as possible. This approach partly follows the method used in Gilbert et al. [2014a], where bedrock adjustments were performed based on the measured surface accumulation. The influence of the bedrock topography of the ice cliff and Grenzgletscher boundary areas on the flow behaviour of the north-exposed flank of CG is included in the error estimation of the calculated ice-core source points and chronologies (main goals of this work, see sections 7.5 and 7.6).

Glacier bed data in the area surrounding the ice-core drill sites are cubically interpolated from different GPR profiles recorded in 2000 [Eisen et al., 2003], 2008 and 2010 [Konrad, 2011; Bohleber, 2011; Konrad et al., 2013]. The GPR profiles link the drill sites KCC, KCI, KCS, CC and KCH. As an example, Figure 5.3 shows the radargram of the GPR profile between the KCI and KCS sites [Konrad et al., 2013]. In the lower part of the image the GPR reflection representing the ice-bedrock transition is clearly visible.

In the work of Konrad et al. [2013], the uncertainty of the ice thicknesses was estimated to be at least 16% in areas with strongly inclined bedrock. In addition the authors pointed out, that GPR measurements typically tend to underestimate the ice thickness. In accordance to the uncertainty of the GPR measurements mentioned above, GPR profiles predict a glacier thickness of ~ 63 m at the KCC drilling position, while the

Table 5.2: Summary of data sources used to estimate the bedrock DEM for the glacier sectors defined in section 5.1.1 (see also Figure 5.1). For “manual estimation” see text.

Sector	Bedrock DEM based on:
1	GPR (2000, 2008 and 2010) ¹ and manual estimation at KCC site
2	Manual estimation
3	GPR (1989, 1990, 1996) ² and manual estimation
4	GPR (1989, 1990, 1996) ² and manual estimation
5	Manual estimation

¹ [Eisen et al., 2003; Konrad, 2011; Bohleber, 2011; Konrad et al., 2013]

² [Wagner, 1996; Lüthi, 2000; Lüthi and Funk, 2000]

length of the extracted KCC core is ~ 72 m [Bohleber et al., 2017]. In order to make the glacier geometry consistent with the KCC core length, a depression is manually included around the KCC drilling position. The GPR-derived glacier thickness measured at the other drill sites (KCI, KCH, CC and KCS) is in accordance with the lengths of the extracted cores and no further adjustments are required.

Bedrock elevations in the vicinity of the ice cliff are manually estimated as outlined above. In this area, information about the glacier bed are difficult to gather using GPR, since bedrock reflections are hard to distinguish from reflections due to the vertical ice-air interface at the ice cliff [Bohleber, 2011]. The bedrock DEM of the northern side of the saddle is based on the measured topography used in Wagner [1996], Lüthi

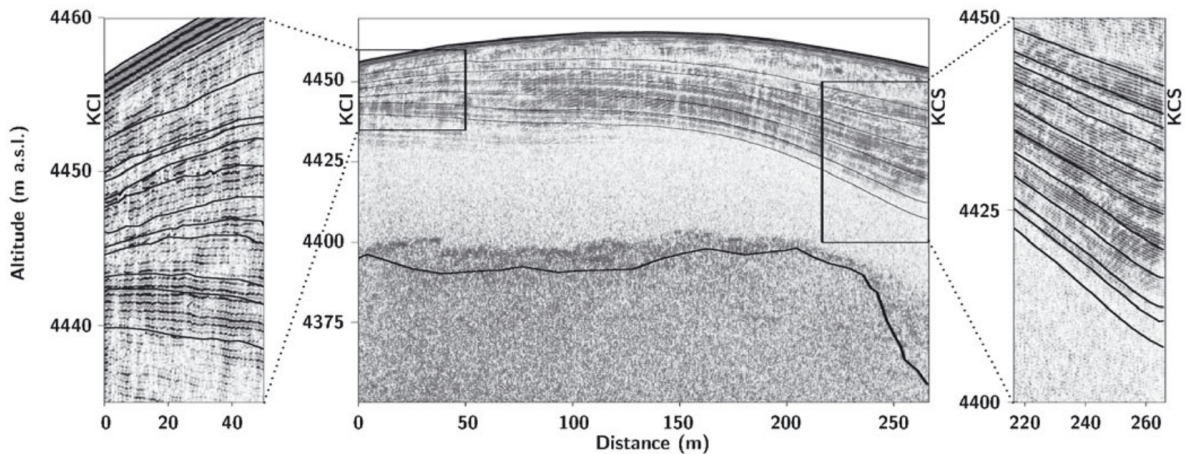


Figure 5.3: Radargram of the GPR profile between the KCI and KCS drill sites. The black lines indicate isochronous reflection horizons in the firn column of the glacier. No isochrones are visible in the ice column of the glacier (light grey color in the GPR profile), but the reflection of the bedrock (lower dark grey zone) is clearly visible (the black line represents the utilized bedrock surface). Figure taken from Konrad et al. [2013].

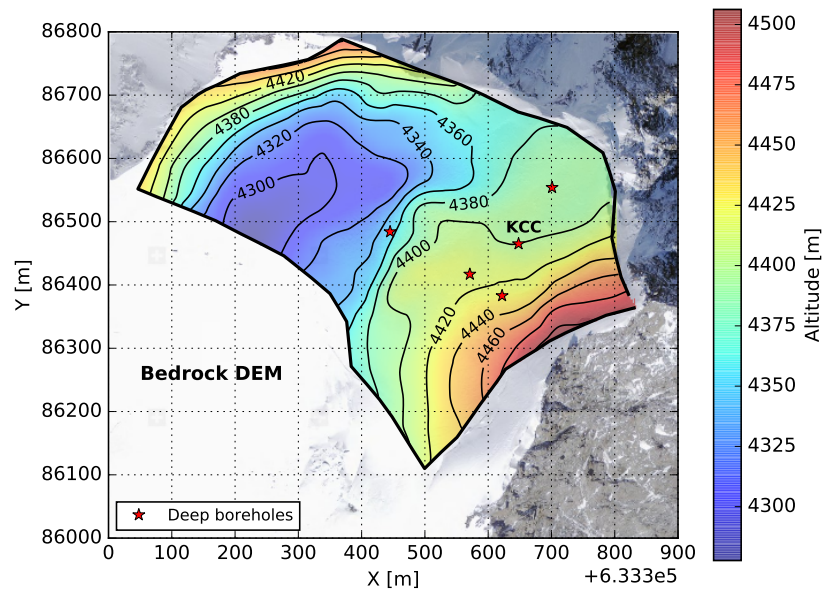


Figure 5.4: Bedrock DEM used as input in the numerical model. The topography of the area surrounding the ice-core drilling sites is based on GPR profiles recorded in the period 2008–2010 [Konrad, 2011; Bohleber, 2011; Konrad et al., 2013], with addition of one profile measured in 2000 [Eisen et al., 2003].

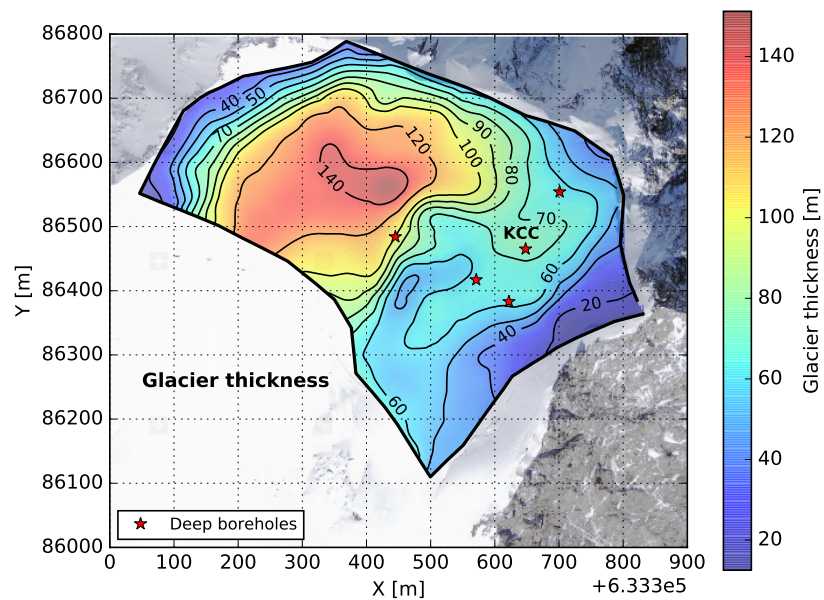


Figure 5.5: Map of glacier thickness at CG derived as difference of the surface DEM and the bedrock DEM used as model input. The slightly enhanced ice thickness in the vicinity of the KCC drilling site is manually inserted in order to make the glacier geometry consistent with the KCC core length.

[2000] and Lüthi and Funk [2000], but adapted (if needed) close to the sector boundaries. The bedrock DEM of the southernmost glacier sector is manually estimated. Figure 5.4 illustrates the topography of the glacier bed used as model input in this work. The glacier thickness map shown in Figure 5.5 is obtained subtracting the bedrock DEM of Figure 5.4 from the surface DEM of Figure 5.2 (note the enhanced glacier thickness nearby the KCC drill site in Figure 5.5).

5.2 Mechanical boundary conditions

5.2.1 Lateral boundaries

The border of the modeling area is divided into four sections. The most relevant properties of the boundaries, and the way these properties are taken into account in the model, are presented in this section:

- The **southern boundary** follows roughly the bergschrund below Signalkuppe. The bergschrund is periodically open, sometimes however not visible due to snow coverage. Figure 5.6, left, shows a picture of the open bergschrund in 2003 [IUP glaciology group database]. A close inspection of the bergschrund was performed in September 1999. The opening was of order 1 m and reached at the descent point a depth of about 18 m down to bedrock [Keck, 2001]. Due to very slow flow velocities and small ice thickness above the bergschrund, the stress on this boundary is negligible. Therefore, in this study the bergschrund boundary is treated as stress-free.
- The **western boundary** corresponds to the outflow towards Grenzletscher. A



Figure 5.6: Left: open bergschrund below Signalkuppe in 2003 [IUP glaciology group database]. Right: sudden increase in bedrock slope on the western boundary of CG producing the aperture of crevasses; the bergschrund below Zumsteinspitze, which was open in 2016 (photo: Helene Hoffmann, modified).

rapid increase in the bedrock slope is responsible for the aperture of big crevasses (Figure 5.6, right panel). The normal stress σ_n on this boundary is parametrized as suggested in Lüthi [2000] and Lüthi and Funk [2000]. Moving downwards from the surface, the boundary is kept stress-free as far as the crevasse is open, whereas below the closure point the normal stress increases linearly:

$$\sigma_n(d) = \begin{cases} 0 & , d < d_c \\ \kappa(d - d_c) & , d \geq d_c \end{cases} \quad (5.1)$$

with d the depth coordinate, d_c the crevasse depth and κ the vertical stress gradient. In this work the crevasse depth is set to $d_c=30$ m, and, following the work of Lüthi [2000] and Lüthi and Funk [2000], the vertical stress gradient is set to $\kappa=10^4$ Pa m⁻¹. The crevasse is assumed to extend along the boundary between the y -coordinates 86270 m and 86500 m. The remaining boundary segment south of the crevasse is treated as stress-free, due to the presence of an almost vertical wall, creating a small ice fall just a few meters downstream.

- The **northern boundary** is located on the slope below Zumsteinspitze. The presence of a bergschrund (see Figure 5.6, right) leads to setting a stress-free northern boundary. However, the influence of this boundary on the flow behaviour in the central part of the glacier is negligible.
- The ice cliff defines the **eastern boundary** of the study area and is treated as stress-free. Bedrock and surface altitudes at this boundary govern the outgoing mass flux through the cliff and therefore influence strongly the flow pattern of the glacier. The estimation of bedrock and surface topography close to the ice cliff is discussed in more detail in section 5.1.3 and 5.1.4. Stretching forces in the vicinity of the ice cliff are so strong, that crevasses can open, as documented in Bohleber [2011]. These kind of features are however not taken into account in this study.

5.2.2 Basal conditions

Although englacial temperatures measured at CG show evidence of warming since 1991 [Hoelzle et al., 2011], englacial temperatures close to bedrock, ranging still between -12°C and -13°C [Hoelzle et al., 2011], are far below the pressure melting point. Therefore the glacier is assumed to be frozen to bedrock, i.e. ice-flow velocities at bedrock are set to zero.

5.3 Thermodynamic boundary conditions

Main goal of the thermodynamic calculations is to provide a reliable temperature field of CG, which is required to calculate a reliable velocity field (see dependence of the creep parameter A and of the fluidity parameter B in section 3.5.1 and 3.5.3). In this context, thermodynamic boundary conditions are adjusted in view of reproducing

measured englacial temperatures. This concerns in particular spin-up surface temperatures $T_s(x, y)$ (sections 5.3.1), and basal heat flux (section 5.3.4). In this work, the thermodynamic boundary condition at the surface is defined as follows:

- For the model spin-up (see coupling diagram in Figure 5.13 in section 5.4), steady (constant over time) surface temperatures $T_s(x, y)$ are used as boundary condition.
- For the fully coupled transient simulations (see coupling diagram in Figure 5.14 in section 5.4) atmospheric temperature anomalies $T_{dev}(t)$ since 1901 are taken into account (see section 5.3.2), together with additional energy source terms $\tilde{Q}_{lat}(t)$ due to surface meltwater refreezing (see section 5.3.3, work of J. Lier [pers. comm., 2017. Master Thesis in preparation]). Using the enthalpy formulation presented in section 3.4.2, for the fully coupled transient simulations the thermal boundary condition at the surface is:

$$H_{surf}(t, x, y) = H(T_s(x, y) + T_{dev}(t)) + \tilde{Q}_{lat}(t) \quad (5.2)$$

where the relation between temperature and enthalpy is given in equation (3.38) (section 3.6). The calculated transient temperature field using $H_{surf}(t, x, y)$ as surface boundary condition is validated by comparison with measured englacial temperatures (see section 7.4). However, it is not possible to validate the relative contribution of T_s , T_{dev} and \tilde{Q}_{lat} to the surface enthalpy H_{surf} (the three terms may compensate each other). Therefore T_s , T_{dev} and \tilde{Q}_{lat} can be in reality different from the values assumed in this work.

5.3.1 Spin-up surface temperatures

Before running a transient simulation taking into account atmospheric temperature variations, the full Stokes model is run to equilibrium imposing constant boundary conditions (spin-up). The constant surface temperatures $T_s(x, y)$ used for the spin-up are shown in Figure 5.7 (see later in this section how this map is estimated). Spatial variations of surface temperatures are related to the topography of the glacier, as well as to differences in surface altitude, slope, aspect and wind exposure.

In the central part of the glacier, from where borehole temperature measurements are available (red stars in Figure 5.7), surface temperatures are adjusted in view of minimizing the discrepancy between measured¹ and modeled temperature profiles (see validation of the modeled temperature field in section 7.4). On the other hand, surface temperatures of the northern half of the glacier are not constrained by measurements. For the sake of simplicity, aiming to avoid complex surface energy balance models, surface temperatures of this area are set as best guess, taking into account altitude and aspect of the domain (south-facing). Note that high uncertainty in the bedrock topography exists for this area (see section 5.1.4), rendering this simplification not the limiting factor

¹The temperature profiles used as reference for the adjustments are plotted in comparison with the model results in Figure 7.15 of section 7.4. Main characteristics of the profiles can be found in Table 7.2 of section 7.4

of the accuracy of the model results. Following the same scheme, surface temperatures nearby the bergschrund are set slightly lower than in the saddle area, since this region is north-exposed and higher in altitude.

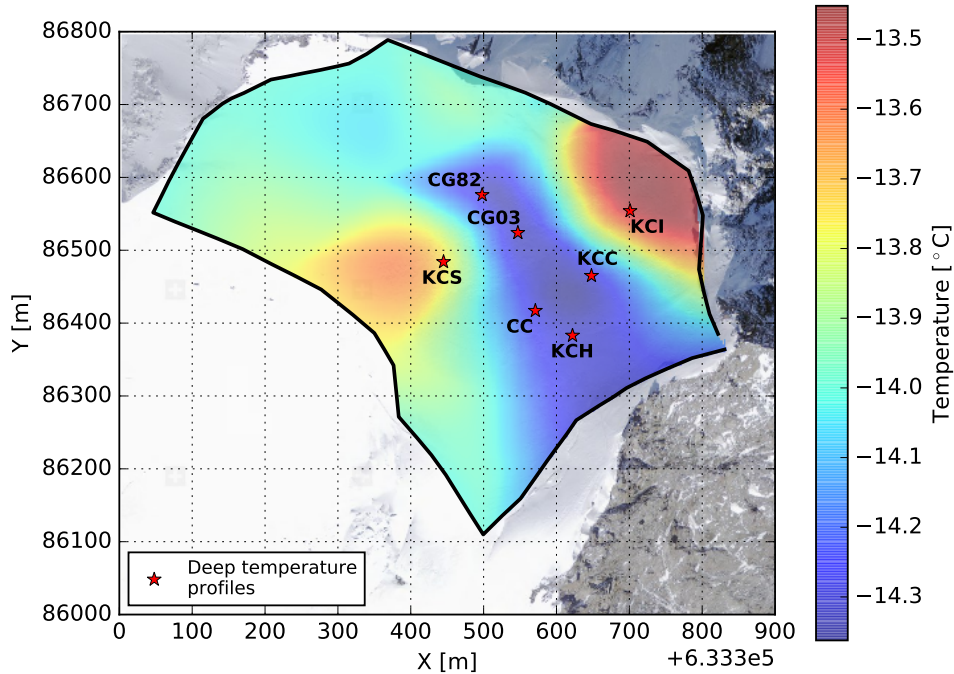


Figure 5.7: Surface temperatures $T_s(x, y)$ used for the model spin-up. Red stars indicate the position of the measured borehole temperature profiles used to adjust surface temperatures in the central part of the glacier.

5.3.2 Atmospheric forcing

In contrast to the assumptions made in support for the spin-up of the model, the temperature boundary condition at the glacier surface is time dependent, since it is influenced by changes in atmospheric air temperatures. The temperature boundary condition at the glacier surface is therefore forced and estimated according to variations of the air temperatures. In this work, atmospheric temperature anomalies $T_{dev}(t)$ are considered starting from the year 1901, with a resolution of one year, and are added to the spin-up temperatures $T_s(x, y)$ shown in Figure 5.7 (see also equation (5.2)).

Air temperature anomalies used to force the surface boundary condition are based on instrumental data and are presented in Figure 5.8 (yearly averaged data). They show a clear increasing (non-steady) trend. The anomalies are calculated with respect to the mean temperatures after 1982 (according to the data coverage). The black line represents the time series used in the model, which is built on four time series. Meteorological data from a weather station installed at the Margherita Hut² (4560 m a. s. l.) (data available since September 2002) are integrated with data from weather

²Weather station operated by Arpa Piemonte <http://www.arpa.piemonte.gov.it>

stations installed at Gornergrat³ (3129 m a. s. l.) and Zermatt³ (1638 m a. s. l.). Those weather stations offer data coverage back to the early 1980s (and in the 1960s for the Zermatt station). Instrumental temperature data back in time until the year 1901 are taken from the HISTALP⁴ database (Monte Rosa grid cell) [Auer et al., 2007]. As apparent in Figure 5.8, the correlation between the four anomaly time series is high.

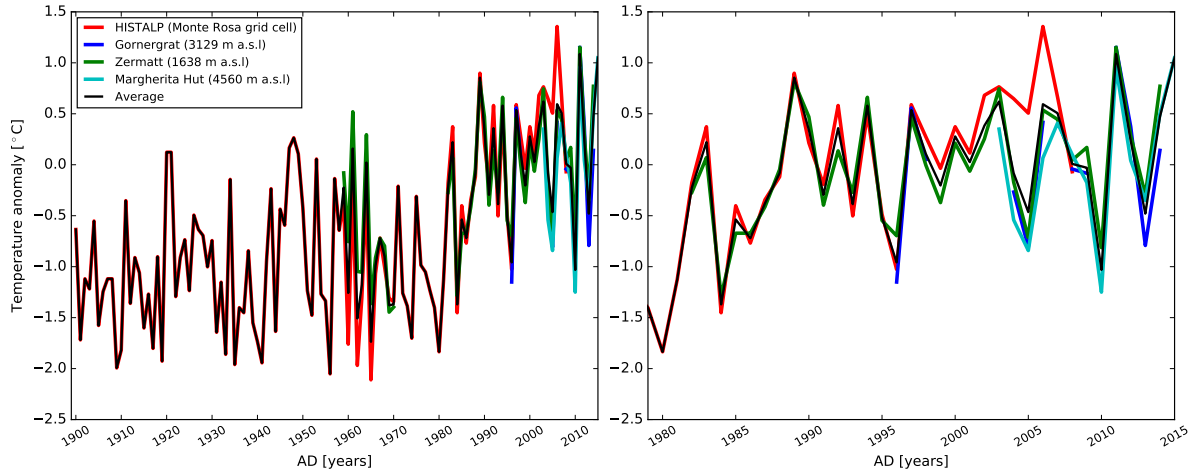


Figure 5.8: Air temperature anomalies $T_{dev}(t)$ for CG based on instrumental data in the period 1900–2008 (HISTALP, Monte Rosa grid cell) and direct measurements after 1982 (yearly average data). The anomalies are calculated with respect to the mean temperature after 1982. Left: whole time series. Right: zoom for 1980 until 2015. The black line represents the average over all four data sources. Although the weather stations are situated at different locations and altitudes, the correlation between the (measured) temperature anomalies is very strong.

5.3.3 Surface meltwater refreezing

Heat sources at the glacier surface⁵ due to refreezing of meltwater are taken into account in the full Stokes model by applying a variation of the degree-day model introduced by Hock [1999]. The degree-day model assumes a linear correlation between positive daily maximum air temperatures and the amount of produced meltwater. This model was already used in Gilbert et al. [2014b] to model near-surface temperatures of the high Alpine glacier site Col du Dôme (Mont Blanc massif). In the present thesis the effect of atmospheric warming on the glacier temperature field is reproduced by using a transient simulation with a time step of one year. Therefore, the degree-day model is reduced to a degree-year model:

$$\tilde{Q}_{lat}(x, y) = \tilde{T}^+ a(x, y) \quad (5.3)$$

³Weather station operated by MeteoSchweiz <http://www.meteoschweiz.ch>

⁴<http://www.zamg.ac.at/histalp>

⁵In this work it is assumed that all the latent heat due to meltwater refreezing is released at the glacier surface, neglecting any form of meltwater percolation

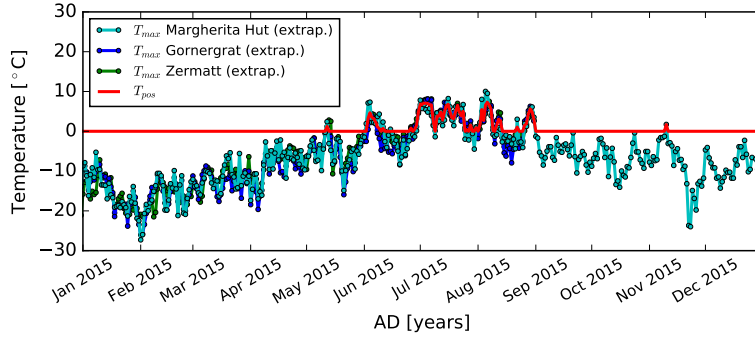


Figure 5.9: Daily maximum air temperatures at CG for 2015, extrapolated to the altitude of CG from data registered at the Margherita Hut, Gornergrat and Zermatt. The parameter T^+ defined in equation (5.4) is represented by the red line. Results provided by J. Lier [pers. comm., 2017].

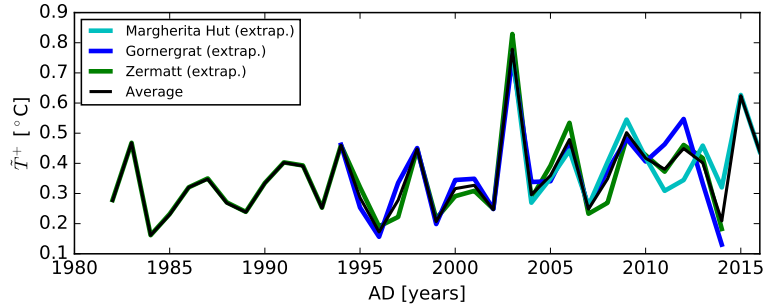


Figure 5.10: The parameter \tilde{T}^+ at CG estimated for the years 1982–2016 based on meteorological data registered at the Margherita Hut, Gornergrat and Zermatt. The data used for the simulations are the average of the three datasets (black line). Results provided by J. Lier [pers. comm., 2017].

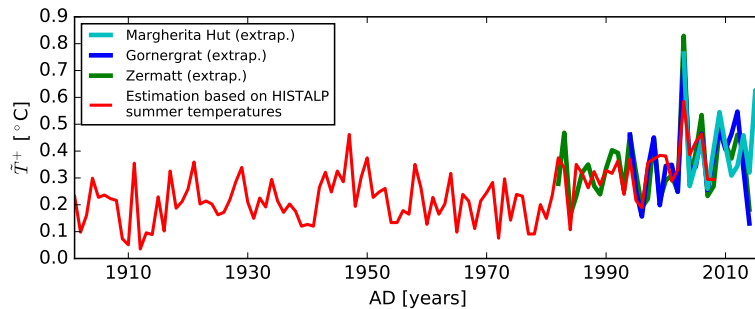


Figure 5.11: The parameter \tilde{T}^+ at CG estimated for the years 1901–2016. The red line describes the estimation of \tilde{T}^+ based on the correlation between \tilde{T}^+ and the summer temperatures taken from the HISTALP database (Monte Rosa grid cell) [Auer et al., 2007] in the period 1982–2008.

In our formulation (equation (5.2)) the quantity \tilde{Q}_{lat} is expressed in J kg^{-1} and represents the yearly averaged amount of heat released at the glacier surface due to refreezing of meltwater. The parameter $a(x, y)$ in $\text{J kg}^{-1} \text{K}^{-1}$ is the space dependent melt factor and \tilde{T}^+ is the yearly mean of the quantity T^+ , defined as:

$$T^+ = \begin{cases} T_{max} & , \text{ if } T_{max} \geq 0 \\ 0 & , \text{ if } T_{max} < 0 \end{cases} \quad (5.4)$$

with T_{max} the daily maximum air temperatures at the glacier surface expressed in $^{\circ}\text{C}$. To illustrate the meaning, in Figure 5.9 the parameter T^+ is plotted in red in daily resolution for the year 2015. The temperatures T_{max} used to calculate T^+ (extrapolated to the CG altitude from weather station data, see later in this section) are represented in cyan, blue and green.

The parameter \tilde{T}^+ is calculated for the years 1982 to 2016 (see Figure 5.10) based on daily air temperatures registered at the Margherita Hut, Gornergrat and Zermatt⁶, and extrapolated to the CG site using altitude temperature gradients [pers. comm. J. Lier, 2017]. For the period before 1982 no continuous daily meteorological data are available from the weather stations mentioned above. Before 1982 the parameter \tilde{T}^+ is therefore determined in an alternative way, namely via the correlation found between the parameter \tilde{T}^+ and the average temperatures of the summer months (May to September) available from the HISTALP database (for the grid point containing the Monte Rosa area) in the period 1982–2008. Results of this estimation are presented in Figure 5.11 in red.

In our formulation (equation (5.3)), the melt factor $a(x, y)$ indicates how much energy per unit of (firn/ice) mass and per degree Celsius is released in the glacier after refreezing of the produced meltwater. The melt factor is site-dependent and therefore different for each glacier, since it is dependent on local characteristics such as Potential Solar Radiation⁷ (PSR), mean albedo, wind speed, humidity and surface roughness [Gilbert et al., 2014b]. The estimation of the melt factor a for CG was performed by J. Lier [pers. comm., 2017]. The melt factor is determined by analyzing density anomalies of deep and shallow ice cores recovered at CG from 1991 to 2016, aiming to quantify past melt events, as done by Gilbert et al. [2014b] for the Col du Dôme glacier. As expected, it results that the firn zone of ice cores located in areas with higher PSR contains a higher ice contribution compared to cores from areas with lower PSR. This is a sign of more frequent melt events. Nevertheless, no clear correlation is found between the estimated melt factors (relative contribution of ice in firn) and local PSR, since at CG areas with enhanced insolation correspond to areas with enhanced snow accumulation (less efficient wind erosion, see section 2.1). The estimated melt factor ranges between 100 and 500 $\text{J kg}^{-1} \text{K}^{-1}$ [pers. comm. J. Lier, 2017]. However, the true value is likely even higher since the applied method neglects multiple thawing and refreezing of the same melt

⁶The weather stations are referenced in section 5.3.2

⁷Factors influencing PSR are: surface slope, aspect, altitude, latitude and relief shading. A method to calculate clear sky shortwave solar radiation is presented in Kumar et al. [1997]

layer at weather conditions with several consecutive hot days, as often encountered in summer. Therefore, a melt factor of $1500 \text{ J kg}^{-1} \text{ K}^{-1}$ constant in space and time is used, for which model results produce a better agreement with the measured temperature profiles. Note that the melt factor a required in the model to reproduce the measured temperature profiles may be biased by imprecise knowledge of T_s and T_{dev} (see comments on equation (5.2)). Therefore, the melt factor used can be in disagreement with the empirical estimation.

5.3.4 Basal heat flux

Basal heat fluxes at high altitude glaciers are governed by the thermal conductivity of the rocks from the mountain below, as well as by the presence of partly thawing and refreezing permafrost inside the mountain [Lüthi, 2000; Lüthi and Funk, 2001]. Further, basal fluxes are influenced by the shape of the mountains, in particular by the presence of exposed slopes and their snow cover. In Switzerland the estimated geothermal heat flux at sea level amounts to 70 mW/m^2 [Medici and Rybach, 1995], decreasing to fluxes between 20 and 40 mW/m^2 [Haeberli and Funk, 1991; Lüthi, 2000; Lüthi and Funk, 2001; Suter, 2002] at altitudes of cold glaciers. These fluxes are close to the 15 mW/m^2 used in Gilbert et al. [2014a] to model the thermal regime of the Col du Dôme glacier. Basal heat fluxes used in this work as boundary condition are displayed in Figure 5.12 (see later in this section how this map is estimated). The fluxes range between 30 and

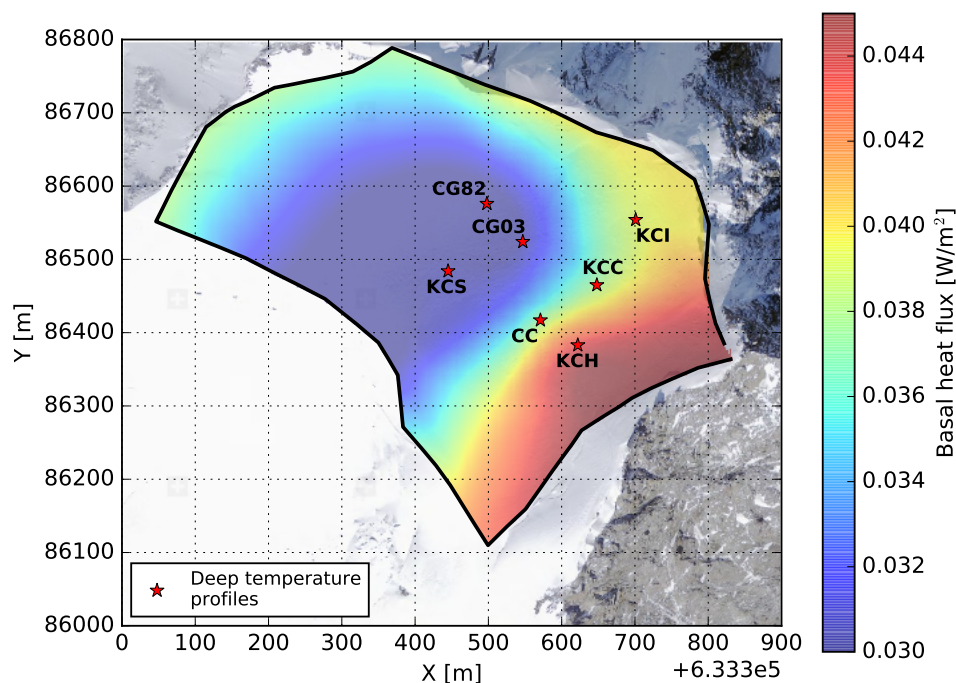


Figure 5.12: Basal heat flux map used within this work as boundary condition in the full Stokes model. Basal heat fluxes are strongly influenced by lateral fluxes due to exposed slopes.

45 mW/m² and are therefore consistent with the literature values mentioned above. Aiming to avoid complex heat flow modeling of the whole Monte Rosa massif down to sea level [Lüthi, 2000; Lüthi and Funk, 2001], basal heat fluxes are adjusted in order to match vertical temperature gradients of measured deep temperature profiles⁸. Results of the estimation at the available borehole sites are summarized in Table 5.3. Due to additional lateral heat fluxes coming from the south face of Monte Rosa, the estimated basal heat flux at the KCH drilling site is much higher than basal fluxes in the central saddle region. In a similar way, the basal flux estimated at the KCI drilling site is higher than in the central saddle region due to the influence of the east face of Monte Rosa. For glacier areas not covered by direct measurements, basal fluxes are estimated as best guess, based on the presence or absence of exposed slopes nearby.

Table 5.3: Basal heat fluxes estimated at the deep drill sites. Core lengths after Gabrieli et al. [2011], Wagenbach et al. [2012], Bohleber et al. [2013] and Bohleber et al. [2017].

Borehole	Basal heat flux (estimated) [mW/m ²]	Max. depth of temperature profile [m]	Ice-core length [m]
KCC	38	73	72
KCI	39	62	62
KCH	44	61	60
CC	38	35	64
KCS	30	101	100
CG03	30	80	81
CG82	30	120	120

5.4 Operating the model

This section is focusing on how the field equations governing the glacier flow (see chapter 3 for more details) are combined in order to get a steady state fully thermo-mechanically coupled solution (spin-up). The steady state solution is used afterwards as initial condition to calculate a transient fully coupled solution, taking into account surface temperature changes. The procedures are illustrated schematically in Figure 5.13 and 5.14, partly following the procedure presented in Gilbert et al. [2014a].

Steady state solution (spin-up)

In the first phase of the spin-up, the Stokes equation (momentum conservation and constitutive equation) and the continuity equation are coupled running a transient simulation (Figure 5.13, left). In a first step, the velocity and pressure field are calculated

⁸The temperature profiles used as reference for the adjustments are plotted in comparison with the model results in Figure 7.15 of section 7.4. Main characteristics of the profiles can be found in Table 7.2 of section 7.4

inserting a prescribed initial density and temperature field in the Stokes equation. For a fast convergence to a steady solution, the initial density and temperature field need to be chosen as realistic as possible. The resulting velocity field is inserted in the continuity equation, producing a new density field, which is then used again to obtain a new velocity field. This procedure is iteratively repeated until velocity and density field are stable. At this point, a diagnostic simulation starts (Figure 5.13, right). The solution of the Stokes equation is used to calculate the strain heating. A new temperature field is computed, inserting the calculated velocity and density field, together with the strain heating, in the enthalpy equation. The resulting temperature field is then used to restart a new transient run. Transient and diagnostic runs are iteratively repeated until all variables reach equilibrium. At this point the spin-up is finished and a fully thermo-mechanically coupled steady solution is achieved. The evolution of the norm of the velocity and density solution during the model spin-up (spin-up used to produce the results presented in chapter 7) is shown in Figure A.3 and A.4 in appendix A.4. During the spin-up all boundary conditions like surface elevation and temperature are kept constant over time.

Transient solution

The fully coupled steady state solution serves as initial condition for the subsequent transient simulation. Aim of the transient simulation is to account for observed varia-

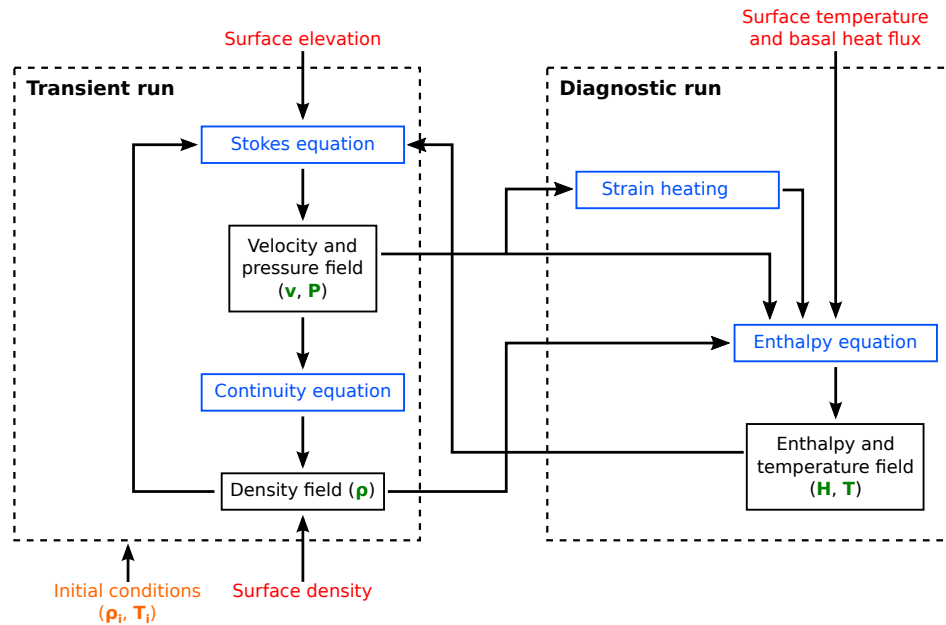


Figure 5.13: Execution of the spin-up of the full Stokes model including the equations to be solved (blue), the calculated variables (green), the boundary conditions (red) and the initial conditions (orange). Procedure partly following Gilbert et al. [2014a].

tions in the atmospheric air temperature, and consequently in the temperature boundary condition at the surface. In this work, atmospheric forcing is considered starting from the year 1901 onwards at annual resolution (see section 5.3.2). Figure 5.14 illustrates the procedure to calculate the fully coupled transient solution. First, according to the current year, the thermodynamic boundary condition at the glacier surface is prescribed. This concerns the yearly averaged surface temperature and the amount of refreezing meltwater (see section 5.3.3). Afterwards a new temperature field is calculated and used to recalculate velocity and density. The procedure is repeated for each of the simulated years.

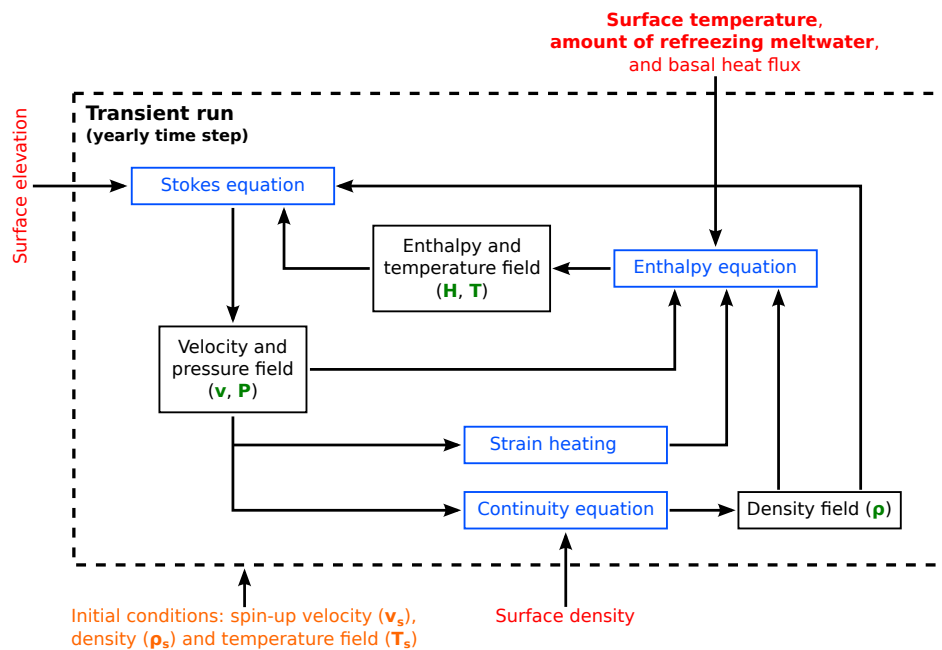


Figure 5.14: Procedure to calculate the fully coupled transient solution of the full Stokes model, taking into account atmospheric air temperature changes, including the equations to be solved (blue), the calculated variables (green), the boundary conditions (red and in bold if time-dependent) and the initial conditions (orange). Procedure partly following Gilbert et al. [2014a].

6 Numerical implementation

The Finite Element software Elmer/ice used in this work for the numerical implementation of the flow model is introduced in the first part of this chapter (section 6.1). Note that the goal of the section is not to give an introduction into the Finite Element method (basic knowledge is assumed here). The mesh used to approximate the glacier geometry and the solvers deployed to solve the equations are presented in section 6.2 and 6.3. Tests performed to implement bubble close-off in the Elmer/Ice Porous-Solver, the solver dedicated to the solution of the Stokes equations using the firn flow law, are presented in section 6.4. An attempt to combine firn and anisotropic law is presented in section 6.5.

6.1 The Finite Element software Elmer/Ice

The equations required to execute the full Stokes model (see section 5.4) are numerically solved using the state-of-the-art Finite Element software Elmer/Ice¹ [Gagliardini et al., 2013]. The Elmer/Ice code is based on the multi-physics open-source simulation software Elmer, mainly developed by CSC². With respect to Elmer, Elmer/Ice incorporates modules dedicated to solve specific glaciological problems, like e.g. firn rheology [Zwinger et al., 2007], anisotropic ice rheology [Gillet-Chaulet et al., 2005; Ma et al., 2010; Zwinger et al., 2014], fabric evolution [Gillet-Chaulet et al., 2006], enthalpy transport [Gilbert et al., 2014a], hydrology [De Fleurian et al., 2014; Werder et al., 2013], grounding line dynamics [Favier et al., 2012, 2014], calving dynamics [Todd and Christoffersen, 2014] and damage mechanics [Krug et al., 2014]. Besides full Stokes applications, Elmer/Ice can solve Shallow Ice Approximation (SIA) and Shallow Stream/Shelf Approximation (SSA) as well. The broad range of applications of Elmer/Ice includes small-scale problems with complex geometry and boundary conditions [Gagliardini et al., 2011; Gilbert et al., 2015], as well as simulations on the ice-sheet scale [Gillet-Chaulet et al., 2012; Seddik et al., 2012].

Basic concepts and usage guidelines of Elmer can be found in the ElmerSolver Manual³ [Ruokolainen et al., 2017], whereas a description of the implemented physical models (the solvers) is given in the Elmer Models Manual⁴ [Råback et al., 2017]. The documentation of the Elmer/Ice specific modules can be found on the Elmer/Ice-Wiki⁵ [Elmer/Ice-Wiki, 2017].

¹<http://elmerice.elmerfem.org>

²<https://www.csc.fi/web/elmer>

³<http://www.nic.funet.fi/pub/sci/physics/elmer/doc/ElmerSolverManual.pdf>

⁴<http://www.nic.funet.fi/pub/sci/physics/elmer/doc/ElmerModelsManual.pdf>

⁵<http://elmerice.elmerfem.org/wiki/doku.php?id=start>

6.2 The mesh

The three-dimensional mesh used to approximate the CG glacier geometry is presented in Figure 6.1. The mesh consists of 3088 nodes and 2505 trilinear hexahedrons (Elmer element type code 808 [Ruokolainen et al., 2017]). Hexahedrons are used, since they are compatible with the available implementation of the AIFlow-Solver and with the *bubbles* stabilization method in the AdvectionReaction-Solver (see section 6.3).

The mesh is generated starting from a two-dimensional mesh of the footprint of the glacier, created using the Gmsh⁶ mesh generator (see Figure 6.2). The two-dimensional mesh has a mesh size of 50 m and consists of 193 nodes and 167 quadrilateral elements (Elmer element type code 404 [Ruokolainen et al., 2017]). The three-dimensional mesh is extruded from the two-dimensional footprint, based on the surface and bedrock DEM given as input. As a consequence of the extrusion, nodes of different layers are aligned in the vertical direction. There are 16 extrusion layers. As visible from Figure 6.1, the extrusion layers are not equally distributed in the vertical direction, but are more frequent coming closer to the surface. The motivation of such a distribution is to better describe the near-surface changes of density and temperature.

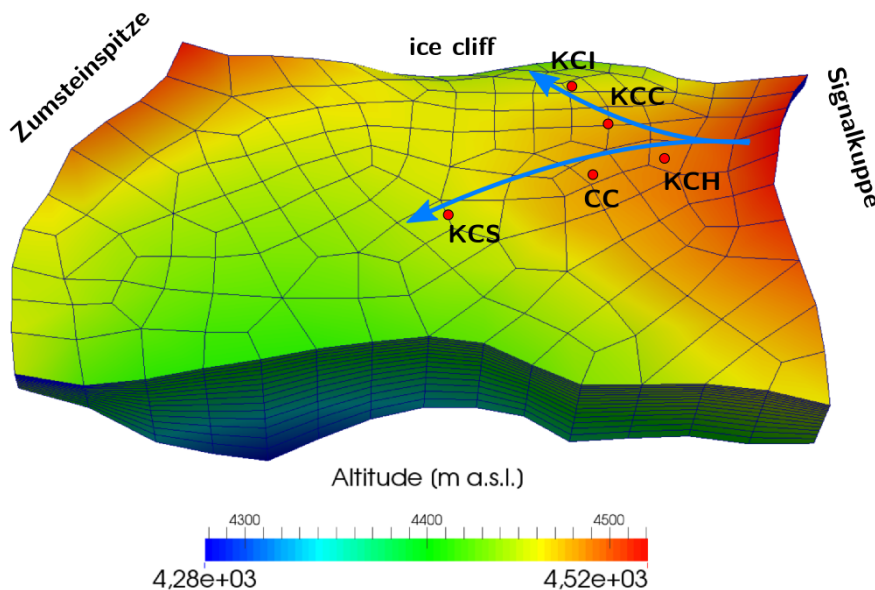


Figure 6.1: Three-dimensional mesh used to approximate the geometry of CG (visualization using ParaView). The mesh consist of 3088 nodes and 2505 trilinear hexahedrons, with 16 extrusion layers. The blue lines indicate roughly the flowlines of the north-facing flank.

⁶<http://gmsh.info/>

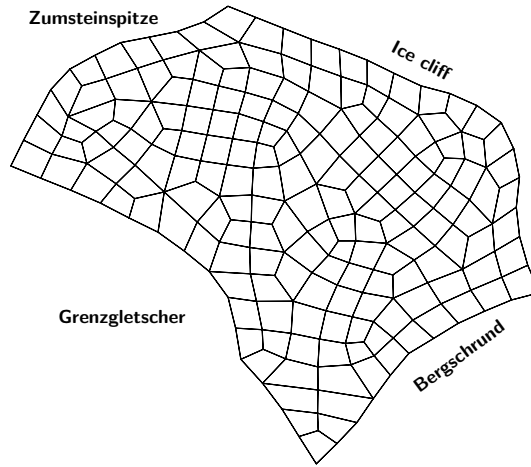


Figure 6.2: Two-dimensional mesh of the glacier footprint calculated using the Gmsh mesh generator. The mesh consist of 193 nodes and 167 quadrilateral elements, and has a mesh size of 50 m.

6.3 Deployed Solvers and User Functions

The most important Elmer and Elmer/ice solvers used in this work are listed in Table 6.1. Solvers required for standard operations, like data interpolation, mesh extrusion or export of data, are not included in the list. If not specified, the deployed solvers are part of the Elmer version 8.2 (Rev: a5adc1d) and are documented in the Elmer Models Manual [Råback et al., 2017] or in the Elmer/Ice-Wiki [Elmer/Ice-Wiki, 2017].

The version of the used AdvectionReaction-Solver is not part of the Elmer distribution. In the early stages of this work, the AdvectionReaction-Solver was run using the Discon-

Table 6.1: List of the most relevant Elmer and Elmer/Ice solvers deployed in this work, with the corresponding equation (see chapter 3) or physical problem to solve, and the deployed linear system solvers.

Solver name	Equation / physical problem	Linear system solver ¹
Porous	Stokes + firn flow law	Direct, Mumps
AIFlow	Stokes + anisotropic law (GOLF)	n.a.
AdvectionReaction ²	continuity eq. / dating eq.	Direct, Mumps
Enthalpy	enthalpy eq.	Direct, Mumps
FreeSurface	free-surface eq.	Iterative, BiCGStab, ILU0
ParticleDynamics	particle tracking	n.a.
StrainHeating ³	$tr(\boldsymbol{\sigma}\dot{\boldsymbol{\epsilon}})$	Direct, Umfpack

¹ Details in Ruokolainen et al. [2017]

² Using the stabilization method *bubbles* for the continuity equation and *stabilized* for the dating equation (not part of the Elmer distribution)

³ Self-implemented (not part of the Elmer distribution)

tinuous Galerkin (DG) method [Brezzi et al., 2004; Kuzmin, 2010]. However, the calculated density field showed irregularities and oscillations, especially close to the model boundaries. A more reliable density solution is achieved using the AdvectionReaction-Solver together with the *bubbles* stabilization method [Arnold et al., 1984; Baiocchi et al., 1993; Brezzi et al., 1992]. The implementation of the *bubbles* stabilization method for the AdvectionReaction-Solver was made by the Elmer developers, but it has been not available in the Elmer distribution when the calculations were performed. For the calculation of the age field deploying the dating equation (see section 3.4.4), the AdvectionReaction-Solver is used together with the Streamline Upwind Petrov-Galerkin (SUPG) stabilization method [Donea, 1984; Hughes, 1987] (Elmer keyword: *stabilized*). Systematic comparisons between different stabilization methods for transport equations using Elmer/Ice can be found in Brondex [2017] (in press).

The StrainHeating-Solver is self-implemented and is not part of the Elmer distribution. The solver calculates the heat source term in the Enthalpy equation due to ice deformation (see section 3.4.2) and is a modification of the DeformationalHeat-Solver available in Elmer/Ice. Other than the DeformationalHeat-Solver, the StrainHeating-Solver calculates the strain heating directly from the calculated strain and stresses, with no need to define a viscosity parameter, therefore it can be used for any flow law.

User Functions (USF)

In Elmer, USFs are widely used to define boundary conditions, initial conditions and variable parameters. In this work, USFs are used to define:

- the mechanical boundary condition of the western glacier boundary, characterized by the presence of a big crevasse as described in equation (5.1) of section 5.2.1;
- the surface thermal boundary condition, i.e. the surface enthalpy $H_{surf}(t, x, y)$, evaluated taking into account the local spin-up temperatures $T_s(x, y)$, the time dependent atmospheric forcing $T_{dev}(t)$ and the time dependent amount of heat due to refreezing meltwater $\dot{Q}_{lat}(t)$ as described in equation (5.2) of section 5.3;
- the fluidity parameter B in the firn flow law (see section 3.5.3 and Figure 3.4 in section 3.5.1) and the enthalpy diffusivity κ (see equation (3.42));
- the initial density field ρ_i (see Figure 5.13 section 5.4) and the prescribed fabric distribution (see Figure 7.6 in section 7.1.3).

6.4 Implementation of bubble close-off

Bubble close-off influences the flow dynamics of glaciers. Section 3.5.4 describes how the firn flow law changes, if bubble close-off is taken into account. Here we present how the Porous-Solver, the Elmer/Ice solver dedicated to compute velocity and pressure using the firn flow law, is modified in order to implement bubble close-off. A general description of the Porous-Solver and of the modifications is given in section 6.4.1. The modifications are tested on a simple test case (see section 6.4.2). Test applications of the

modified Porous-Solver at CG are presented in section 6.4.3. However, since the validity of the modifications is not sufficiently proven and not all issues are fully understood, the modified Porous-Solver is not further used in this work for operational or diagnostic applications. All results presented in chapter 7 are produced without consideration of bubble close-off.

6.4.1 Modification of the Porous-Solver (firn flow law)

The Porous-Solver available in the Elmer/Ice distribution solves the Stokes equations together with the compressible firn flow law using the Finite Element method. According to the Elmer/Ice source code, Gagliardini and Meyssonnier [1997] and Zwinger et al. [2007], the equations to solve are:

$$-\nabla p + \nabla \cdot \boldsymbol{\tau} = -D \vec{\mathbf{f}} \quad (6.1)$$

$$\nabla \cdot \vec{\mathbf{v}} + \kappa_{cp} p = 0 \quad (6.2)$$

with the pressure p , deviatoric stress tensor $\boldsymbol{\tau}$, relative density D (required as input), load vector $\vec{\mathbf{f}}$ (in general $\vec{\mathbf{f}} = \rho_{ice} \vec{\mathbf{g}}$, with ρ_{ice} the ice density and $\vec{\mathbf{g}}$ the gravity vector), velocity vector $\vec{\mathbf{v}}$, κ_{cp} the volume–pressure coupling [Zwinger et al., 2007] (see below equation (6.4)) and

$$\tau_{ij} = 2\eta \left(\dot{\epsilon}_{ij} - \frac{\dot{\epsilon}_m}{3} \delta_{ij} \right) \quad (6.3)$$

$$\kappa_{cp} = bB^{\frac{1}{n}} \dot{\epsilon}_D^{\frac{n-1}{n}} \quad (6.4)$$

$$\dot{\epsilon}_D^2 = 2 \frac{\dot{\epsilon}_{ij} \dot{\epsilon}_{ij}}{a} + \frac{\dot{\epsilon}_m^2}{b} \quad (6.5)$$

$$\eta = \frac{B^{-\frac{1}{n}}}{a} \dot{\epsilon}_D^{\frac{1-n}{n}} \quad (6.6)$$

where $\dot{\boldsymbol{\epsilon}}$ is the strain rate tensor, ϵ_m the trace of $\dot{\boldsymbol{\epsilon}}$, $\dot{\boldsymbol{\epsilon}}$ the deviatoric strain rate tensor, $\dot{\epsilon}_m$ the trace of $\dot{\boldsymbol{\epsilon}}$, a and b the density dependent parameters of the firn flow law, B the fluidity parameter and n the creep exponent (see section 3.5.3). Equations (6.1) and (6.2) are equivalent to equation (3.5) and (3.6) (momentum and mass conservation, see section 3.4.1), with addition of the term $\kappa_{cp} p = -\dot{\epsilon}_m$ accounting for firn compressibility. Equation (6.3) formulates the firn flow law (equal to equation (3.28) of section 3.5.3 and equivalent to equation (3.20)). More explanations for equations (6.1) to (6.6) can be found in chapter 3.

Using the Finite Element method (see the variational formulation presented in Gagliardini and Meyssonnier [1997]), the equations (6.1) to (6.6) are reduced together to the form:

$$A x = F \quad (6.7)$$

with A the *stiffness matrix* (the left-hand side of the equations), x the *solution vector* and F the *force vector* (the right-hand side of the equations). In three dimensions, a

simplified form of equation (6.7) (omitting the basis functions) is:

$$\begin{pmatrix} A_{11} & A_{12} & A_{13} & A_{14} \\ A_{21} & A_{22} & A_{23} & A_{24} \\ A_{31} & A_{32} & A_{33} & A_{34} \\ A_{41} & A_{42} & A_{43} & A_{44} \end{pmatrix} \begin{pmatrix} u \\ v \\ w \\ p \end{pmatrix} = \begin{pmatrix} F_1 \\ F_2 \\ F_3 \\ F_4 \end{pmatrix} \quad (6.8)$$

where u , v and w are the velocity components and p is the pressure.

In this work, we attempt to consider the effect of bubble close-off in the firm flow law in a simple way: not by producing a new formulation of the stiffness matrix A , but subtracting the effect of bubble close-off from the force vector F . At depths where the relative density D is higher than the close-off density D_c (see equation (3.31) in section 3.5.4), the force vector is modified to:

$$F' = \begin{pmatrix} F_1 - A_{14}p_b \\ F_2 - A_{24}p_b \\ F_3 - A_{34}p_b \\ F_4 \end{pmatrix} \quad (6.9)$$

with p_b the pressure within the bubbles, calculated using equation (3.30) of section 3.5.4.

6.4.2 Test: Application on a simple test case

Analytical solutions of a simple test case presented in this section are calculated deploying the compressible firm flow law, with and without accounting for bubble close-off (see section 3.5.3 and 3.5.4). The presented solutions are adaptations of the calculations available from the Elmer/Ice-Wiki documentation⁷ of the Porous-Solver (firm flow law). The analytical solutions are compared with numerical solutions calculated using Elmer/Ice. The aim of the comparison is to validate the implementation of bubble close-off in the Porous-Solver outlined in section 6.4.1.

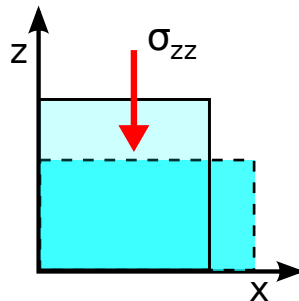


Figure 6.3: Sketch of uniaxial stress-driven compression of a cubic sample.

⁷<http://elmerice.elmerfem.org/wiki/lib/exe/fetch.php?media=solvers:poroussolver.pdf>

Uniaxial stress-driven compression test

In this example a cubic sample of firn deforms by applying a vertical stress σ_{zz} on top of the sample (see Figure 6.3), without considering gravity. The only non-zero component of the stress tensor is $\sigma_{zz} = \bar{\sigma}$. The isotropic pressure is therefore $p = -\bar{\sigma}/3$, whereas the non-zero components of the deviatoric stress tensor are: $\tau_{xx} = \tau_{yy} = -\bar{\sigma}/3$ and $\tau_{zz} = 2\bar{\sigma}/3$. Using the second invariant of the deviatoric stress tensor $\tau^2 = \bar{\sigma}^2/3$ and applying equation (3.32), the stress invariant under consideration of bubble close-off is:

$$\begin{aligned}\sigma_{D,co}^2 &= a\tau^2 + bp_{co}^2 = a\frac{\bar{\sigma}^2}{3} + b\left(-\frac{\bar{\sigma}}{3} - p'_b\right)^2 \\ &= \left(\frac{a}{3} + \frac{b}{9}\right)\bar{\sigma}^2 + \frac{2}{3}bp'_b\bar{\sigma} + bp_b'^2 =: \zeta^2\end{aligned}\quad (6.10)$$

with p'_b the increment of air pressure in the bubbles as defined in section 3.5.4, B the fluidity parameter, a and b the density dependent parameters of the compressible firn flow law (see equation (3.20)) and ζ simply an abbreviation. Using the formulation of

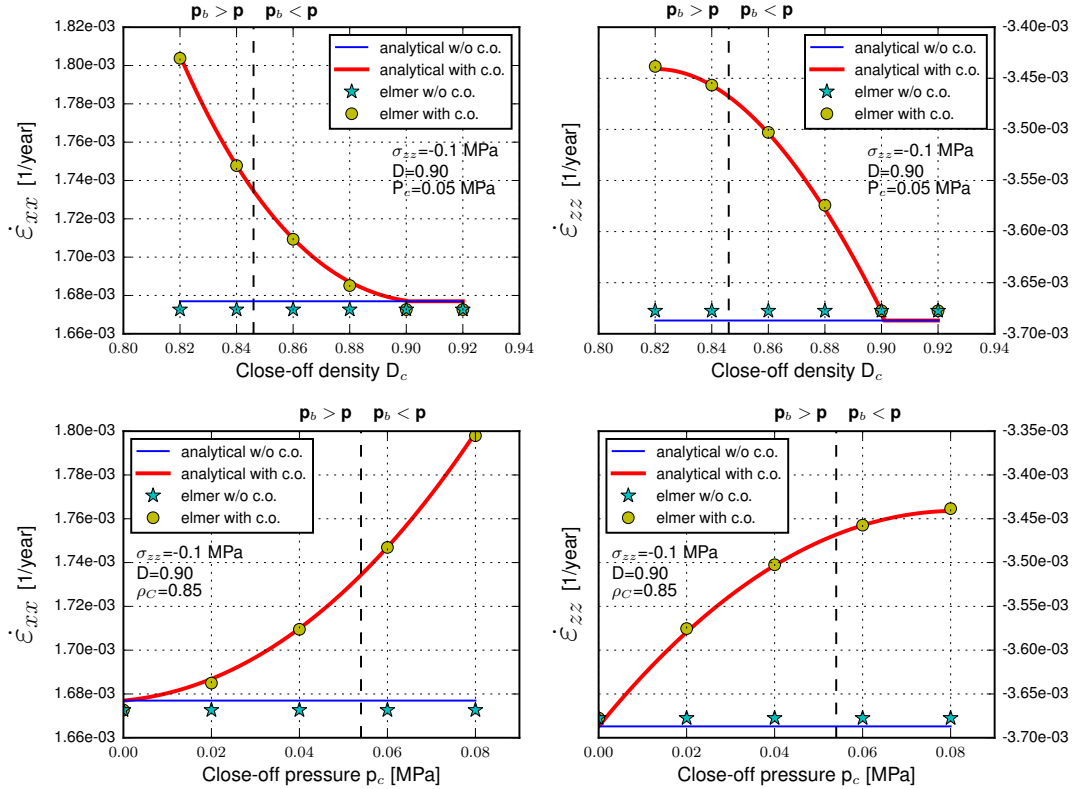


Figure 6.4: Uniaxial stress-driven compression test. Strain components calculated with and without consideration of bubble close-off for different (relative) close-off densities D_c and close-off pressures p_c . Analytical and numerical (Elmer/Ice) solutions are in good agreement. The vertical dashed line indicates the point where the bubble pressure p_b exceeds the isotropic pressure p .

the compressible flow law of equation (3.33), the strain-rate tensor components under consideration of bubble close-off are:

$$\dot{\epsilon}_{xx,co} = \dot{\epsilon}_{yy,co} = B\zeta^{n-1} \left[\left(-\frac{a}{6} + \frac{b}{9} \right) \bar{\sigma} + \frac{b}{3} p'_b \right] \quad (6.11)$$

and

$$\dot{\epsilon}_{zz,co} = B\zeta^{n-1} \left[\left(\frac{a}{3} + \frac{b}{9} \right) \bar{\sigma} + \frac{b}{3} p'_b \right] . \quad (6.12)$$

Results of the calculations are presented in Figure 6.4 for different (relative) close-off densities D_c (with $D_c = \rho_c/\rho_i$, where ρ_c is the close-off density and ρ_i the ice density) and close-off pressures p_c . The analytical solutions, with and without consideration of bubble close-off, are represented with solid lines. The numerical solutions calculated with the original Elmer/Ice Porous-Solver (firn flow law without close-off) are represented with stars, whereas solutions calculated using the modified Porous-Solver (therefore with consideration of close-off) are indicated with dots.

The numerical solutions are in good agreement with the analytical solutions. Obviously, the solutions without consideration of close-off are not influenced by close-off density and pressure. As expected, the lower is D_c or the higher is p_c , the more air is trapped in the bubbles (higher bubble pressure p_b) and the stiffer becomes the sample under vertical compression (vertical strain $\dot{\epsilon}_{zz}$ less negative). The solutions with close-off are identical to the solutions without close-off if the firn density D is lower than the close-off density D_c and if the close-off pressure p_c is zero. The vertical dashed black line marks the threshold, where the bubble pressure p_b becomes higher than the isotropic pressure p .

6.4.3 Test: Application to Colle Gnifetti

As an experiment, the modified Porous-Solver (firn flow law with consideration of bubble close-off) is applied to CG, testing different close-off densities D_c in several steady state runs with prescribed density and temperature. The prescribed density field is derived from the density profile calculated at KCC with the fully coupled model (see Figure 7.14 in section 7.3). However, the highest relative densities are limited to be $D < 0.98$, in order to avoid the bubble pressures p_b to diverge (see equation (3.30) in section 3.5.4). The prescribed ice temperature T and close-off temperature T_c are both set to -10°C throughout the whole glacier (arbitrary choice), whereas the close-off pressure p_c is set to 740 hPa [Lüthi and Funk, 2000].

Results of the test-runs are presented in Figure 6.5. The vertical velocity at the KCC drilling site is calculated for different close-off densities D_c between 0.80 and 1.00. The lower the close-off density, the more air is trapped in the bubbles and the larger is the air pressure within the bubbles. This makes the ice stiffer under compression and reduces the vertical velocity. If the close-off density is set to 1.0 (yellow line in Figure 6.5), nowhere in the glacier the bubbles are closed ($D \leq D_c$ everywhere) and the isotropic pressure is not modified by the bubble pressure (see equation (3.31) in section 3.5.4). In this case the solution is identical to the solution of the unmodified Porous-Solver

(black-dashed line).

Bubble close-off occurs typically at a firn porosity of $\phi=0.1$ [Schaller et al., 2017], corresponding to a (relative) close-off density of ca. $D_c=0.9$ ($\rho_c \approx 830 \text{ kg m}^{-3}$). According to the test results of Figure 6.5, at KCC the vertical velocity in the bottom part of the core slows down by up to a factor of two when considering bubble close-off at $D_c=0.9$. The next step in testing the close-off implementation consists in applying the modified Porous-Solver in a transient simulation of CG (with variable density and velocity). However, transient runs conducted coupling the modified Porous-Solver with the continuity equation produce irregular and unrealistic solutions. Most likely, this is an effect of densification in the basal part of the glacier, where the calculated densities approach the ice density ($D \rightarrow 1$), and the bubble pressure p_b becomes too high (by far exceeding the isotropic pressure p). No satisfying solution was found so far to overcome these instabilities, therefore all CG simulations presented in this work (see chapter 7) are produced deploying the unmodified Elmer/Ice Porous-Solver without consideration of bubble close-off.

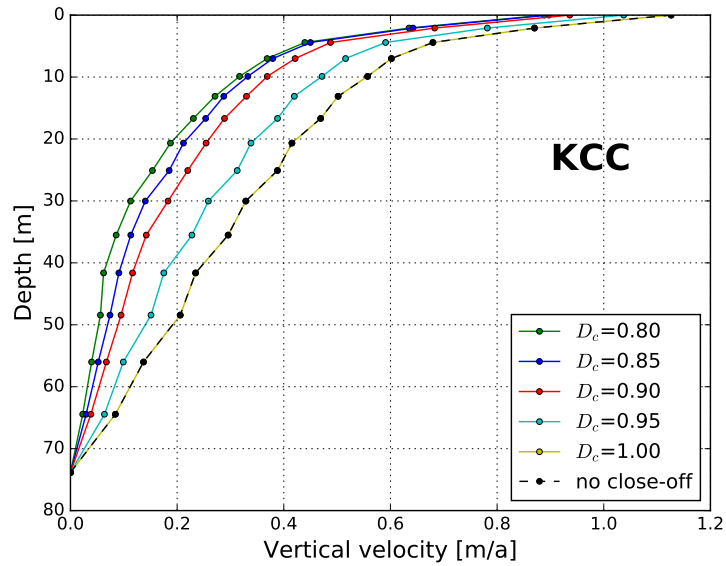


Figure 6.5: Test runs of the modified Porous-Solver (firn flow law with consideration of bubble close-off) applied at CG for different close-off densities D_c (steady state simulations with prescribed density). As expected, vertical velocities slow down at low close-off densities (exemplary results calculated at the KCC drilling site).

6.5 Attempt to combine firn and anisotropic flow law

This section describes the attempt to obtain a flow solution combining both firn and anisotropic flow law. This attempt is motivated by the particular glaciological settings of the CG glacier, with low density firn at the surface and increasingly anisotropic fabric towards the bedrock [Kerch, 2016] (see section 7.1.3). This requires consideration of both firn and anisotropic ice rheology for the correct modeling of the flow field. However, a flow law taking into account both firn and anisotropic ice rheology is not available. Developing and implementing in Elmer such a new flow law would go beyond the scope of this work.

The principle of the tests performed to combine firn and anisotropic law in the CG flow model is sketched in Figure 6.6. The tests are performed with prescribed (fixed) density field (similar to the KCC density profile) and temperature. The prescribed fabric distribution is based on the fabric measurements of the core KCC [Kerch, 2016]. The glacier is divided into two parts: the upper part is restricted to a depth where the density is lower than a threshold density ρ_{th} , and the lower part where the density is higher than ρ_{th} . The combined velocity field is calculated according to the following procedure (see Figure 6.7):

- The velocity field v_{f_0} (the subscript f stays for firn law) of the whole glacier is calculated using the firn law (red dashed line in Figure 6.7).
- The velocity field v_{a_1} (the subscript a stays for anisotropic law) is calculated using the anisotropic flow law and imposing $v_{a_1} = v_{f_0}$ for the mesh nodes in the upper part of the glacier (green dashed line). Note that the basal velocities are no longer imposed to be zero (glacier frozen to bedrock), but sliding is allowed. Otherwise the anisotropic solver would have to deal with two Dirichlet boundary conditions, $v_{a_1} = 0$ at bedrock and $v_{a_1} = v_{f_0}$ at the interface to the upper domain, which would be a problem since the anisotropic law is incompressible.
- The velocity field v_{f_1} is calculated using the firn law and imposing $v_{f_1} = v_{a_1}$ for the mesh nodes in the lower part of the glacier (blue dashed line).

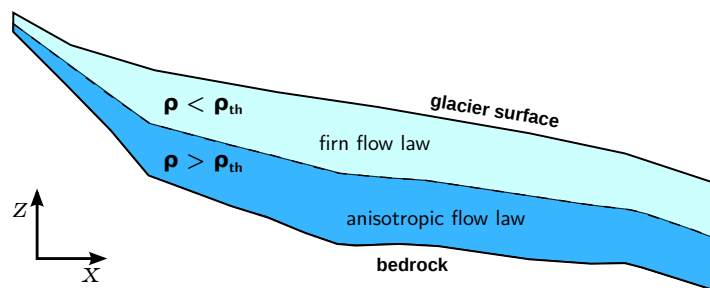


Figure 6.6: Sketch of the attempt to combine firn and anisotropic flow law. The glacier is divided into two parts: one with density lower than the threshold density ρ_{th} , where the firn flow law is applied, and one with higher density, where the anisotropic flow law is applied.

- In the next iterations, the velocity fields v_{a_i} and v_{f_i} are recalculated in alternation using the anisotropic and the firn law as outlined above. The expectation is that after a number of iterations, the velocity solutions v_{a_i} and v_{f_i} would not change anymore and converge to a stable combined solution v_{af} .

The results of these simulations are shown in Figure 6.7. The calculated velocities are representative for an exemplary glacier location (close to the western boundary). Horizontal velocity profiles calculated after different steps of the procedure are visualized with different colors. It is evident how after few iterations the velocity solution diverges (yellow dashed line). Different basal slip coefficients and threshold densities ρ_{th} were tested. In all cases it was not possible to calculate a stable solution for v_{af} , therefore in this work firn and anisotropic flow law are used separately, i.e. either the firn or the anisotropic law (see chapter 7).

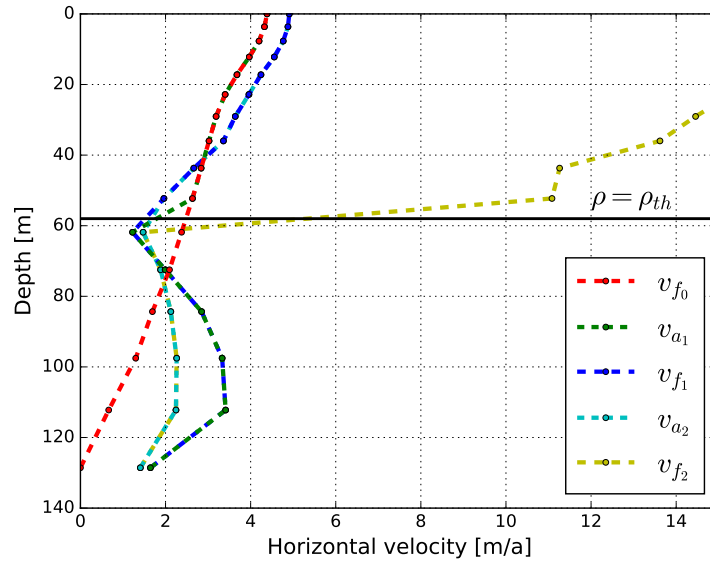


Figure 6.7: Simulation results for combined firn and anisotropic flow law. No stable solution could be achieved. The velocity solution diverges after few iterations (yellow dashed line).

7 Results: Model validation and applications

In this chapter the results of the full Stokes model applied to the CG glacier saddle are presented (50 m mesh size, 16 extrusion levels, and accounting for atmospheric temperature variations from 1901 to 2015 with a time step of one year). All calculations are produced by coupling the Stokes solver, the continuity equation and the enthalpy equation as outlined in the coupling diagrams of section 5.4. If not specified differently, the compressible firn flow law (without consideration of bubble close-off) is used. Calculated velocities (section 7.1), surface accumulation (section 7.2), densities (section 7.3) and temperatures (section 7.4) are compared with measurements in order to validate the model. Results concerning calculation of trajectories, ice-core dating and depths of equal age are discussed in the sections 7.5, 7.6 and 7.7. Excluding the temperature calculations, all presented model results are calculated for the year 2015.

7.1 Velocity field

7.1.1 Horizontal surface velocities

Horizontal surface velocities calculated using the full Stokes model are displayed in Figure 7.1, where model results (black arrows) are compared with stake measurements (red arrows). Velocities are well reconstructed in the central region of the glacier, especially along the KCH-KCS and KCC-KCI flowlines, where the most recent GPR data are available (see section 5.1.4). However, in the region close to the bergschrund, the model predicts far too slow velocities, and significant mismatch is obtained in the northern part of the glacier as well as in the southern edge, i.e. glacier sectors where bedrock and surface topography are not well known. The saddle line dividing ice flow from the southern and from the northern part of the glacier is accurately reconstructed. Further, the calculated saddle point, the point in the north-eastern part of the glacier with vanishing horizontal velocities, is well reproduced.

The generally good agreement with the stake measurements in the vicinity of the ice cliff and close to the Grenzletscher boundary, both areas characterized by sparse topography measurements, is obtained with a manual estimation of the glacier geometry (see section 5.1.3 and 5.1.4). The influence of the topography of those boundary areas on the calculated trajectories and ice-core chronologies (main goals of this work) is estimated by means of sensitivity studies (see section 7.5 and 7.6) and is included in the error estimation of the results. Figure 7.2 gives a quantitative comparison between calculated and measured surface flow velocities. For a more meaningful comparison, the nodal velocities shown in Figure 7.1 are cubically interpolated in order to assess model velocities exactly at the stake positions. The histogram on the left side of Figure

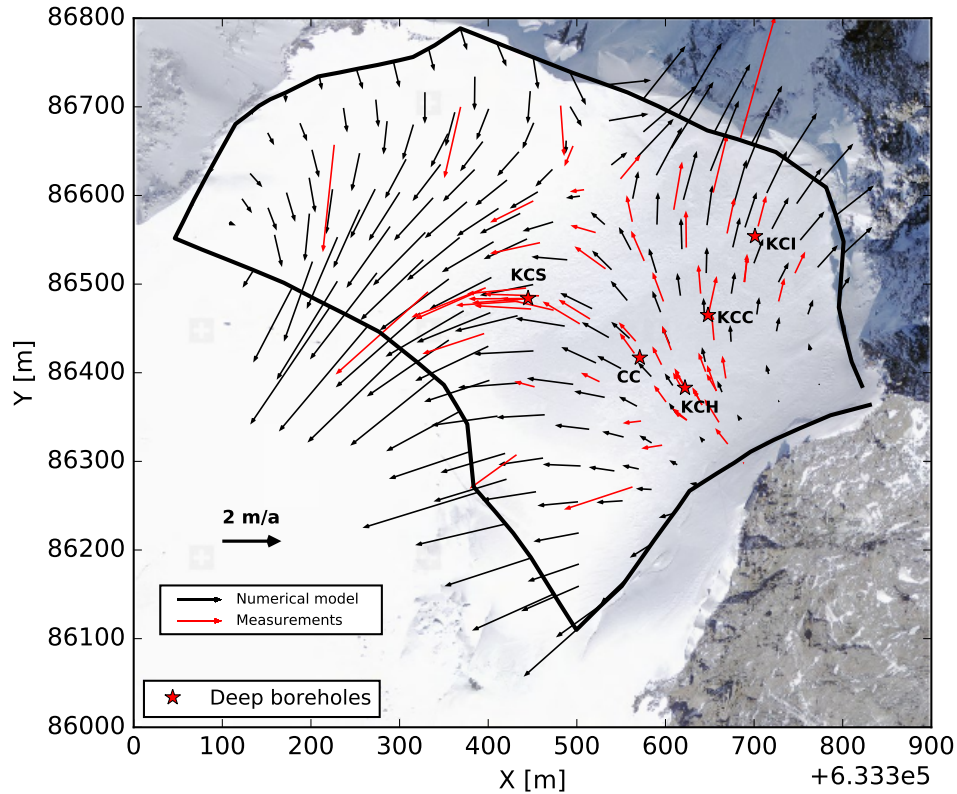


Figure 7.1: Horizontal surface flow velocities calculated at the mesh nodes (black arrows) compared with stake measurements (red arrows). The flow field is particularly well reconstructed in the area including the drilling sites. Coordinates are in the official Swiss coordinate system, with the x -coordinate pointing to the east and the y -coordinate pointing to the north. Areal imagery from <https://map.geo.admin.ch>.

7.2 shows the ratios between the magnitudes of calculated v_m (the subscript m stays for model) and measured v_s (the subscript s stays for stake) surface velocity vectors. The majority of the calculated velocity magnitudes reproduces the stake measurements with less than 50% discrepancy ($\sim 20\%$ mean discrepancy). The validity of the calculated flow directions is proven in the right histogram, showing for all stakes the angles between modeled and measured velocities. Most of the calculated directions are less than 20° misaligned with respect to the measurements ($\sim 10^\circ$ on average).

Discussion of surface velocity calculations

The calculated surface velocities close to the bergschrund are very small compared to the stake measurements (note in particular the stake just downhill of the bergschrund pointing towards the drilling site KCH). The various potential reasons for this discrepancy are not completely understood so far, so several possibilities are discussed:

- Too slow flow velocities could suggest underestimated glacier thickness at this

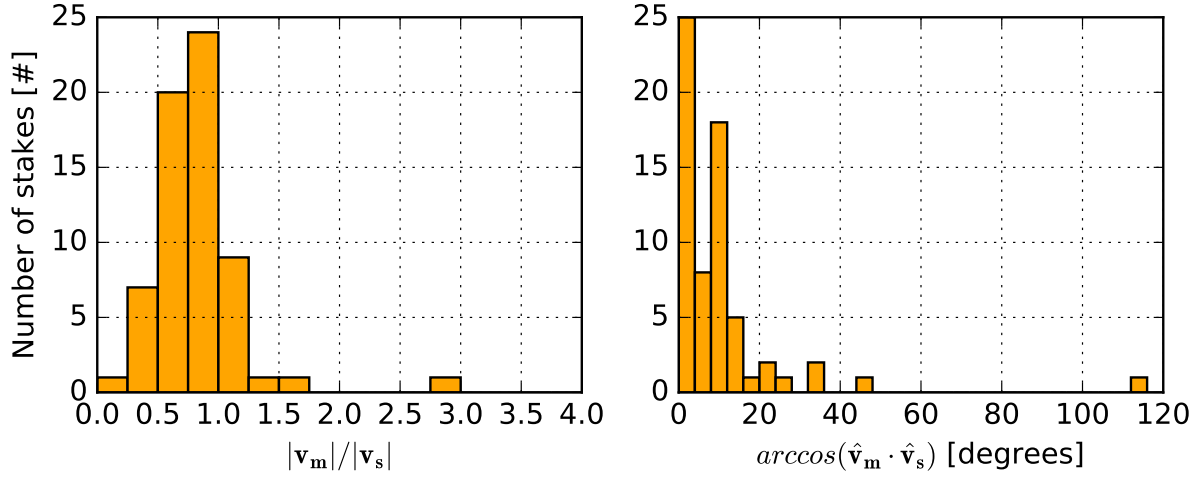


Figure 7.2: Quantitative validation of the calculated surface flow velocities (v_m modeled, v_s measured velocities). Left: validation of the velocity vector magnitudes. Right: validation of the flow directions, given as degree-deviations from the measured directions.

location, but the inspection of the open bergschrund in September 1999¹ [Keck, 2001] and recent GPR measurements in this area [pers. comm. J. Lier, 2017] are not in conflict with the bedrock topography used to run the model.

- The velocity stake measurements of this area date back to the late 1990s. At that time the bergschrund was open (the inspection of the bergschrund was performed in 1999 [Keck, 2001]), suggesting an enhanced ice flow just downstream of the bergschrund compared to the area above the bergschrund². However, in this work the bergschrund boundary is treated as stress-free, therefore the model should be better suited to describe the glacier flow with open-bergschrund, rather than with closed-bergschrund. Unfortunately, the stakes installed in 2014 in this area were lost and no velocity measurements could be performed (see section 4.1). This hampers the possibility to investigate correlations between bergschrund conditions and the local surface velocity pattern.

7.1.2 Bulk velocities (firn flow law)

Bulk flow velocities calculated with the full Stokes model at the drilling site locations KCC, KCI, KCH, CC and KCS are presented in Figure 7.3. In this subsection I discuss results using the firn flow law (blue lines), whereas results using the anisotropic flow law GOLF [Gillet-Chaulet et al., 2005] (yellow lines) are discussed in section 7.1.3. In addition, Figure 7.4 shows the different components of the strain-rate tensor $\dot{\epsilon}$ evaluated at KCC.

¹Bedrock found at 18 m depth

²Note the much higher velocity measured (over the same timespan) at the first stake below the bergschrund (upstream of KCH), compared to the only stake above the bergschrund in Figure 7.1

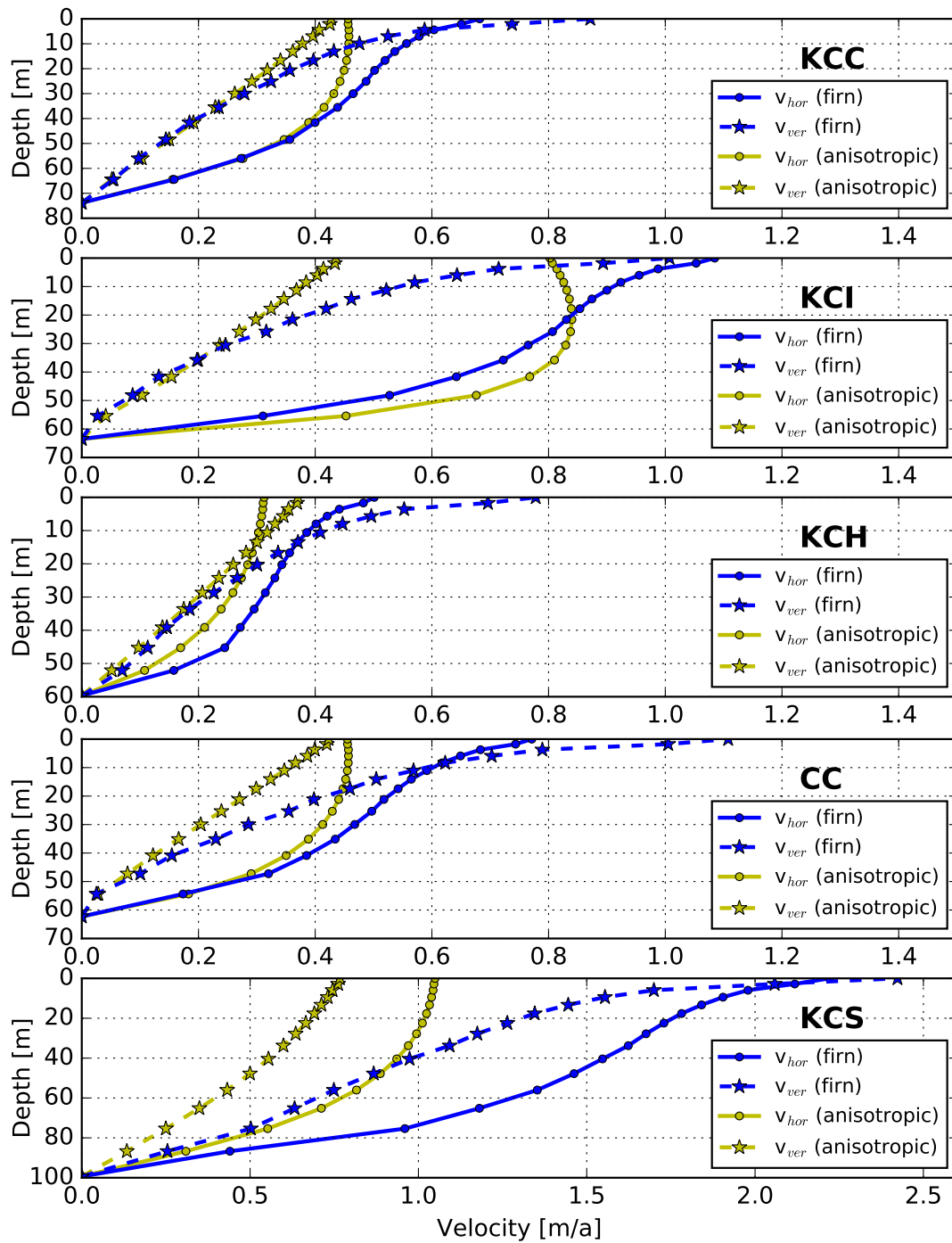


Figure 7.3: Horizontal and vertical velocities calculated at the drilling sites KCC, KCI, KCH, CC and KCS using the firn flow law (blue lines, results discussed in section 7.1.2) and the anisotropic flow law GOLF [Gillet-Chaulet et al., 2005] (yellow lines, results discussed in section 7.1.3). Note the different x-scale used for the core KCS.

Using the firm flow law, the vertical velocity profiles manifest the strongest vertical gradients close to the surface, due to the presence of low density firm, which is easy to compress (pure shear). This is also evident by looking at the vertical strain component $\dot{\epsilon}_{zz}$ calculated at KCC (blue line in Figure 7.4, left), indicating an high vertical compression at the surface ($\dot{\epsilon}_{zz} \approx -0.06 \text{ a}^{-1}$). At 20 m depth the vertical strain is much lower and already of the same order as at bedrock ($\dot{\epsilon}_{zz} < -0.01 \text{ a}^{-1}$). The nearly constant vertical strain rates calculated below 20 m correspond to the approximately linear decrease of the vertical velocity visible in Figure 7.3 ($\dot{\epsilon}_{zz} = \partial v_z / \partial z$). Inspecting the horizontal velocity profiles ($v_{hor} = \sqrt{v_x^2 + v_y^2}$) calculated using the firm flow law (Figure 7.3, blue solid lines), the strongest vertical gradients are close to the surface and close to bedrock. This is also evident when inspecting the off-diagonal components of the strain-rate tensor calculated at KCC (Figure 7.4, right). Since at KCC the prevailing ice flow is northwards (y-direction), the dominant strain-rate component is $\dot{\epsilon}_{zy}$ (simple shear in y-direction). The enhanced strain close to the surface is due to the high deformability of low density firm, whereas the strong deformation close to bedrock is due to the imposed no-slip condition (glacier frozen to bedrock, therefore $\vec{v}_{bed} = 0$).

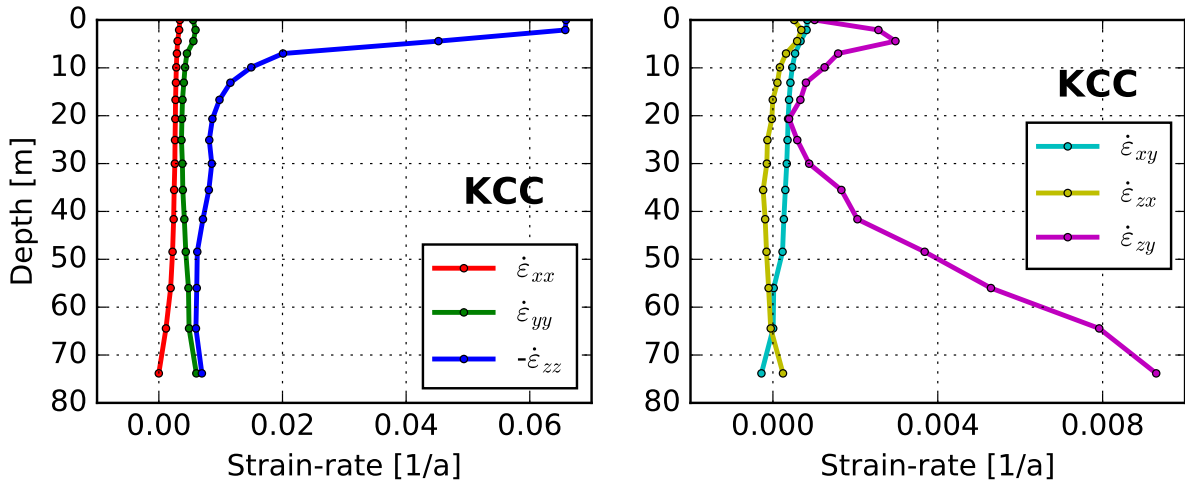


Figure 7.4: Components of the strain-rate tensor $\dot{\epsilon}$ calculated at KCC deploying the firm flow law. The most important deformations are pure shear close to the surface (vertical compression $\dot{\epsilon}_{zz}$) and simple shear near surface and bedrock ($\dot{\epsilon}_{zy}$). Note that the y -direction points to north.

Comparison with measured annual layer thickness

Assuming steady state, thus constant surface elevation and accumulation, the thickness of an annual layer is the vertical distance travelled by an ice particle in one year. Therefore, the annual layer thickness corresponds to the vertical velocity of the particle expressed in m a^{-1} ($v_{ver} \cdot 1 \text{ year} = 1 \text{ annual layer}$). Although the accumulation rate at CG is very variable from year to year, on a longer time scale the glacier can be considered in steady state (see section 5.1.2). Therefore, the comparison with measured annual

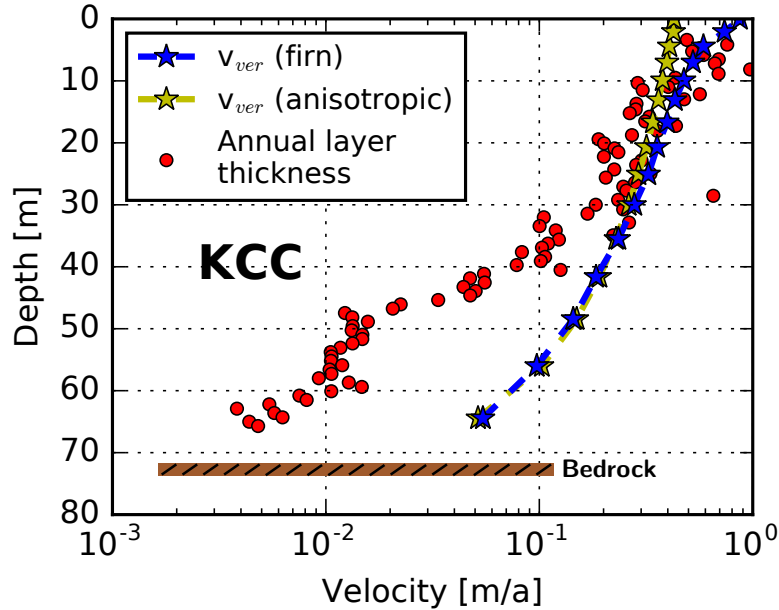


Figure 7.5: Vertical velocity calculated at the KCC drilling site using firn (blue) and an anisotropic (yellow) flow law, compared to annual layer thickness (red dots) measured at KCC using laser ablation [Bohleber et al., 2017; pers. comm. P. Bohleber, 2017]. At the bottom, measured and modelled vertical velocity largely disagree (see text and section 7.6). Note the logarithmic scale, exaggerating small differences.

layer thickness gives the opportunity to (indirectly) validate the calculated vertical velocities.

In Figure 7.5, the vertical velocity profile calculated at KCC using the full Stokes model is compared to the annual layer thickness observed at KCC (from laser ablation measurements [Bohleber et al., 2017; pers. comm. P. Bohleber, 2017]). The measured annual layer thickness decreases with depth reaching the mm-scale close to the bottom of the ice core. Note that due to the logarithmic x-axis, the velocity calculated at bedrock (set to zero as boundary condition) cannot be displayed.

By applying the firn flow law (blue line), the calculated vertical velocities and the measured annual layer thickness are consistent up to 30 m depth. Further below the model predicts velocities considerably larger than inferred from the observations, with the disagreement between both velocities reaching a factor of 10 near the bottom. Several reasons can explain this finding:

- Since the viscosity of the ice is influenced by the c -axes orientation of the ice crystals (see section 3.5.5), the observed discrepancy could be an effect of anisotropic fabric not accounted for in the full Stokes model if using the porous flow law. According to crystal-orientation fabric measurements [Kerch, 2016], the lower half of the ice core KCC is characterized by anisotropic single-maximum fabric, with the c -axes of the ice crystals roughly oriented in the vertical direction. Figure 7.5 shows the vertical velocity profile obtained deploying the anisotropic flow law

GOLF [Gillet-Chaulet et al., 2005] implemented in Elmer/Ice. For this simulation it is assumed for the whole glacier a crystal-orientation fabric distribution similar to the profiles measured at KCC [Kerch, 2016] (see Figure 7.6, more details in section 7.1.3). The vertical velocity calculated in the last 20 m above bedrock using the anisotropic law tends to be lower than using the firn law (see comparisons between the two laws at all cores in Figure 7.3). However, at KCC the anisotropic vertical velocities near bedrock are still around a factor 10 too high compared to the measured annual layer thickness.

- The model results and the validation using annual layer thickness are based on the steady state assumption. Features due to past changes in the glaciological settings of the glacier cannot be reproduced using the flow model presented in this work. The very thin layers observed at KCC below 40 m depth possibly indicate periods in the past with reduced accumulation rate³.
- The firn flow law applied in the full Stokes model does not take into account the influence of bubble close-off. Since the presence of air trapped in the bubbles makes the ice harder to compress (see section 3.5.4), calculated vertical velocities are potentially overestimated. However, preliminary results produced in this work (see Figure 6.5 in section 6.4.3) show that the influence of bubble close-off on the KCC vertical velocity about 20 m above bedrock is much smaller than the discrepancy to the observed layer thickness.
- Most likely the measured annual layer thickness does not match with the modeled vertical velocity due to disturbances of the ice flow in the basal part of KCC. Radiocarbon dating results [Hoffmann, 2016; Hoffmann et al., 2017; pers. comm. H. Hoffmann, 2017] (plotted with green dots in Figure 7.20, left) point to an age discontinuity at about 60 m depth, possibly generated by folding ice. Small-scale processes such as this are impossible to resolve using the model presented in this work. Deep thin layers may have been transported and stretched few meters upwards, destroying the relation between annual layer thickness and vertical velocity mentioned above. This finding, not fully understood so far, is discussed in more detail in section 7.6.

7.1.3 Diagnostic run using the anisotropic flow law

Crystal-orientation fabric measurements performed at the ice core KCC clearly showed the presence of anisotropic fabric at CG [Kerch, 2016]. In this section, the effect of anisotropic ice on the flow field of CG is investigated deploying the anisotropic flow law GOLF implemented in Elmer/Ice [Gillet-Chaulet et al., 2005; Gagliardini et al., 2013] (see section 3.5.5).

³According to dating results based on annual layer counting [Bohleber et al., 2017], at KCC 40 m depth corresponds to about 200 years BP (see Figure 7.20, left)

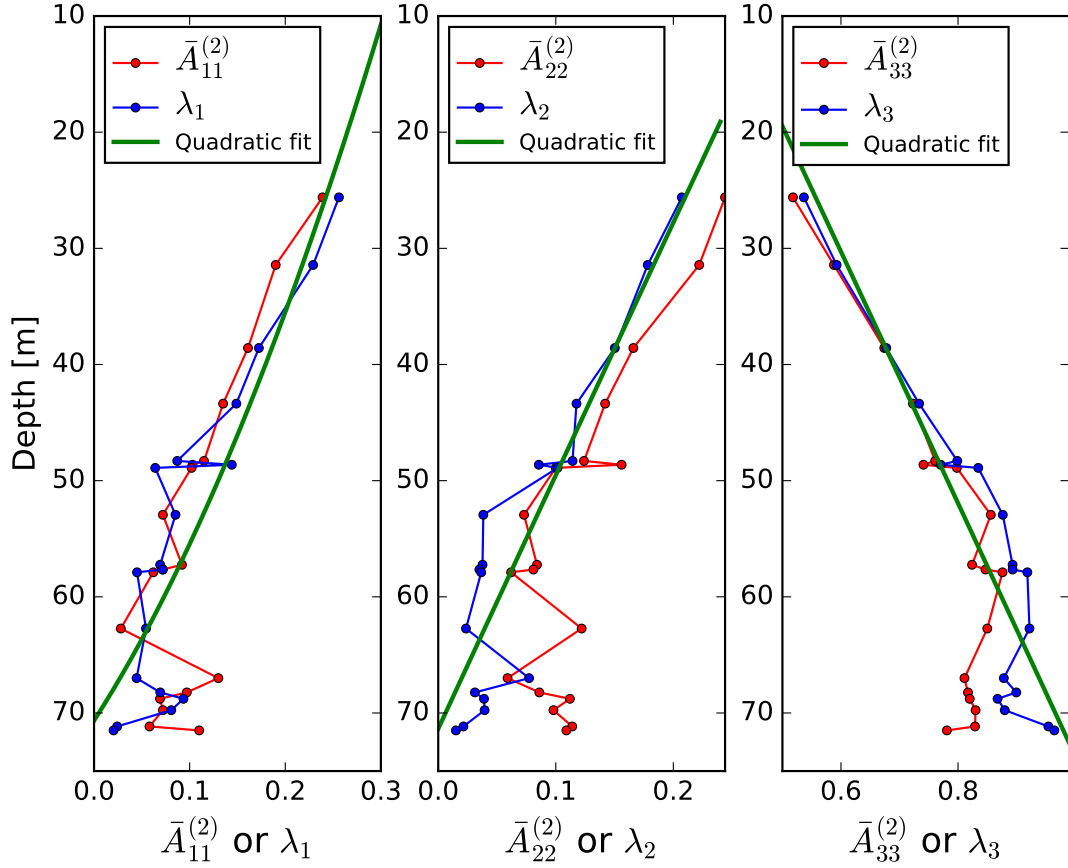


Figure 7.6: Diagonal components (red dots) and eigenvalues (blue dots) of the second-order orientation tensor $\bar{\mathbf{A}}^{(2)}$ measured at KCC (data provided by J. Kerch [pers. comm., 2016]). The green line represents the quadratic fit function to λ_i used to describe the fabric distribution in the full Stokes model.

Fabric distribution

The fabric distribution used as input for the anisotropic flow law is based on fabric data measured at the ice core KCC [Kerch, 2016]. The ice fabric is described using the second-order orientation tensor $\bar{\mathbf{A}}^{(2)}$ (see section 3.5.5). Figure 7.6 shows (with blue dots) the vertical distribution of the eigenvalues λ_i of $\bar{\mathbf{A}}^{(2)}$ measured at KCC (data from Kerch [2016]). The uppermost data point was measured at ~ 25 m depth. It is evident that the c -axes of the ice crystals tend to be oriented preferably in the vertical direction when approaching the bedrock (single-maximum in the vertical direction, therefore $\lambda_1 = \lambda_2 = 0$ and $\lambda_3 = 1$).

The anisotropic flow law GOLF requires as input the components $\bar{A}_{11}^{(2)}$, $\bar{A}_{22}^{(2)}$, $\bar{A}_{12}^{(2)}$, $\bar{A}_{23}^{(2)}$, $\bar{A}_{13}^{(2)}$ of the second-order orientation tensor $\bar{\mathbf{A}}^{(2)}$, whereas the component $\bar{A}_{33}^{(2)}$ is calculated from the other two diagonal components using $tr(\bar{\mathbf{A}}^{(2)}) = 1$. In Figure 7.6 the measured diagonal components of $\bar{\mathbf{A}}^{(2)}$ are presented with red dots (data provided by J. Kerch [pers. comm., 2016]).

For the anisotropic flow law calculations, one single fabric vertical profile is used for the whole glacier, thus assuming no horizontal dependencies of the fabric distribution. The profile used is estimated based on the fabric distribution observed at KCC. However, the orientation tensor measured at KCC is potentially influenced by the local bedrock inclination and no information is available about the azimuth of the measured core pieces [Kerch, 2016]. Therefore, the fabric distribution used as input for the flow law is the diagonalized form of the orientation tensor measured at KCC (with the eigenvalues λ_i as diagonal elements and all other tensor components equal to zero).

As evident from Figure 7.6, the vertical distribution of the eigenvalues of $\bar{\mathbf{A}}^{(2)}$ shows some variation on the meter-scale. Since in the full Stokes model the glacier geometry is subdivided into only 16 vertical layers, these short-scale variations cannot be resolved. The input fabric distribution is therefore obtained from a quadratic fit of the measured eigenvalues (see green lines in Figure 7.6). The input fabric distribution is normalized to the different glacier depths. Note that the fit is executed including a virtual measurement point at the surface, where isotropic fabric is assumed ($\lambda_{11} = \lambda_{22} = \lambda_{33} = 1/3$).

Model calculations and discussion of the results

The effect of anisotropic ice on the glacier dynamics is investigated running a steady state simulation. The anisotropic flow law is employed using a prescribed fabric distribution (see above). The temperature and density fields are prescribed as well, using temperatures and densities calculated with the firn flow law (see sections 7.3 and 7.4). Further parameters⁴ of the GOLF flow law are arbitrarily set, whereas the influence of this choice on the velocity profiles calculated at KCC is less than 25%. The velocity profiles calculated deploying the anisotropic flow law are presented in Figure 7.3 as yellow lines. Main issues to be pointed out are:

- Since the anisotropic flow law does not account for firn compressibility, the velocities calculated close to the surface (both horizontal and vertical) are much smaller than when using the firn law (around a factor of 2–3).
- Excluding the core KCI, vertical velocities calculated with the anisotropic law in the vicinity of the bedrock tend to be smaller than using the firn law (most evident at KCS). This is expected since, according to the prescribed fabric distribution, approaching the bedrock the c -axes are more oriented in the vertical direction (single-maximum). Namely, this fabric distribution makes the ice stiffer under vertical compression.
- The prescribed fabric distribution close to the surface is nearly isotropic. The profile of the calculated horizontal velocities is therefore similar to the z^4 -profile calculated using the ice-slab simplification with the isotropic Glen’s law (see section 3.5.2). However, at KCI the calculated maximum of the horizontal velocity is located not at the surface, but at ~ 20 m depth. This is an effect of the prescribed

⁴Grain anisotropy parameters: $\beta = 0.04$, $\gamma = 0.80$; stress exponent: $n = 1.0$; $\mu - M$ model: visco-plastic self-consistent (VPSC). Details in Gillet-Chaulet et al. [2005].

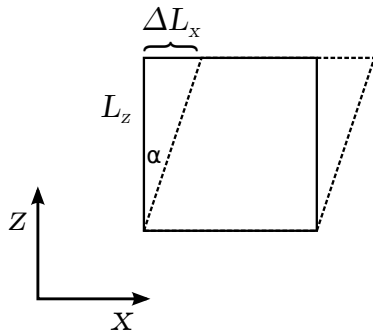
anisotropic distribution (converging to single-maximum at the bottom), by which shear is enhanced in the horizontal direction (perpendicular to the c -axes). At the KCI location this finding is more evident than elsewhere, because KCI is the only drilling site close to a stress-free downstream boundary.

Due to the highly unrealistic velocity field calculated close to the surface, the anisotropic flow law is not well suited to reproduce the flow field of CG (surface velocity calculated with the firn law is validated in section 7.1.1). According to the simulations, the role of compressible firn close to the surface is more relevant than the role of anisotropic ice in the basal part of the glacier. For this reason, the following simulation results are only produced using the firn flow law. An attempt to combine firn and anisotropic flow law is presented in section 6.5.

7.1.4 Borehole inclination angles

The velocity field calculated with the full Stokes model is used to simulate the temporal shape evolution of the boreholes KCC and KCI. From there, borehole inclination angles are calculated and compared with the borehole inclination measurements (presented in section 4.3) for a validation of the model. Assuming that the presence of the borehole has no influence on the flow pattern of the glacier, the calculations are performed in a post-processing step. The starting borehole shapes are straight and vertical, therefore it is assumed that core drilling occurred without deviations from the plumb line. Three methods are employed:

Method 1:



Method 2:

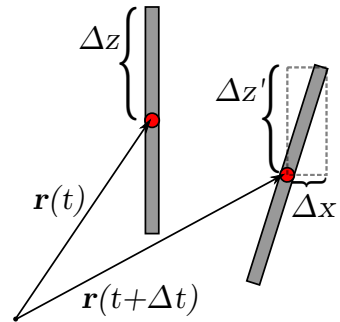


Figure 7.7: Illustration of method 1 and 2 to calculate borehole inclination angles, starting from a given velocity field. Left: simplification assuming simple shear. Right: method after Gudmundsson et al. [1999]. Synthetic tilt meters are represented in grey. Tilt meter centers are in red.

- **Method 1: approximation assuming simple shear**

Assuming simple shear in the horizontal downstream direction and neglecting horizontal gradients of velocity, the only non-zero strain components are $\dot{\epsilon}_{zx} = \dot{\epsilon}_{xz} =$

$\partial v_x / \partial z$, where the directions x and z are defined in Figure 7.7. The inclination angle α at a certain borehole depth z is calculated as follows:

$$\alpha(z) = \arctan(\Delta L_x(z)/L_z) = \arctan\left(\frac{\partial v_x(z)}{\partial z} \cdot \Delta t\right) \quad (7.1)$$

where ΔL_x and L_z are defined in Figure 7.7, left, and Δt represents the elapsed time after drilling. This method allows to estimate tilt angles without first calculating the deformed borehole shape and offers a valid approximation where simple shear dominates over pure shear (see section 3.3). In accumulation areas like at CG, simple shear dominates in the deeper layer, where the density is high and compression is negligible.

- **Method 2: after Gudmundsson et al. [1999]⁵**

The temporal shape evolution of the borehole is evaluated considering the borehole as an ensemble of particles, each following a particle path. For the sake of clarity the particles can be identified with a set of tilt meters (depicted in grey in Figure 7.7, right). The coordinate \vec{r} of the center of the tilt meter (red dots in Figure 7.7) is calculated executing a forward time integration of the local velocity field \vec{v} :

$$\vec{r}(\vec{r}_0, t + \Delta t) = \vec{r}(\vec{r}_0, t) + \vec{v}(\vec{r}(\vec{r}_0, t)) \Delta t \quad (7.2)$$

where \vec{r}_0 is the initial coordinate of the center of the tilt meter and Δt is the time step. The coordinates of the top of the tilt meter with respect to the center are $\Delta \vec{r} = (\Delta x, \Delta y, \Delta z)$ [Gudmundsson et al., 1999]. Position changes of the top of the tilt meter with respect to the center are calculated considering velocity gradients in the vicinity of the tilt meter:

$$\begin{aligned} \Delta x'(t + \Delta t) &= \Delta x(t) + \partial_z v_x(\vec{r}(\vec{r}_0, t)) \Delta z \Delta t \\ \Delta y'(t + \Delta t) &= \Delta y(t) + \partial_z v_y(\vec{r}(\vec{r}_0, t)) \Delta z \Delta t \\ \Delta z'(t + \Delta t) &= \Delta z(t) + \partial_z v_z(\vec{r}(\vec{r}_0, t)) \Delta z \Delta t \end{aligned} \quad (7.3)$$

Different from Gudmundsson et al. [1999], we neglect horizontal velocity gradients. Finally, borehole inclination angles (e.g. in the x -direction) are calculated:

$$\alpha = \arctan(\Delta x' / \Delta z') \quad (7.4)$$

Note that the calculated angles are essentially not influenced by the choice of Δz .

- **Method 3: using the ParticleDynamics-Solver⁶ within Elmer**

The ParticleDynamics-Solver is deployed to calculate the path of particles acting as passive tracers of the flow field. The particles are initially positioned along a straight vertical line, imitating the shape of the borehole just after drilling. The solver calculates the position of the particles changing with time and, considering

⁵In this work with few modifications

⁶See Elmer Models Manual [Råback et al., 2017]

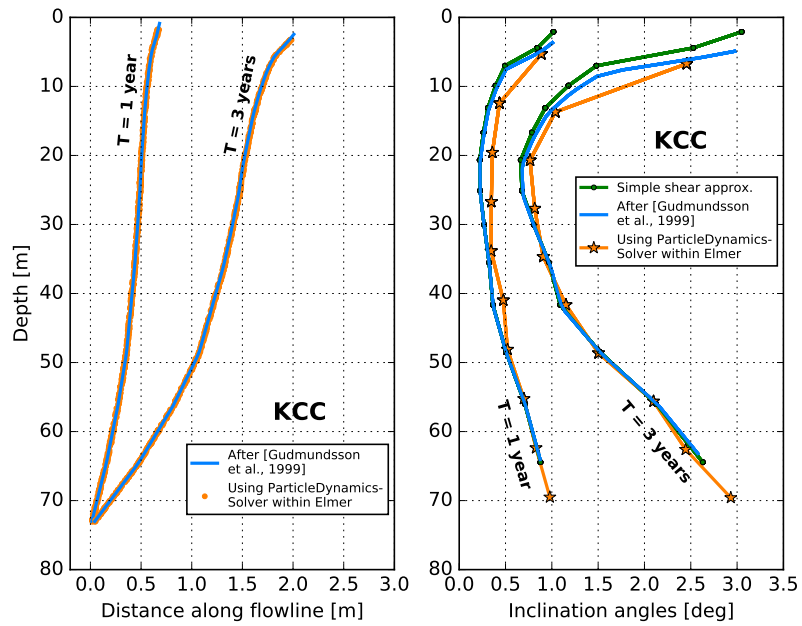


Figure 7.8: Calculated borehole deformation at the drilling site KCC. Left: borehole shape evolution after 1 and 3 years using method 2 and 3 (1000 particles). Right: calculation of borehole inclination angles after 1 and 3 years using method 1, 2 and 3.

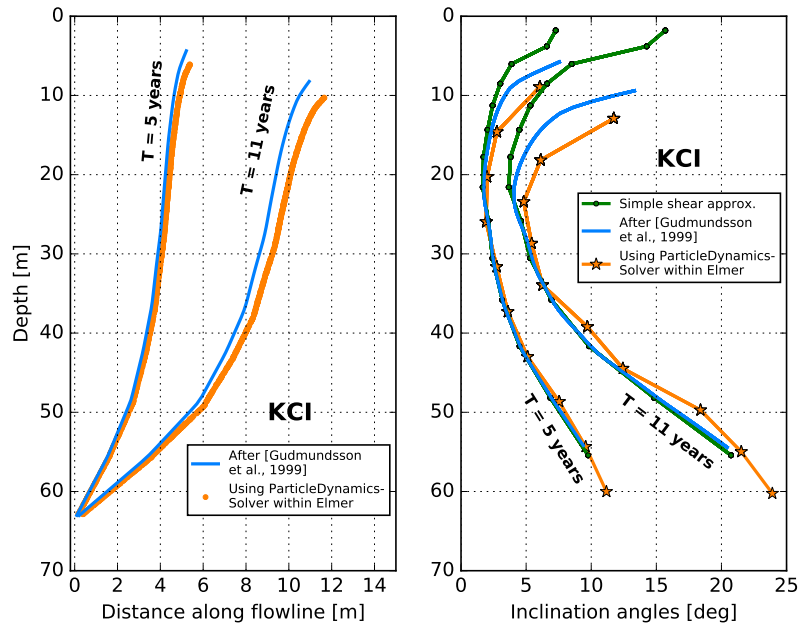


Figure 7.9: Calculated borehole deformation at the drilling site KCI. Left: borehole shape evolution after 5 and 11 years using method 2 and 3 (1000 particles). Right: calculation of borehole inclination angles after 5 and 11 years using method 1, 2 and 3.

all particles together, the deformation of the line representing the borehole. The inclination angles are determined by fitting the calculated borehole shape with a piecewise linear function and evaluating the slope of each linear segment (segments equally distributed in the vertical direction).

Vertical velocity profiles used to perform the calculations with methods 1 and 2 are plotted in Figure 7.3 (model results using the firn flow law). The required velocity gradients are determined at the nodes using a central differencing scheme:

$$\left. \frac{\partial v}{\partial z} \right|_i = \frac{v_{i+1} - v_{i-1}}{z_{i+1} - z_{i-1}} \quad (7.5)$$

where i represents the node index along the borehole, v the velocity component to be differentiated and z the vertical coordinate (no gradients can be calculated at the first and last node). Moreover, velocities and gradients used in method 2 are linearly interpolated with 1 m spacing from the nodal values. All time integrations are performed using a time step size of one year ($\Delta t=1$ a).

Results and comparison with inclination measurements

Borehole shapes calculated using method 2 and 3 are presented in Figure 7.8 and 7.9 (both left). The time integration is stopped according to the age of the boreholes at the time of the measurements in September 2016 (three years for KCC and 11 years for KCI). Inclination angles calculated at KCC and KCI using all three methods are presented in Figure 7.8 and 7.9 (both right). Note that using the methods listed above, no inclination angles can be evaluated just above bedrock. This is because the velocity gradients cannot be evaluated at the boundaries (see equation (7.5)). Moreover, the lowermost angle calculated with method 3 is evaluated at half height of the lowermost segment used for the piecewise linear fit. According to the calculations, the boreholes are most inclined close to the surface and close to the bedrock, whereas they are almost vertical at middle depths.

The calculated borehole inclination angles are compared with inclination measurements in Figure 7.10 and 7.11. Details about borehole inclination measurements can be found in section 4.3. Calculated inclination angles at the borehole KCC are (about 3°) systematically smaller than the measured angles and not within the 1σ -error. On the other hand, inclination angles calculated at the borehole KCI are consistent, especially at middle depths, with the measurements of September 2016 (11 years after drilling).

Discussion of borehole inclination calculations

The three deployed methods produce results consistent with each other and are in accordance with the velocity profiles of Figure 7.3 used as input (model results using the firn flow law):

- The calculated borehole shapes are most inclined close to the surface and close to the bedrock, since here the vertical gradients of velocity are strongest (see Figure 7.3).

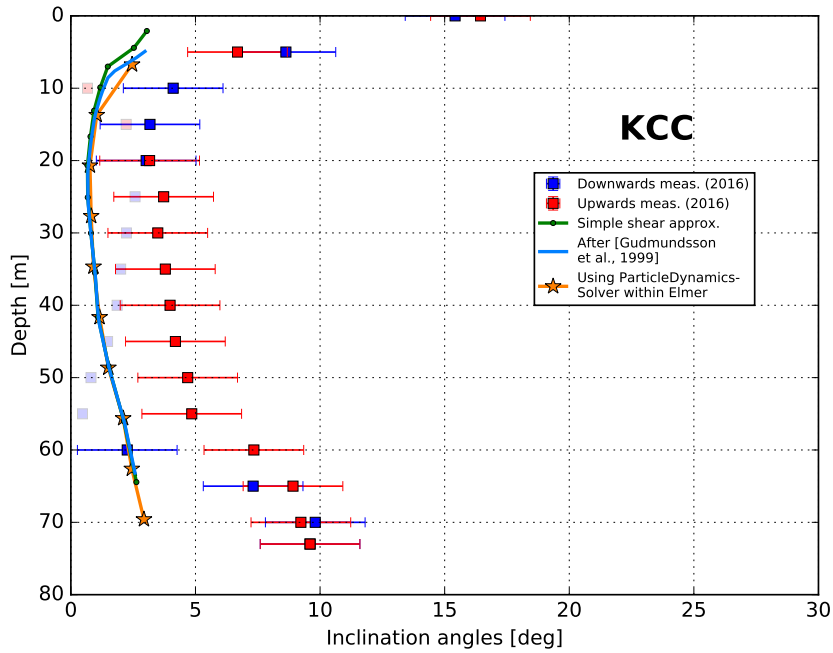


Figure 7.10: Validation of calculated inclination angles at KCC by comparison with measurements of September 2016 (see section 4.3). The calculated angles are about 3° systematically smaller than the measured.

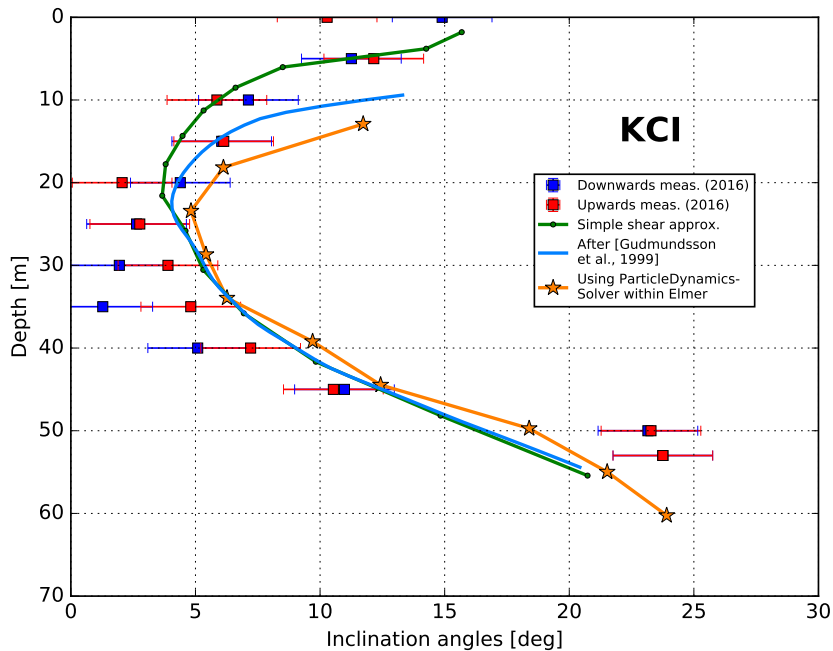


Figure 7.11: Validation of calculated inclination angles at KCI by comparison with measurements of September 2016 (see section 4.3).

- Borehole shapes calculated using method 2 and 3 are nearly identical. Differences at the borehole KCI are more visible than at KCC, since the borehole KCI is much older and requires an almost four times longer integration time.
- The agreement between inclination angles calculated with method 1 (only simple shear) and method 2 (simple and pure shear) is very good below 20 m depth, where simple shear is the dominating deformation process. This indicates the validity of the simple shear approximation at depths far from the surface. Moving closer to the surface, pure shear becomes more important due to the high compressibility of low density firn, therefore there the two methods produce discordant results. Figure 7.3 (results using the firn flow law) indicates that $\partial v_z / \partial z$ (and therefore the pure shear component $\dot{\epsilon}_{zz}$) is highest close to the surface.
- Inclination angles calculated using method 3 show few instabilities, most likely related to small differences in the path length of neighbouring particles calculated with the ParticleDynamics-Solver.
- Considering the specific flow field characteristics of the KCC-KCI area and the short integration times required (at most 11 years with 1 m a^{-1} surface velocity), the method after Gudmundsson et al. [1999] (method 2) produces the most reliable results, since it accounts for both simple and pure shear, and it is more stable than method 3.

At KCI, at depths between 10 and 50 m, the calculated borehole inclination angles are within the 1σ -error range of the measurements, whereas at KCC a systematic shift of around 3° is evident:

- Excluding issues with the calibration of the inclinometer [Ryser et al., 2014], the systematic shift is possibly referable to the initial borehole shape, which is assumed for the calculations to be vertical just after drilling, but possibly slightly out of the plumb in reality.
- At KCC the model calculations predict very small inclination angles (less than 2°) in the 10–50 m depth range three years after drilling. As discussed in section 4.3, issues due to mispositioning of the inclinometer probe inside the borehole are enhanced if the measured angles are small. Since the deployed measuring methods are not precise enough (signal to noise ratio too small), a meaningful validation of the calculated velocity field is not possible at the KCC site.
- Similar to KCC, at KCI no measurements of the borehole shape just after drilling are available. However, at KCI the influence of the assumed initial borehole shape is less significant than at KCC, since the KCI borehole is almost four times older (larger inclination angles) and signs of possible non-vertical drilling are smeared out.
- At KCI the angles calculated close to the surface are slightly larger compared to the measurements (method 2). This observation is consistent with the too high

surface accumulation predicted by the model at this location (see section 7.2) and is related to the imprecise geometrical definition of the ice cliff boundary.

7.2 Surface accumulation

In this section the velocity field calculated with the full Stokes model is validated in the vicinity of the glacier surface with respect to the surface accumulation rate. The accumulation regime of the glacier is reconstructed by inserting the calculated velocity field in the free-surface equation (3.9) (see section 3.4.3) with a fixed surface elevation because of the steady state assumption ($\partial s/\partial t=0$). With this procedure, the calculated accumulation rate represents the accumulation necessary to hold a steady surface elevation. Results of the calculation are presented in Figure 7.12. As expected, the accumulation decreases while moving upstream from the saddle region towards the southern bergschrund. Furthermore, snow accumulation in the northern half of the glacier is significantly higher than in the southern half. As already outlined in section 5.1.3 and 5.1.4, the geometry of the ice cliff and Grenzgletscher boundary is poorly constrained by measurements and is therefore manually adjusted in order to get (in those areas) surface velocity and accumulation rates in agreement with the field observations. The influence of the ice cliff and Grenzgletscher boundary geometry on the calculated trajectories and ice-core chronologies (main goals of this work) is estimated

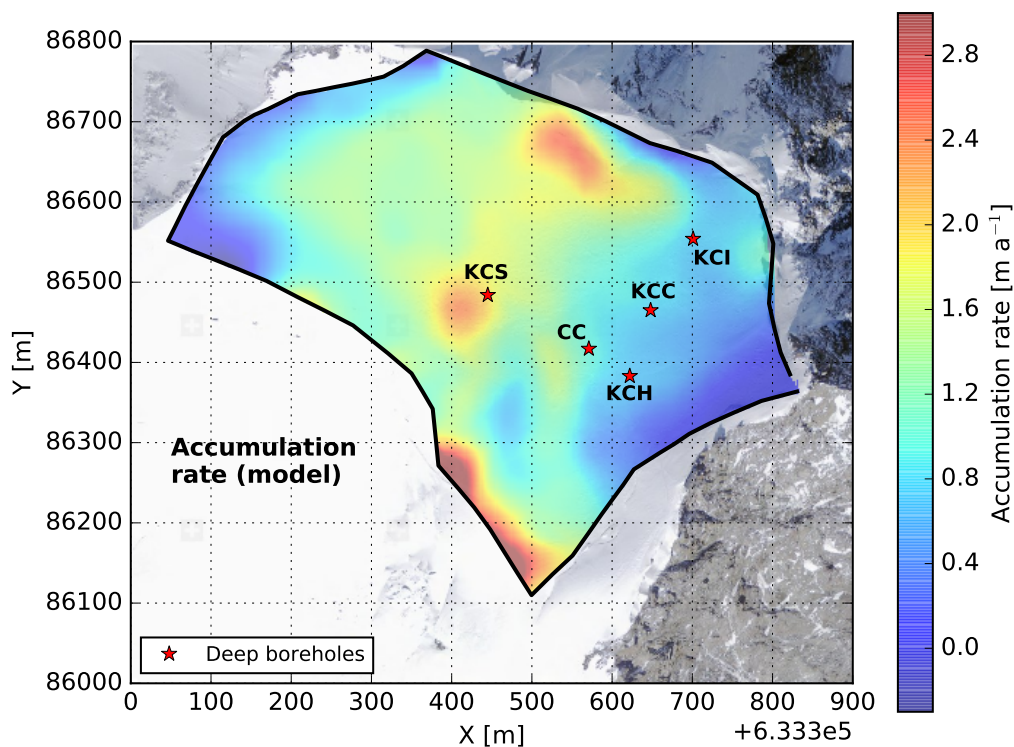


Figure 7.12: Surface accumulation rate calculated using the free-surface equation and assuming steady glacier geometry (expressed in absolute m a^{-1}).

Table 7.1: Comparison of accumulation rates derived from ice-core measurements with accumulation rates calculated at the drilling sites using the numerical model. The measured accumulation rates have an uncertainty of at least 10% [pers. comm. P. Bohleber, 2017]. The modeled accumulation rates are expressed in m w.e. a^{-1} to facilitate the comparison. The conversion from m a^{-1} to m w.e. a^{-1} is done assuming surface firn densities of 360 kg m^{-3} (as the surface density boundary condition used in the model).

Ice core	Accumulation (ice core) [m w.e. a^{-1}]	Accumulation (model) [m w.e. a^{-1}]	Ratio $\text{Acc.}_{model} / \text{Acc.}_{ice\ core}$
KCC	0.22 ¹	0.28	1.27
KCI	0.14 ²	0.27	1.93
KCH	0.23 ²	0.25	1.09
CC	0.22 ²	0.36	1.64
KCS	0.51 ²	0.70	1.37

¹ [Bohleber et al., 2017]

² [Bohleber et al., 2013]

by means of sensitivity studies and is included in the error estimation of the results (see section 7.5 and 7.6). Due to difficulties in defining the model geometry close to the boundaries, few artefacts are evident, like for instance negative accumulation at the north-western edge of the modeling domain.

In Table 7.1 surface accumulation rates calculated at the drilling sites are pointwise compared with accumulation rates derived from ice-core measurements [Bohleber et al.,

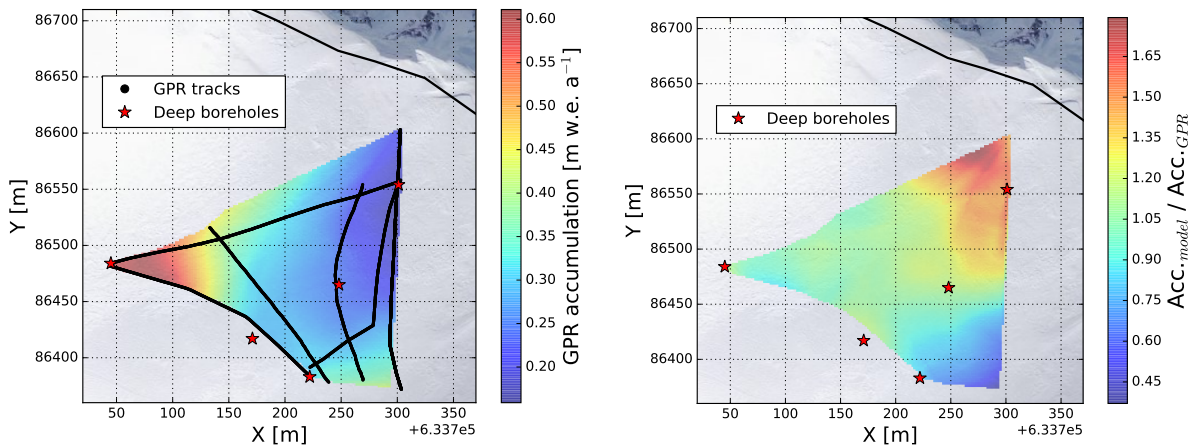


Figure 7.13: Left: accumulation rates derived from GPR profiles [Konrad, 2011; Konrad et al., 2013]. The position of the GPR tracks is marked with black dots. The data are cubically interpolated. Right: ratio between model calculated and GPR-derived accumulation rate.

2013, 2017]. The comparison shows that the calculated accumulation rates are consistent with the glaciological settings of CG, however the presence of a systematic overestimation is also evident. The calculated accumulation rates are further validated using GPR-derived surface accumulation data [Konrad, 2011; Konrad et al., 2013]. The GPR-derived accumulation rates are cubically interpolated and are illustrated in Figure 7.13, left. The data are converted from m w.e. assuming a surface density of 360 kg m^{-3} (as the density boundary condition in the full Stokes model). Figure 7.13 (right) shows the ratio between model-derived and GPR-derived accumulation. The accumulation rate is well reproduced in the area between the ice cores, whereas discrepancies are evident approaching the bergschrund (underestimation) or close to the KCI drilling site (overestimation).

Discussion of surface accumulation calculations

According to the comparisons with ice-core derived accumulation rates shown in Table 7.1, the full Stokes model tends to overestimate surface accumulation in the area including the drill sites. Moreover, according to Figure 7.13 (right) surface accumulation is overestimated in the vicinity of the KCI drilling site and underestimated close to the bergschrund. Possible reasons of these discrepancies are listed below:

- The very low accumulation rates calculated in the region just below the bergschrund are a consequence of the very low modeled flow velocities in this area (see discussion in section 7.1.1). If the ice flows downhill very slowly, low accumulation rates are sufficient to keep the surface at a constant height.
- Since calculated flow velocities in the region below the bergschrund tend to be too low, the ice outflowing from the drilling sites area is not sufficiently compensated by ice inflowing from further uphill. Therefore the accumulation needed to keep the surface altitude stable tends to be too high.
- The overestimated accumulation rates in the KCI area are most likely related to the poorly known bedrock and surface topography close to the ice cliff. Overestimated accumulation in this area implies too much outflow across the ice cliff. This is potentially, but not necessarily, in contradiction with the velocity vectors shown in Figure 7.1, where the model seems to underestimate flow velocities across the ice cliff. The velocity in the vicinity of the ice cliff was measured only with one stake (in the early 1980s [Haeberli et al., 1988]). Moreover, flow velocities in the vicinity of the ice cliff are potentially subject of abrupt accelerations, when calving events are approaching.
- The mean accumulation rate measured at the ice core KCI is $14 \text{ cm w.e. a}^{-1}$ [Bohleber et al., 2013], around half of the $27 \text{ cm w.e. a}^{-1}$ predicted by the model. However, the accumulation rate observed in the period 1977–2005 ($\sim 17 \text{ cm w.e. a}^{-1}$) is twice as high when compared to the period 1901–1977 ($\sim 9 \text{ cm w.e. a}^{-1}$) [Bohleber, 2008]. The surface elevation of this area could have changed in the last years according to changes in the accumulation regime. Since the surface topography

used in this work is based on measurements of the period 2014–2016 (see section 4.2), the accumulation rates calculated in the KCI area are possibly more representative for the recent accumulation regime.

7.3 Density field

The density field calculated with the full Stokes model is validated by comparison with density profiles measured at five deep ice cores. A density profile similar to the KCC density profile is used for the whole glacier as initial condition in the model, with vertical scaling according to the different glacier depths within the modeling area. Furthermore, the density boundary condition at the surface is fixed to 360 kg m^{-3} , without any hori-

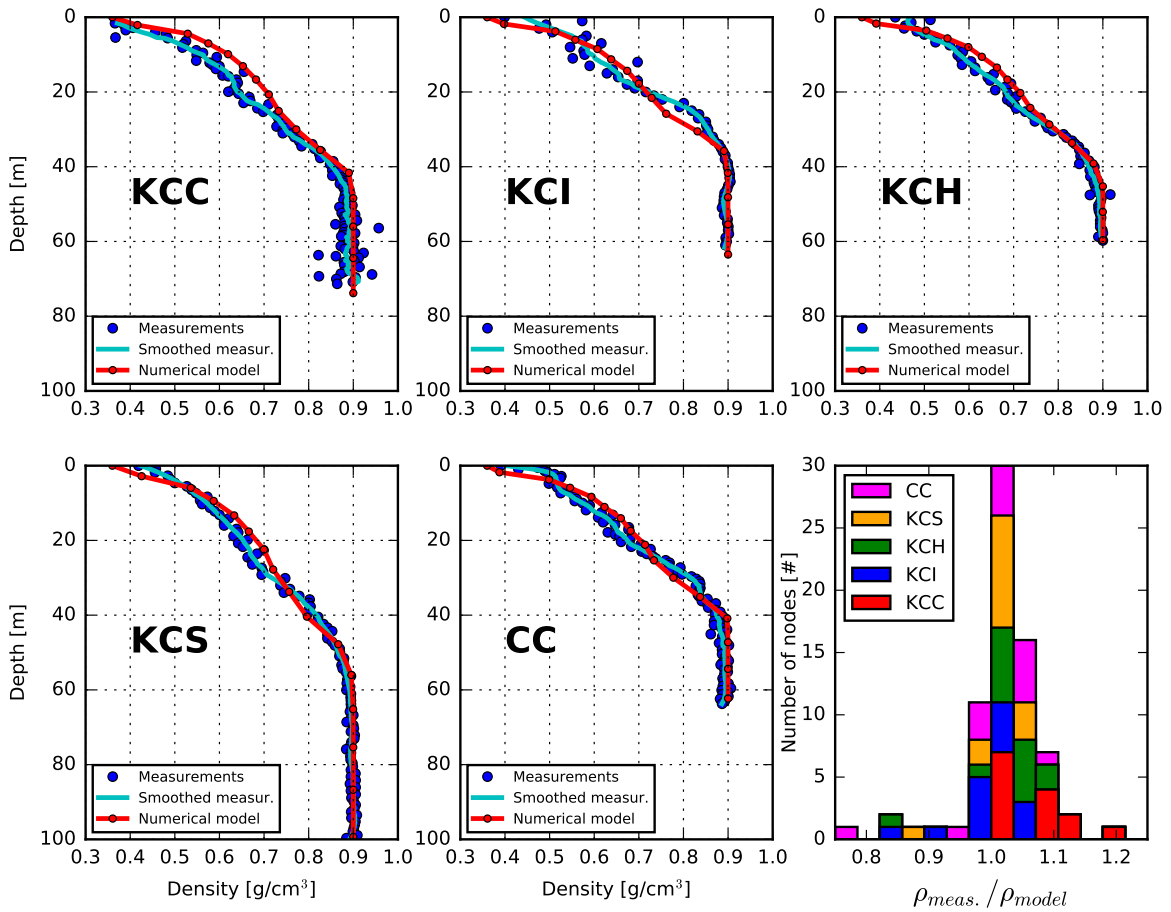


Figure 7.14: Comparison between calculated (red lines) and measured density profiles. Measured densities are shown as blue dots. The cyan lines represent the smoothing of the measurements applying the Savitzky-Golay filter available within SciPy (<https://www.scipy.org/>). Discrepancies between model simulations and measurements are quantified in the histogram in the bottom-right panel. Relative densities D are converted to absolute densities ρ using $\rho_{ice} = 900 \text{ kg m}^{-3}$.

zontal variation.

Results of the density calculations are presented in Figure 7.14. The blue dots represent the densities measured at the ice cores [IUP glaciology group database]. Smoothed density profiles are plotted as cyan lines, whereas the red lines represent the model results. The calculated density profiles are in good agreement with the measurements. Noteworthy is the good agreement of the position of the firn–ice transitions (partially with exception of the core KCI), both at cores located in areas with lower accumulation like at CC, as well as with higher accumulation like at KCS. Figure 7.14 shows in the bottom-right panel a quantitative comparison between model calculations and measured data for all five ice cores. Most of the calculated densities deviate less than 10% from the measured data.

Discussion of density calculations

The shape of the calculated density profiles are quite similar for all drilling sites. Furthermore, densities are overestimated or underestimated at all five ice cores in a similar way:

- Moving from the surface towards bedrock, the model tends to overestimate firn density (by less than 0.05 g cm^{-3}) in the first third of the core depth. Density profiles calculated in Gilbert et al. [2014a] at the Col du Dôme glacier (using Elmer/Ice and the same flow law implementation) show a similar behaviour. Possibly, this mismatch is caused by the parametrization used for low relative densities of $a(D)$ and $b(D)$ in the firn flow law (see Figure 3.6, right, in section 3.5.3).
- In the second third of the core depth, the calculated densities are slightly underestimated compared to the measurements. This observation, most evident at KCI and KCS (the drilling sites most close to the model outflow boundaries), suggests too much ice outflow (producing at the same time too high surface accumulation as shown in Table 7.1), most likely due to an inaccurate geometrical definition of the ice cliff and the Grenzletscher boundary.

7.4 Temperature field

The temperature field of CG is calculated with the full Stokes model accounting for atmospheric temperature changes since 1901 and heat sources due to refreezing of meltwater with a time step size of one year (see section 5.4 for more details). For this reason, the calculated temperatures correspond to temperatures averaged over the whole calendar year. At times and locations where measurements are available, model calculated temperatures are output along vertical lines representing the boreholes. Englacial temperature profiles calculated with the model are presented in Figure 7.15 with dashed lines and stars, whereas the measured profiles are represented with solid lines and circles. More details about the measured profiles are given in Table 7.2. Following the system introduced in Hoelzle et al. [2011], a code is assigned to each measured profile. The code identifies the borehole, the year of drilling and when the measurement was

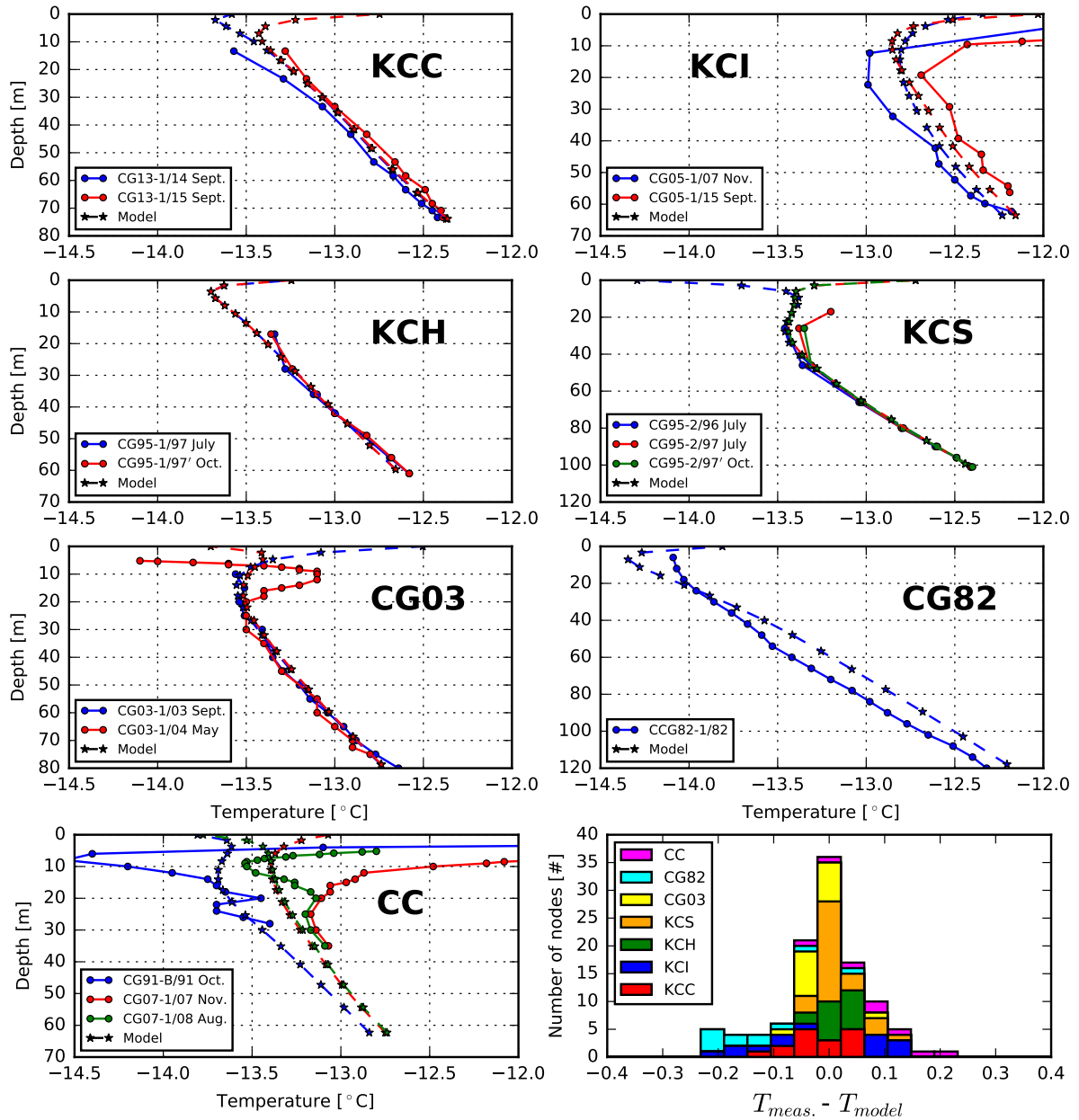


Figure 7.15: Comparison between calculated (dashed lines with stars) and measured (solid lines with circles) temperature profiles. The borehole locations are indicated in the map of Figure 5.7 in section 5.3.1. The absolute uncertainty of the measurements is up to $\pm 0.2\text{K}$ [Hoelzle et al., 2011]. Basic information about the measured profiles can be found in Table 7.2. The histogram (bottom-right panel) shows discrepancies between modeled and measured temperatures below the ZAA-depth (20 m, where seasonal temperature fluctuations are vanishing). Note the different scale on the y -axis.

Table 7.2: Basic information about the measured temperature profiles used to validate the model results (data from Hoelzle et al. [2011] and Bauder et al. [2017]). The code used to identify the measurements follows the system introduced in Hoelzle et al. [2011]. The locations of the boreholes are indicated in the map of Figure 5.7 in section 5.3.1.

Measurement code	Location name	Date of measurement	Max. depth of profile [m]	Ice-core length [m]
CG13-1/14 ¹ CG13-1/15 ¹	KCC	Sept. 2014 Sept. 2015	73	72
CG05-1/07 CG05-1/15 ¹	KCI	Nov. 2007 Sept. 2015	62	62
CG95-1/97 CG95-1/97'	KCH	July 1997 Oct. 1997	61	60
CG91-B/91 CG07-1/07 CG07-1/08	CC	Oct. 1991 Nov. 2007 Aug. 2008	35	64
CG95-2/96 CG95-2/97 CG95-2/97'	KCS	July 1996 July 1997 Oct. 1997	101	100
CG03-1/03 CG03-1/04	CG03	Sept. 2003 May 2004	80	80
CG82-1/82	CG82	1982	120	120

¹ Measurements performed by the Physical Geography Group at the University of Fribourg, Switzerland, in the frame of IUP Field campaigns within this work.

performed. For example, the code CG13-1/14 means: borehole number 1 drilled at CG in 2013 and measured in 2014. Some locations were surveyed several times. Either several times the same borehole, or several boreholes were drilled approximately at the same location (like at CC). The locations of the borehole sites are indicated in the map of Figure 5.7 in section 5.3.1.

The agreement between calculated and measured temperatures below the ZAA-depth⁷ is very good. The histogram in the bottom-right corner of Figure 7.15 shows that the discrepancies below the ZAA-depth are in most cases lower than 0.1 K, therefore of the same order of the measuring accuracy (± 0.2 K according to Hoelzle et al. [2011]).

Discussion of temperature calculations

The main goal of the temperature calculations is to produce a temperature field in accordance with the measured temperature profiles. A reliable temperature field is

⁷Depth of Zero Annual Amplitude, around 20 m, where seasonal temperature fluctuations are less than ± 0.1 °C [Hoelzle et al., 2011]

required to determine a reliable (temperature dependent) fluidity parameter B in the firn flow law (see section 3.5.3). Thermodynamic boundary conditions are accordingly adjusted (see section 5.3). The agreement between modeled and measured temperature profiles below the ZAA-depth is therefore very good. Further, the following points are worth mentioning:

- Above the ZAA-depth seasonal temperature fluctuations take place. The present model cannot reproduce these variations due to the coarse temporal resolution of the simulations (the model runs with a time step of one year and using yearly averaged air temperatures). The reconstruction of seasonal temperature fluctuations goes beyond the scope of this work.
- The model is able to reconstruct multi-year temperature trends. The temperature profiles calculated at the drilling sites KCI and CC, the only locations surveyed several times within a long time span, reproduce well the measured warming trend of glacial temperatures.
- The calculated temperatures show no systematic shifts towards lower or higher values, except for the location CG82. I decided not to tune the spin-up surface temperatures accordingly, since there are no evident physical reasons to motivate lower surface temperatures at this location.

7.5 Calculation of trajectories

The calculation of backward trajectories starting from the drill sites is one of the main objectives of this study. This is required in order to map source regions on the glacier surface and evaluate upstream effects (see chapter 1). Ice particle trajectories presented in this section are calculated in a post-processing step, using the velocity field determined with the full Stokes model. The calculations are performed using the Runge-Kutta 4-5 integrator implemented in the stream tracer of ParaView⁸ [Ahrens et al., 2005]. The maximal step size is 1 m. Stream lines stop when crossing a boundary, or at latest after 2000 steps.

Calculated backward trajectories starting from the drilling site KCC are shown in Figure 7.16. In order to support a representation in two dimensions, the horizontal coordinates are expressed as distance from the drill site. The plotted surface and bedrock profiles correspond to the surface and bedrock DEM used to run the full Stokes model. The starting depths of the trajectories are indicated left of the borehole (Figure 7.16), whereas the calculated source regions are marked with red dots. According to the calculations, the ice retrieved at KCC at a depth of about 70 m was originally deposited at the glacier surface in the vicinity of the bergschrund.

Calculated source regions of the ice cores KCC and KCI are shown in aerial view in Figure 7.17 with red dots (coordinates of the source points can be found in appendix A.5). The numbers beside the dots indicate the corresponding depths in the ice cores.

⁸<https://www.paraview.org/>

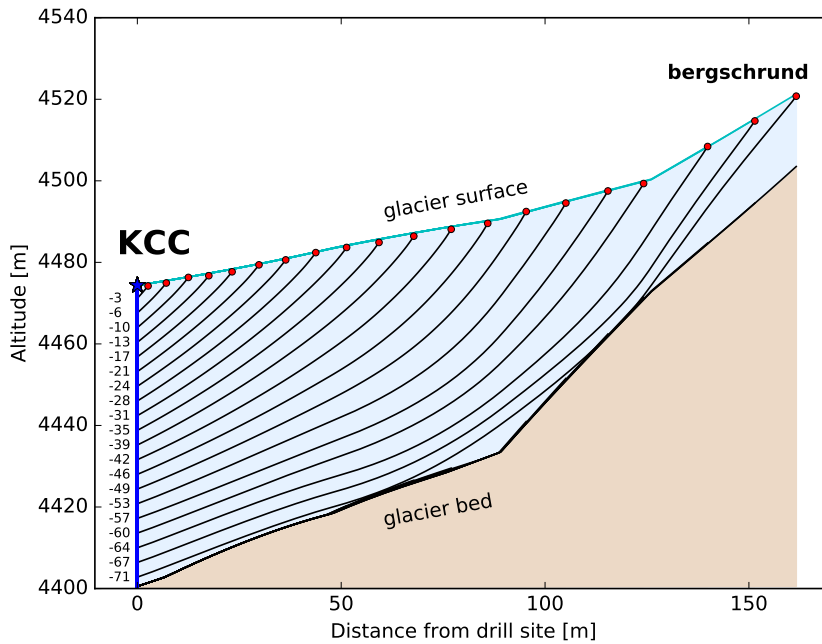


Figure 7.16: Backward trajectories starting from the KCC drilling site calculated with the Runge-Kutta method implemented in ParaView. The starting depths are indicated left of the borehole site (in meters). Red dots represent the source regions on the glacier surface. The represented surface and bedrock elevations corresponds to the surface and bedrock DEM used to run the full Stokes model. Due to not known small-scale bedrock corrugations, basal trajectories are less reliable than in the areas above.

According to the model calculations, the boreholes do not lie exactly on the same flow-line. The calculated catchment areas of the ice cores KCC, KCI, KCH, CC and KCS are presented together in Figure 7.18 (coordinates of the source points can be found in appendix A.5). According to the calculations, basal ice retrieved at all five cores stems from a common small area (around $80 \times 40 \text{ m}^2$) nearby the bergschrund. Compared to the results presented in this work, KCS backward trajectories calculated in Lüthi [2000] are slightly different, since in Lüthi [2000] the ice core CC lies exactly in the catchment area of KCS. This discrepancy is most likely due to different GPR profiles used to define the bedrock DEM in this area (see in section 5.1.4).

Forward trajectories calculated starting from all five ice cores mentioned above are represented in Figure 7.19. According to the calculations, the drilling site KCH is situated very close to the ice divide of the glacier. Looking at the forward stream lines starting from the KCH drilling site, but also at backward trajectories of the KCS and KCI drilling sites, it becomes evident that deep and shallow stream lines do not lie in the exactly same vertical plane when the flow direction changes. This is because shallow firn layers have a lower viscosity. Therefore, shallow firn layers are able to change the flow direction more rapidly than deep ice layers.

Error estimation

The uncertainty of the positions of the calculated source points, i.e. the error of the red dots in Figure 7.17 and 7.18, is estimated by sensitivity studies. To this aim, three different bedrock topographies are used. They were generated by lowering or lifting the bedrock elevation of sector 2 and 3 (i.e. close to the ice cliff and to the Grenzgletscher boundary, see Figure 5.1 of section 5.1.1) by 15 m, or by lowering the bedrock elevation of the glacier everywhere by 5 m. Combining the effects of the three modified topographies (considered as 3σ -errors) using quadratic uncertainty propagation and averaging over all source points of KCC, KCH and CC (KCI and KCS are too close to the modified

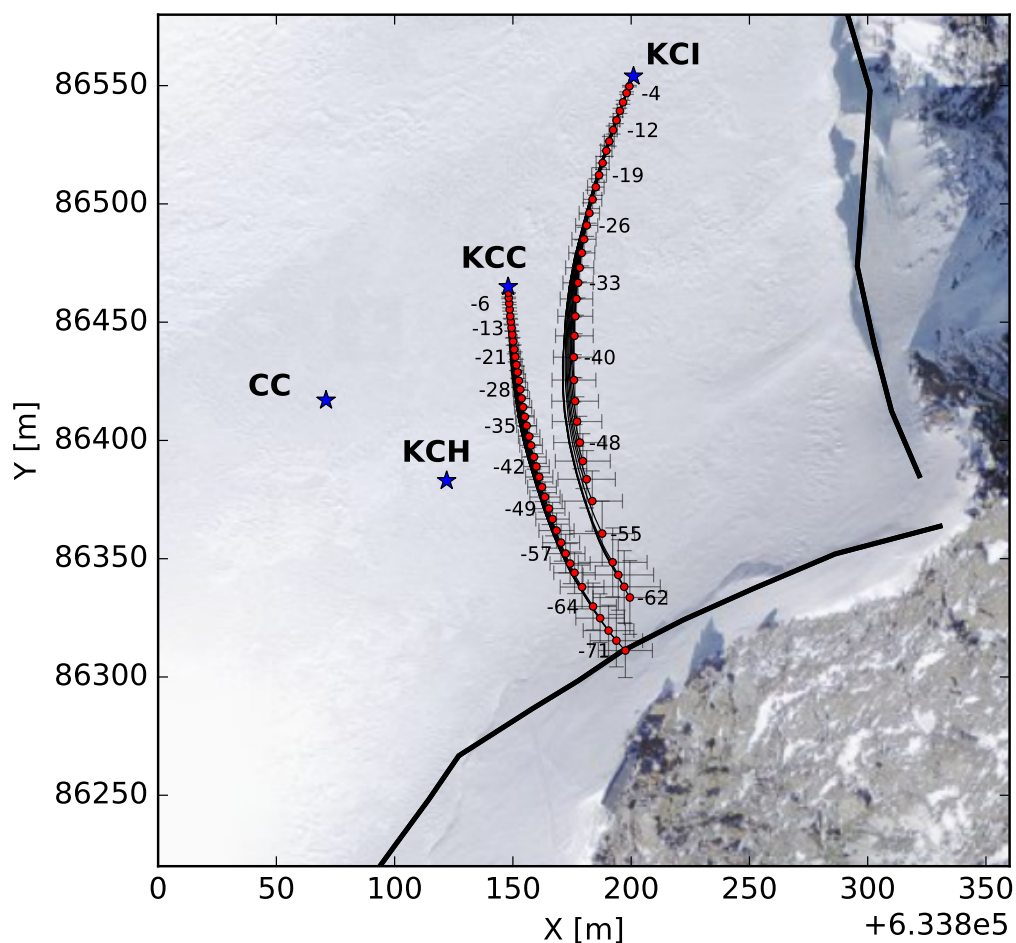


Figure 7.17: Aerial view of backward trajectories starting from KCC and KCI, calculated using the Runge-Kutta method within ParaView. The source points are indicated with red dots, with the corresponding ice-core depths given as labels beside the dots (in meters). The error of the source points is estimated to about 10% of the distance from the drill site. The catchment area of both ice cores is localized nearby the bergschrund. Due to not known small-scale bedrock corrugations, basal trajectories, i.e. trajectories starting (at the glacier surface) far from the drill site, are less reliable than shallow trajectories.

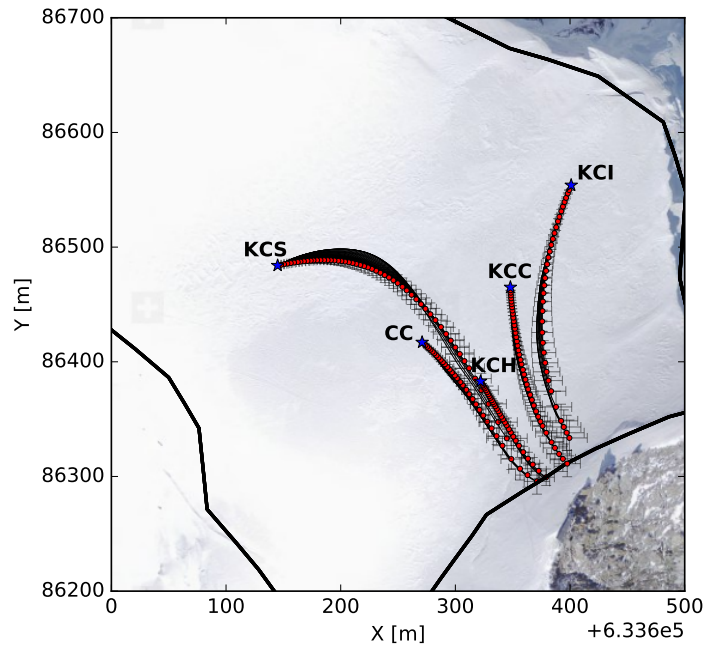


Figure 7.18: Aerial view of backward trajectories starting from KCC, KCI, KCH, CC and KCS, calculated using the Runge-Kutta method (ParaView).

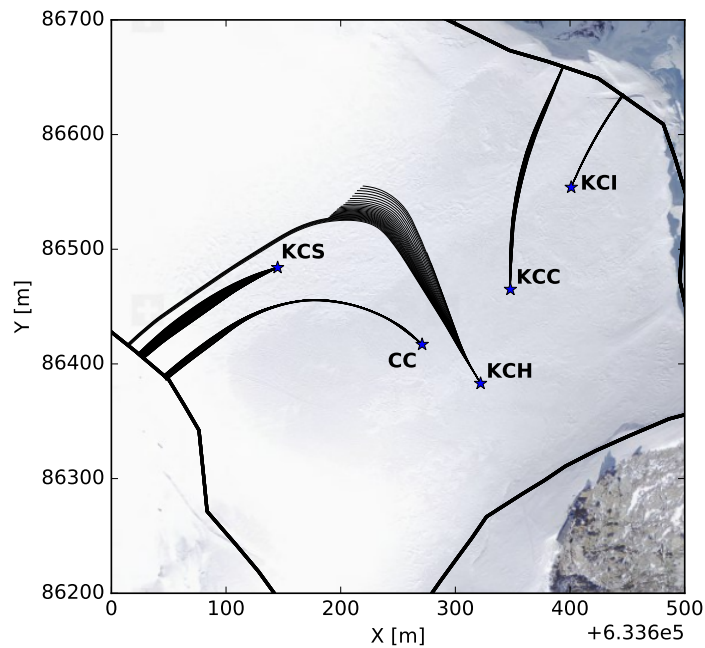


Figure 7.19: Aerial view of forward trajectories starting from KCC, KCI, KCH, CC and KCS, calculated using the Runge-Kutta method (ParaView). The drill site KCH is situated very close to the ice divide of the glacier.

sectors and showed highly unrealistic results), the position errors of the source points are estimated to $\sim 10\%$ of the distance from the borehole (1σ -error). This uncertainty could be reduced by constraining the glacier boundary geometry with more topography measurements.

Basal trajectories

Methods and data used in this work do not allow a proper error estimation for the position of the source points of basal ice. Backward trajectories of the lowermost ice layers could be influenced by the presence of small-scale bedrock corrugations, which can potentially trap ice or produce folds. A more reliable reconstruction of basal trajectories would require a much more precise knowledge of the bedrock topography, as well as a much finer mesh size. We refer to basal trajectories when the trajectories are within the lowermost 2–3 m ice above bedrock, where 2–3 m is an estimation of the size of possible bedrock corrugations based on the spatial resolution of the GPR measurements. Moreover, calculations of basal backward trajectories produce in some cases non-physical results, like backward trajectories terminating in the bedrock (too low vertical flow velocities of the basal ice compared to the increase of bedrock elevation moving uphill).

7.6 Dating of the ice cores

Using the velocity field calculated with the full Stokes model, the age field \mathcal{A} of the glacier is determined in a post-processing step using two alternative methods:

- Inspecting the integration time of the backward trajectories calculated in section 7.5 using the Runge-Kutta method implemented in ParaView.
- Employing the dating equation (3.10) (see section 3.4.4) implemented in Elmer (AdvectionReaction-Solver, see section 6.3).

Figure 7.20 presents dating results of the ice cores KCC and KCI (corresponding data using the Runge-Kutta method can be found in appendix A.5). Whereas the dating equation can be evaluated only at the mesh nodes (in this work 16 points per ice core, corresponding to the 16 extrusion levels, see section 6.2), using the Runge-Kutta method the age $\mathcal{A}(z)$ can be calculated quasi-continuously, since backward trajectories can start at any point. The Runge-Kutta method and the dating equation produce identical results down to the deepest 20% of the core above bedrock. According to the calculations using the Runge-Kutta method, the age of the ice core KCC reaches ~ 3000 years at about 70 m depth, ca. 3 m above bedrock, whereas the calculated age of the ice core KCI ca. 3 m above bedrock is ~ 2000 years. The error of the calculated ages is $\sim 20\%$. This error is estimated with the same procedure as outlined in section 7.5 for the error estimation of the source points, i.e. looking at the integration time of backward trajectories, calculated using three different bedrock topographies.

Further in Figure 7.20, the calculated chronologies of KCC and KCI are compared

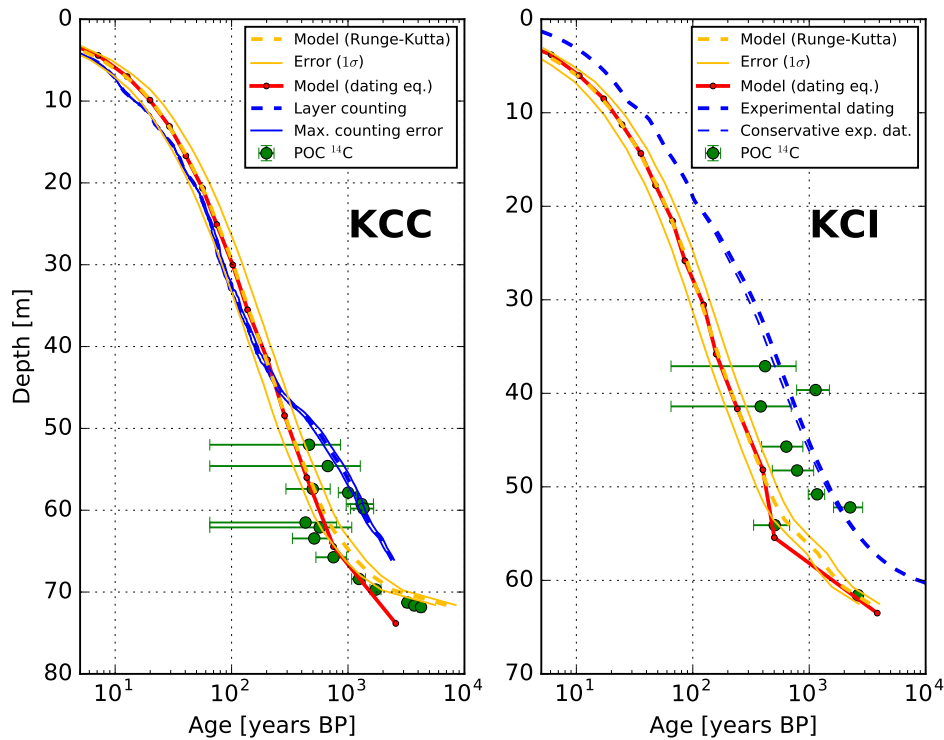


Figure 7.20: Chronologies of the ice cores KCC and KCI calculated with the full Stokes model, deploying the Runge-Kutta method (ParaView, yellow line) and the dating equation (Elmer, red line). The estimated dating error of the model is 20%. The model calculations are compared with radiocarbon dating results (green dots) [Hoffmann, 2016; Hoffmann et al., 2017; pers. comm. H. Hoffmann, 2017] and other experimental methods (blue lines) [Bohleber, 2008; Bohleber et al., 2017; pers. comm. P. Bohleber, 2017].

with two alternative experimental dating methods: annual layer counting (blue lines) [Bohleber, 2008; Bohleber et al., 2017; pers. comm. P. Bohleber, 2017] and Particulate Organic Carbon (POC) radiocarbon (^{14}C) dating (green dots) [Hoffmann, 2016; Hoffmann et al., 2017; pers. comm. H. Hoffmann, 2017]. At KCC, dating results using the full Stokes model are consistent with annual layer counting down to ca. 45 m absolute depth (within the estimated 1σ -error). Further down, layer counting and (two) radiocarbon measurements provide significantly higher ice ages compared to the model calculations. Between 60 m and 70 m depth, ice ages predicted by the model agree within the estimated errors (1σ) with the absolute ages determined by the radiocarbon method. The shift towards younger ages at about 60 m depth pointed out by the radiocarbon measurements represents an unsolved enigma and is discussed later in this section.

The ages calculated at KCI are significantly younger than ages determined using experimental methods [Bohleber, 2008]. The discrepancy is very large at all depths (ca. 200 years at 30 m depth, ca. 1000 years at 50 m depth). However, in the basal part of the

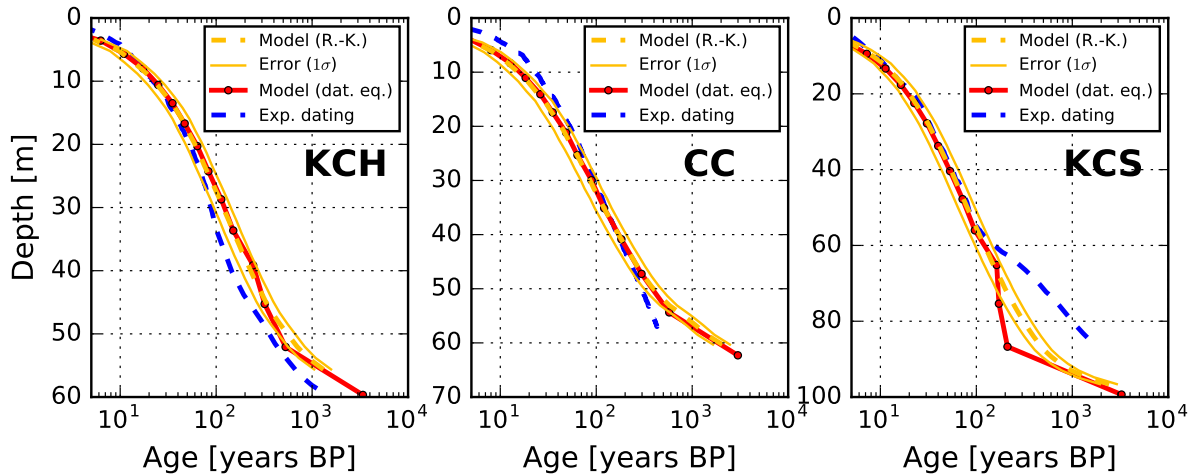


Figure 7.21: Calculated chronologies of the ice cores KCH, CC and KCS using the Runge-Kutta method and the dating equation, compared with experimental dating results (see section 2.2) [IUP glaciology group database]. The estimated dating error of the model is 20%.

core (below 54 m) the calculated ages are in good agreement with radiocarbon dating results (two points). Possible reasons responsible for the mismatch in dating the KCI core are discussed later in this section.

Dating results of the older cores KCH, CC and KCS using the full Stokes model are presented in Figure 7.21 (corresponding data using the Runge-Kutta method can be found in appendix A.5) and compared with dating results derived from experimental methods [Schäfer, 1995; Armbruster, 2000; Keck, 2001; IUP glaciology group database] (see section 2.2). According to the model calculations, near-to-basal ages of these three cores are around 2000 years. At KCH, the simulations predict ages, which tend to be older than ages determined using experimental methods, especially looking at the lower half of the core (ca. 200 years discrepancy at 50 m depth). The chronology of the core CC is well reproduced by the model calculations except near the surface, where the modeled ages tend to be too young. At KCS, the calculated age distribution is consistent with experimental dating results up to 60 m depth (within the estimated 1σ -error of the model), whereas big disagreement is evident further below (ca. 700 years discrepancy at 80 m depth, using the Runge-Kutta method). The kink towards older ages visible in the experimental chronology of KCS below 60 m is discussed below.

Discussion of the calculated age field

The dating results presented in this section lead to the following general considerations:

- The inspection of Figure 7.20 and 7.21 reveals that the Runge-Kutta method and the dating equation may produce discordant results in the vicinity of the bedrock. We consider results obtained using the Runge-Kutta method as more reliable, since at bedrock the dating equation may provide unrealistic ice ages, if the ice velocity is set to zero as boundary condition (the glacier is frozen to

bedrock). Moreover, the Runge-Kutta method has the advantage to produce quasi-continuous dating profiles. Therefore, later in this discussion only results using the Runge-Kutta method are considered and evaluated.

- All ice cores have the same catchment area of about $80 \times 40 \text{ m}^2$ in the vicinity of the bergschrund. According to the results presented in section 7.1.1, the model underestimates flow velocities in this area. As a consequence, the basal ages calculated with the model are possibly overestimated. This observation agrees with the dating results of the basal ice of KCC, where the modeled ages tend to be older compared to the radiocarbon dating results.
- According to the results presented in section 7.2, the model overestimates surface accumulation in the central region of the glacier. This trend is consistent with the generally too young ages calculated at all ice cores (excluding KCC) in the vicinity of the glacier surface (especially at CC).
- Due to the potential presence of not known small-scale bedrock corrugations (not represented in the bedrock DEM used for the simulations) the uncertainty of the ages calculated for the very basal layers may be higher than the previously estimated $\sim 20\%$. This concerns the last 2–3 m ice above bedrock, which corresponds to an estimation of the bedrock corrugation scale (see also section 7.5).

The chronology of the core KCC shows an age discontinuity towards younger ages at ca. 60 m depth. The discontinuity is pointed out by radiocarbon measurements, which offer absolute age constraints. Similar features are not excluded at other drill sites, where no exhaustive radiocarbon measurements are available. A comprehensive explanation of this finding is still not available. However, it is possible that it was generated by a perturbation due to folding ice, which can happen within the ice body [Dahl-Jensen et al., 2013]. Further considerations on this enigmatic observation are:

- According to the current glacier geometry and to the trajectory calculation presented in section 7.5, the discontinuity is not directly related to the bergschrund, since the backward trajectory calculated starting from the KCC site at 60 m depth intercepts the glacier surface ca. 40 m downstream of the bergschrund (see Figure 7.16).
- The numerical model presented here is not adequate to reproduce the observed discontinuity. The mesh used to approximate the glacier geometry (see section 6.2) is too coarse, with the horizontal mesh size of 50 m and a vertical distance between the nodes of ca. 9 m in the basal part of KCC. A much more accurate knowledge of small-scale bedrock corrugations would be required to resolve the observed finding. Moreover, the model is based on the steady state assumption and it cannot be excluded that the observed discontinuity is the result of a transient process.

- Figure 7.20 indicates that the modeled KCC chronology and the radiocarbon dating results are in agreement between a depth of 60 and 70 m, thus suggesting that the basal 10 m ice layers are not influenced by the perturbation.
- Figure 7.5 (section 7.1.2) shows a comparison between modeled vertical velocities and annual layer thickness profiles observed at KCC. The low agreement between the two curves in the lower part of the core is a consequence of the observed age discontinuity.

Dating results of older ice cores, i.e. KCI, KCH, CC and KCS, are in good agreement with ice-core chronologies based on experimental methods, with exception of the ice core KCI. In particular:

- The chronology of the ice core KCI calculated with the full Stokes model is significantly younger compared to experimental dating results. This is consistent with other results shown in this work, namely (a) too high accumulation rates predicted by the model in the KCI area, when compared with the accumulation rate measured at the ice core KCI (see Table 7.1 in section 7.2), and (b) slightly larger borehole inclination angles predicted by the model at KCI close to the surface, when compared with borehole inclination measurements (see Figure 7.11 in section 7.1.4). As already pointed out in previous sections, this suggests that the calculated ice outflow across the ice cliff boundary is likely too high. This is related to the not well known glacier geometry of this area.
- Compared to experimental dating results, the KCH chronology calculated with the model tends to be too old in the lower half of the core. This finding is consistent with previous discussions in this section and with results shown in previous sections, since KCH is the ice core located closest to the bergschrund. In the bergschrund area the model underestimates the velocity field (see section 7.1.1 and 7.2) and underestimated flow velocities imply overestimated ice ages.
- For the core KCS, the chronology based on experimental methods shows a sharp bending towards older ages starting at a depth of 60 m. Previous works based on layer counting associated this finding with upstream effects (lower accumulation rates in the steep slope below Signalkuppe, therefore thinner annual layers) [Armbruster, 2000]. The discrepancy between modeled and experimental chronology observed at KCS below 60 m is similar to the mismatch between modeled and layer counting chronology observed at KCC below 45 m. Additional radiocarbon measurements would be required in order to assess if the basal part of the KCS core is characterized by the presence of perturbations (with possible age discontinuities) as at KCC.

The chronologies of the cores KCH, CC and KCS calculated within this work can be compared with the chronologies calculated for the same cores in Lüthi and Funk [2000] (see Figure 2.4 in section 2.3). The results of the two full Stokes models are consistent, whereas the basal ages calculated in the present work tend to be higher than in Lüthi

and Funk [2000]. This difference could be an effect of the calculated flow field in the vicinity of the bergschrund, which in the present work is characterized by lower velocities compared to Lüthi and Funk [2000]. Finally, the agreement between modeled ice-core chronologies and radiocarbon dating results in the near-to-basal part of the KCC and KCI cores represents an important validation of the full Stokes model.

7.7 Depths of equal age

The calculation of depths of equal age is required to support the comparison between different ice-core records within the CG multi-core array. Ice-core depths of ages ranging between 20 and 1000 years BP are plotted in Figure 7.22. The calculated depths (of specific ice ages) are plotted versus the depth of KCC, which is chosen as reference as it provides the dating with the greatest confidence. The calculations are based on the modeled ice-core chronologies $\mathcal{A}(z)$ presented in section 7.6 (Runge-Kutta method). The depth uncertainties Δz are estimated from the error of the corresponding ice ages $\Delta \mathcal{A}$ using Gaussian error propagation ($\Delta z = \frac{\partial z}{\partial \mathcal{A}} \Delta \mathcal{A}$), where the error of the modeled age of ice is $\sim 20\%$ (see section 7.6). The uncertainties are small at shallow depths, where the dating error is small, and increase moving further down. Closer to the basal

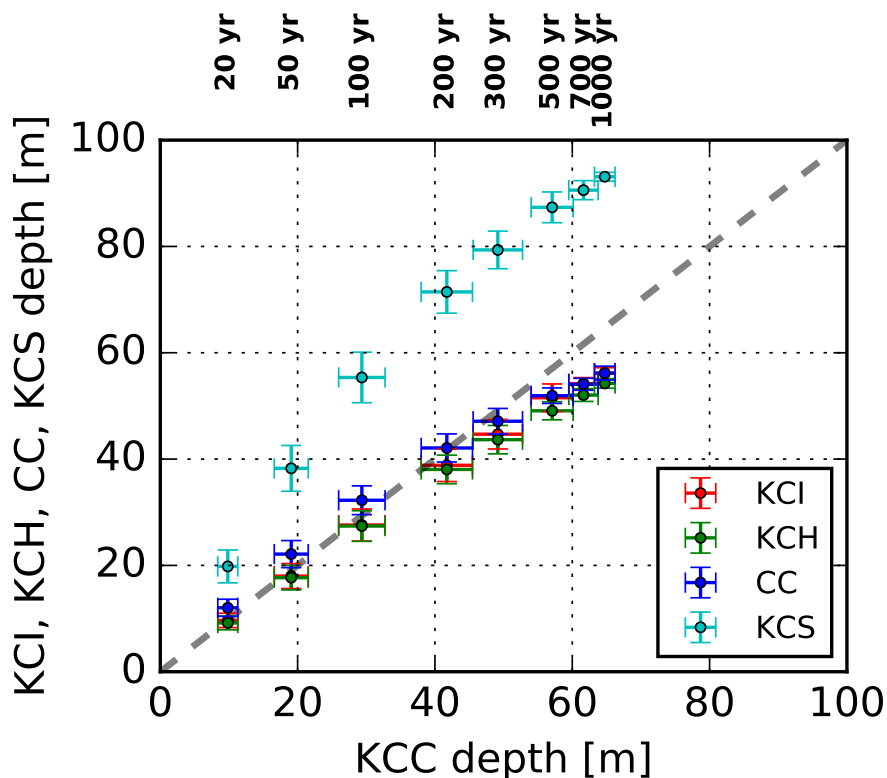


Figure 7.22: Depths of equal age calculated for all five IUP drilling sites and plotted versus the KCC depth (chosen as reference). The respective ages (in years BP) are indicated at the top of the plot.

layers the uncertainties decrease again, since $\frac{\partial z}{\partial A}$ is smaller.

According to the calculations, the drill sites KCC, KCI, KCH and CC have approximately the same ages at the same depths. This is expected since at those locations glacier thickness and (modeled) surface accumulation are comparable. Different is the case at the KCS site, where the glacier thickness is larger and the surface accumulation higher. Consequently, depths of equal age are located further below with respect to KCC.

In Figure 7.23, depths of equal age calculated with the model (in the range 20 to 1000 years BP) are compared with depths of equal age derived from Internal Reflection Horizons (IRHs) (data from Konrad [2011], Bohleber [2011] and Konrad et al. [2013]). The IRHs were detected in the glacier body by means of GPR measurements [Eisen

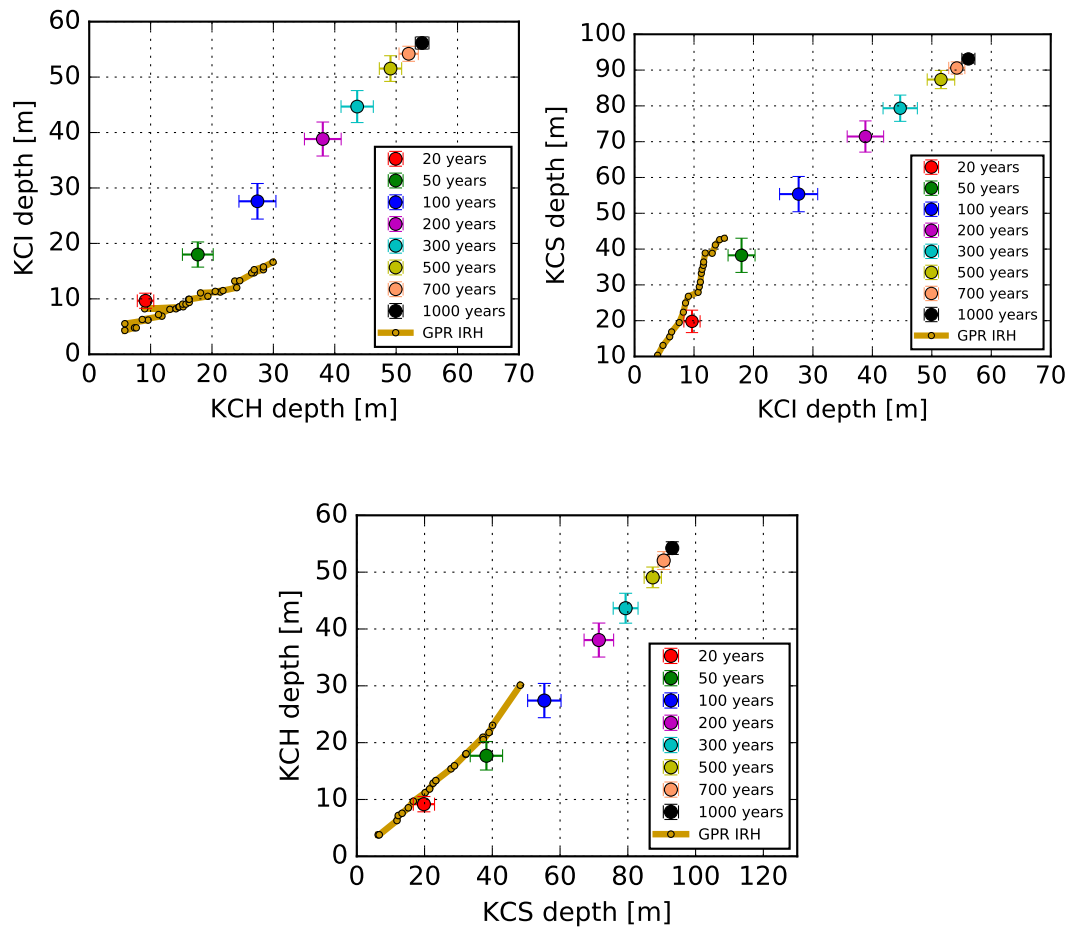


Figure 7.23: Depths of equal age calculated for the core pairs KCH-KCI, KCI-KCS and KCS-KCH for ice ages between 20 and 1000 years BP, and compared with depths of equal age derived from IRHs (GPR measurements). The IRH data are taken from Konrad [2011], Bohleber [2011] and Konrad et al. [2013].

et al., 2003; Konrad, 2011; Bohleber, 2011; Konrad et al., 2013]. IRHs are produced by variations in the firn or ice properties (like e.g. density, acidity [Robin et al., 1969] or crystal orientation fabric [Eisen et al., 2007]). They are associated with englacial isochronous layers. At CG, IHRs could be only traced in the firn part of the glacier, which hampers the validation of the calculated depths of equal age in the deep part of the glacier.

The IRHs extracted from the available GPR-profiles link the stratigraphy of the drill sites KCI, KCH and KCS. The IRHs linking the stratigraphy of the KCH and KCI drill sites (see upper left plot in Figure 7.23) suggest that KCI ice is older than KCH ice at same depths. This observation is in contrast to the model prediction, since the model reveals similar age–depth relationships for KCI and KCH. However, this mismatch is in accordance with the dating results shown in section 7.6. This because in comparison to experimental methods, the model underestimates the age of the KCI core and tends to overestimate the age of the KCH core (see Figure 7.20 and 7.21 in section 7.6). Considering the pairs KCI-KCS and KCS-KCH, the comparison of the calculated depths of equal age with the IRHs shows consistency (within the 1σ -error of the model) for the uppermost firn layers (see upper right and lower plot in Figure 7.23). However, discrepancies are evident further below and they confirm that the model underestimates the age of ice at the KCI site and overestimates the age of ice at the KCH site.

8 Summary and outlook

The main goal of the present thesis is to establish a full Stokes ice-flow model, fully thermo-mechanically coupled, of the high-Alpine glacier saddle Colle Gnifetti (CG). The main model application is to calculate ice particle trajectories within the ice body. The trajectories, calculated backwards from five CG ice-core drilling sites, are required to evaluate potential upstream effects, which may lead to an incorrect interpretation of the ice-core records in terms of atmospheric changes. As a further application, the model is expected to provide a reliable three-dimensional age field of the glacier, in order to support and supplement ice-core chronologies obtained with experimental methods.

The full Stokes model takes into account the rheology of compressible firn, which is mandatory for the application at CG since about half of the glacier depth is made out of firn. The heat flow is calculated using the enthalpy method, considering atmospheric temperature variations over the last century, energy contribution due to refreezing melt-water and deformational (strain) heat. The glacier geometry used is based on Ground Penetrating Radar (GPR) measurements for the bedrock topography and geodetic surveys for the surface topography, respectively. At locations with low data coverage, in particular at boundary areas close to the ice cliff and to the Grenzgletscher outflow, a manually adapted extrapolation of existing data was the only possibility to obtain a realistic glacier topography. The manual adjustments are performed in view of reducing the mismatch between modeled and measured surface velocities and accumulation. All simulations are performed using the Finite Element software Elmer/Ice.

The validity of the full Stokes model is investigated by comparing the model results with field measurements performed at CG in the past as well as during this work. The most relevant outcomes of the model validation are:

- Measured surface flow velocities (stake measurements) are reconstructed by the model with a mean deviation of $\sim 20\%$ (magnitude). Discrepancies in the flow directions are on average only 10° .
- Borehole inclination angles calculated at KCI are overestimated near the surface, whereas they are consistent with the measurements (within the 1σ -error) further below in the core (excluding the lowermost 10 m above bedrock).
- The model tends to overestimate the surface snow accumulation in the central region of the glacier. Comparing the model results with accumulation rates obtained from ice-core measurements, the overestimation ranges between 10% at KCC and 90% at KCI .

- The calculated ice-core density profiles are in accordance with the measured profiles to within a deviation of 10%.
- The calculated englacial temperature profiles are in accordance with the measured englacial temperature profiles to within 0.1 °C (considering only depths below 20 m, where seasonal fluctuations vanish). Moreover, the model is able to reproduce the transient warming trend of englacial temperatures observed at CG.

The results of the model validation suggest that the model reproduces well the flow behaviour of CG in the central part of the north-exposed flank, the area enclosing all IUP drill sites. However, the model predicts too large flow velocities in the area between KCI and the ice cliff. This mismatch is related to the imprecise geometrical definition of the ice cliff boundary.

The full Stokes model is employed to calculate ice-core backward trajectories. The calculations are performed in a post-processing step using the Runge-Kutta integrator implemented in ParaView. The calculations show that the source regions of all IUP ice cores are located in a small area of ca. $80 \times 40 \text{ m}^2$ just downstream of the bergschrund. The estimated 1σ -error of the position of the source points of individual core segments is $\sim 10\%$ of the distance from the corresponding drill site. This uncertainty is estimated running simulations with three different bedrock topographies. The uncertainty could be reduced constraining the geometry of the ice cliff and Grenzgletscher boundary with more topography measurements. The uncertainty of the position of source points of basal ice (ca. 2–3 m above bedrock) could be larger than 10%, since possible small-scale bedrock corrugations are not known and not represented in the bedrock DEM used for the simulations. According to the calculations, the near-to-basal ice of the KCC core was originally deposited less than 150 m upstream of the drill site. This corresponds to a positioning error of less than 15 m. The uncertainties of the calculated positions are therefore low enough for a meaningful evaluation of the upstream effects, when analyzing ice-core proxies for temperatures and other quantities.

The model is further used to calculate the age field of the glacier. The error of the calculated ages is $\sim 20\%$. The error is estimated by sensitivity studies, in the same way as done for the error estimation of the source points. However, in the basal part of the glacier (ca. 2–3 m above bedrock), the uncertainty of the calculated age–depth relationship can be larger due to the presence of small-scale bedrock corrugations, which are not known and not included in the bedrock DEM. Ice-core dating results are well in agreement with ice-core chronologies derived from experimental methods. In particular, the calculated chronology for the ice core KCC is consistent (within the 1σ -error of the model) with the annual layer chronology [Bohleber et al., 2017] for depths up to 45 m (the full core length of KCC is 72 m). Moreover, between 60 and 70 m depth the calculated chronology is consistent with radiocarbon dating results [Hoffmann, 2016] [Hoffmann et al., 2017]. A good agreement with radiocarbon dating results is also obtained for the near-to-basal ages calculated at the KCI drilling site. Such a good agreement of the model calculations with the radiocarbon dating results in the basal

part of the core represents an important and reliable validation of the full Stokes model.

For future activities, the accuracy of the full Stokes model could be further improved. Next important developments in the modeling tool would be:

- To account for the effect of bubble close-off on the firn/ice rheology. A preliminary implementation of bubble close-off in the Elmer/Ice firn flow law has been started in the frame of this thesis and validated on a simple test case. However, transient calculations applied at the CG glacier coupling the modified flow law with the continuity equation produced unstable results.
- To account for anisotropic ice rheology in the deeper part of the glacier, without neglecting firn compressibility at shallow depths. In this work, test runs are conducted using the anisotropic flow law GOLF instead of the firn flow law. The outcome is that neglecting firn compressibility at the surface produces highly unrealistic surface flow velocities. Therefore, a method should be developed which accounts for both, firn and anisotropic rheology (a first attempt is presented in this work).
- To do additional topography measurements (bedrock and surface) at CG, especially to better constrain the geometry of the ice cliff and of the Grenzgletscher boundary, because both govern the ice outflow of the north-exposed flank of CG.
- To improve the estimation of the thermodynamic boundary conditions, which in this work is based on borehole temperature measurements available in the central part of the glacier. A better estimation of the boundary conditions would require either more englacial temperature measurements (also comprehending the south-exposed slope below Zumsteinspitze) or a more complex surface energy balance model.
- To reduce the mesh size of the model. The mesh size used in this work has a horizontal resolution of 50 m. The accuracy of the model results can be improved by reducing the mesh size at least in the vicinity of the drill sites.

The developed modeling tool is well suited to perform further glaciological simulations for CG. For example, the model can be applied to investigate the response of CG under future climate change, i.e. with increasing atmospheric temperature and altered surface accumulation. In particular, the model can be used to predict if and when CG is expected to become a temperate glacier and when the glacier will be not anymore frozen to bedrock (and basal sliding set in). Both questions are of particular relevance for future ice-core studies, since cold ice is necessary to preserve the stratified ice archive from percolating meltwater and basal sliding would corrupt the lowermost and oldest ice layers.

Moreover, the developed full Stokes model allows to investigate the behaviour of CG under past climatic conditions such as during the *Little Ice Age*, the *Medieval Climatic Anomaly* or the last *Ice Age*. Past climate change may have produced variation of the

CG glacier geometry, flow dynamics, temperature and density field. The effects of past climate change are potentially detectable in the current measured temperature, density and annual layer thickness. Therefore, these studies are important in view of improving the interpretation of the ice-core records and to test the validity of the steady state assumption, which is relevant (among others) for future simulation studies.

Bibliography

- Ahrens, J., Geveci, B., and Law, C. (2005). Paraview: An end-user tool for large data visualization. *The Visualization Handbook*, 717.
- Alean, J., Haeberli, W., and Schädler, B. (1983). Snow accumulation, firn a temperature and solar radiation in the area of the Colle Gnifetti core drilling site (Monte Rosa, Swiss Alps): distribution patterns and interrelationships. *Z. Gletscherkd. Glazialgeol.*, 19(2):131–147.
- Armbruster, M. (2000). *Stratigraphische Datierung hoch-alpiner Eisbohrkerne über die letzten 1000 Jahre*. Diploma thesis [in German], Universität Heidelberg.
- Arnold, D. N., Brezzi, F., and Fortin, M. (1984). A stable finite element for the Stokes equations. *Calcolo*, 21(4):337–344.
- Aschwanden, A., Bueller, E., Khroulev, C., and Blatter, H. (2012). An enthalpy formulation for glaciers and ice sheets. *Journal of Glaciology*, 58(209):441–457.
- Auer, I., Böhm, R., Jurkovic, A., Lipa, W., Orlik, A., Potzmann, R., Schöner, W., Ungersböck, M., Matulla, C., Briffa, K., et al. (2007). Histalp—historical instrumental climatological surface time series of the greater alpine region. *International Journal of Climatology*, 27(1):17–46.
- Baiocchi, C., Brezzi, F., and Franca, L. P. (1993). Virtual bubbles and Galerkin-least-squares type methods (Ga. LS). *Computer Methods in Applied Mechanics and Engineering*, 105(1):125–141.
- Bauder, A., Fischer, M., Funk, M., Gabbi, J., Hoelzle, M., Huss, M., Kappenberger, G., and Steinegger, U. (2017). The swiss Glaciers 2013/14 and 2014/15. *The Swiss Glaciers. Glaciological Report*, 135.
- Benson, C. S. (1962). Stratigraphic studies in the snow and firn of the Greenland ice sheet. Technical report, COLD REGIONS RESEARCH AND ENGINEERING LAB HANOVER NH.
- Bohleber, P. (2008). Age distribution and $\delta^{18}\text{O}$ variability in a low accumulation Alpine ice core: perspective for paleoclimate studies. Diploma thesis, Universität Heidelberg.
- Bohleber, P. (2011). *Ground-penetrating radar assisted ice core research: The challenge of Alpine glaciers and dielectric ice properties*. Dissertation, Universität Heidelberg.

- Bohleber, P., Erhardt, T., Spaulding, N., Hoffmann, H., Fischer, H., and Mayewski, P. (2017). Temperature and mineral dust variability recorded in two low accumulation Alpine ice cores over the last millennium. *Clim. Past Discuss.*, <https://doi.org/10.5194/cp-2017-80>, accepted.
- Bohleber, P., Wagenbach, D., Schöner, W., and Böhm, R. (2013). To what extent do water isotope records from low accumulation alpine ice cores reproduce instrumental temperature series? *Tellus B*, 65.
- Böhm, R., Jones, P. D., Hiebl, J., Frank, D., Brunetti, M., and Maugeri, M. (2010). The early instrumental warm-bias: a solution for long central European temperature series 1760–2007. *Climatic Change*, 101(1):41–67.
- Braithwaite, R. J., Raper, S. C., and Candela, R. (2013). Recent changes (1991–2010) in glacier mass balance and air temperature in the European Alps. *Annals of Glaciology*, 54(63):139–146.
- Brezzi, F., Bristeau, M.-O., Franca, L. P., Mallet, M., and Rogé, G. (1992). A relationship between stabilized finite element methods and the Galerkin method with bubble functions. *Computer Methods in Applied Mechanics and Engineering*, 96(1):117–129.
- Brezzi, F., Marini, L. D., and Süli, E. (2004). Discontinuous Galerkin methods for first-order hyperbolic problems. *Mathematical models and methods in applied sciences*, 14(12):1893–1903.
- Brondex, J. (2017). *Influence de l'endommagement et du frottement basal sur la dynamique de la ligne d'échouage*. PhD thesis, Université de Grenoble.
- Calonne, N., Flin, F., Morin, S., Lesaffre, B., du Roscoat, S. R., and Geindreau, C. (2011). Numerical and experimental investigations of the effective thermal conductivity of snow. *Geophysical Research Letters*, 38(23).
- Castelnau, O., Duval, P., Lebensohn, R. A., and Canova, G. R. (1996). Viscoplastic modeling of texture development in polycrystalline ice with a self-consistent approach: Comparison with bound estimates. *Journal of Geophysical Research: Solid Earth*, 101(B6):13851–13868.
- Castelnau, O., Shoji, H., Mangeney, A., Milsch, H., Duval, P., Miyamoto, A., Kawada, K., and Watanabe, O. (1998). Anisotropic behavior of GRIP ices and flow in Central Greenland. *Earth and planetary science letters*, 154(1):307–322.
- Cuffey, K. M. and Paterson, W. S. B. (2010). *The physics of glaciers*. Academic Press.
- Dahl-Jensen, D., Albert, M., Aldahan, A., Azuma, N., Balslev-Clausen, D., Baumgartner, M., Berggren, A.-M., Bigler, M., Binder, T., Blunier, T., et al. (2013). Eemian interglacial reconstructed from a Greenland folded ice core. *Nature*, 493(7433):489–494.

- De Fleurian, B., Gagliardini, O., Zwinger, T., Durand, G., Le Meur, E., Mair, D., and Raback, P. (2014). A double continuum hydrological model for glacier applications. *The Cryosphere*, 8:137–153.
- Diez, A., Eisen, O., Hofstede, C., Bohleber, P., and Polom, U. (2013). Joint interpretation of explosive and vibroseismic surveys on cold firn for the investigation of ice properties. *Annals of Glaciology*, 54(64):201–210.
- Donea, J. (1984). Recent advances in computational methods for steady and transient transport problems. *Nuclear Engineering and Design*, 80(2):141–162.
- Duva, J. and Crow, P. (1994). Analysis of consolidation of reinforced materials by power-law creep. *Mechanics of materials*, 17(1):25–32.
- Eisen, O., Hamann, I., Kipfstuhl, S., Steinhage, D., and Wilhelms, F. (2007). Direct evidence for continuous radar reflector originating from changes in crystal-orientation fabric. *The Cryosphere*, 1(1):1–10.
- Eisen, O., Nixdorf, U., Keck, L., and Wagenbach, D. (2003). Alpine ice cores and ground penetrating radar: combined investigations for glaciological and climatic interpretations of a cold alpine ice body. *Tellus B*, 55(5):1007–1017.
- Elmer/Ice-Wiki (2017). <http://elmerice.elmerfem.org/wiki/doku.php?id=start>.
- Favier, L., Durand, G., Cornford, S. L., Gudmundsson, G. H., Gagliardini, O., Gillet-Chaulet, F., Zwinger, T., Payne, A., and Le Brocq, A. M. (2014). Retreat of Pine Island Glacier controlled by marine ice-sheet instability. *Nature Climate Change*, 4(2):117–121.
- Favier, L., Gagliardini, O., Durand, G., and Zwinger, T. (2012). A three-dimensional full stokes model of the grounding line dynamics: effect of a pinning point beneath the ice shelf. *The Cryosphere*, 6:101–112.
- Fischer, H., Severinghaus, J., Brook, E., Wolff, E., Albert, M., Alemany, O., Arthern, R., Bentley, C., Blankenship, D., Chappellaz, J., et al. (2013). Where to find 1.5 million yr old ice for the IPICS "Oldest-Ice" ice core. *Climate of the Past*, 9(6):2489–2505.
- Gabrieli, J., Cozzi, G., Vallelonga, P., Schwikowski, M., Sigl, M., Eickenberg, J., Wacker, L., Boutron, C., Gäggeler, H., Cescon, P., et al. (2011). Contamination of Alpine snow and ice at Colle Gnifetti, Swiss/Italian Alps, from nuclear weapons tests. *Atmospheric environment*, 45(3):587–593.
- Gabrielli, P., Barbante, C., Bertagna, G., Bertó, M., Binder, D., Carton, A., Carturan, L., Cazorzi, F., Cozzi, G., Dalla Fontana, G., et al. (2016). Age of the Mt. Ortles ice cores, the Tyrolean Iceman and glaciation of the highest summit of South Tyrol since the Northern Hemisphere Climatic Optimum. *The Cryosphere*, 10(6):2779.

- Gäggeler, H., Von Gunten, H., Rössler, E., Oeschger, H., and Schotterer, U. (1983). ^{210}Pb -Dating of cold alpine firn/ice cores from Colle Gnifetti, Switzerland. *Journal of Glaciology*, 29(101):165–177.
- Gagliardini, O., Gillet-Chaulet, F., Durand, G., Vincent, C., and Duval, P. (2011). Estimating the risk of glacier cavity collapse during artificial drainage: The case of Tête Rousse Glacier. *Geophysical Research Letters*, 38(10).
- Gagliardini, O. and Meyssonier, J. (1997). Flow simulation of a firn-covered cold glacier. *Ann. Glaciol.*, 24, 242–247.
- Gagliardini, O., Zwinger, T., Gillet-Chaulet, F., Durand, G., Favier, L., de Fleurian, B., Greve, R., Malinen, M., Martín, C., Råback, P., Ruokolainen, J., Sacchettini, M., Schäfer, M., Seddik, H., and Thies, J. (2013). Capabilities and performance of Elmer/Ice, a new-generation ice sheet model. *Geosci. Model Dev.*, 6, 1299–1318, doi:10.5194/gmd-6-1299-2013.
- Gilbert, A., Gagliardini, O., Vincent, C., and Wagnon, P. (2014a). A 3-D thermal regime model suitable for cold accumulation zones of polythermal mountain glaciers. *J. Geophys. Res. Earth Surf*, 119, doi:10.1002/2014JF003199.
- Gilbert, A., Vincent, C., Gagliardini, O., Krug, J., and Berthier, E. (2015). Assessment of thermal change in cold avalanching glaciers in relation to climate warming. *Geophysical Research Letters*, 42(15):6382–6390.
- Gilbert, A., Vincent, C., Six, D., Wagnon, P., Piard, L., and Ginot, P. (2014b). Modeling near-surface firn temperature in a cold accumulation zone (Col du Dôme, French Alps): from a physical to a semi-parameterized approach. *The Cryosphere*, 8(2):689.
- Gillet-Chaulet, F., Gagliardini, O., Meyssonier, J., Montagnat, M., and Castelnau, O. (2005). A user-friendly anisotropic flow law for ice-sheet modelling. *Journal of Glaciology*, 51(172):3–14.
- Gillet-Chaulet, F., Gagliardini, O., Meyssonier, J., Zwinger, T., and Ruokolainen, J. (2006). Flow-induced anisotropy in polar ice and related ice-sheet flow modelling. *Journal of non-newtonian fluid mechanics*, 134(1):33–43.
- Gillet-Chaulet, F., Gagliardini, O., Seddik, H., Nodet, M., Durand, G., Ritz, C., Zwinger, T., Greve, R., and Vaughan, D. G. (2012). Greenland ice sheet contribution to sea-level rise from a new-generation ice-sheet model. *The Cryosphere*, 6(6):1561–1576.
- Glen, J. W. (1955). The creep of polycrystalline ice. In *Proceedings of the Royal Society of London A: Mathematical, Physical and Engineering Sciences*, volume 228, pages 519–538. The Royal Society.
- Greve, R. and Blatter, H. (2009). *Dynamics of ice sheets and glaciers*. Springer Science & Business Media.

- Gudmundsson, G. H. (1994). *Converging glacier flow - a case study: the Unteraar-glacier*. Eidg. Tech. Hochschule, Zürich. Versuchsanst. Wasserbau, Hydrol. Glaziol. Mitt. 131.
- Gudmundsson, G. H., Bauder, A., Lüthi, M., Fischer, U. H., and Funk, M. (1999). Estimating rates of basal motion and internal ice deformation from continuous tilt measurements. *Annals of Glaciology*, 28(1):247–252.
- Haerberli, W. and Funk, M. (1991). Borehole temperatures at the Colle Gnifetti core-drilling site (Monte Rosa, Swiss Alps). *Journal of Glaciology*, 37(125):37–46.
- Haerberli, W., Schmid, W., and Wagenbach, D. (1988). On the geometry, flow and age of firn and ice at the Colle Gnifetti, core drilling site (Monte Rosa, Swiss Alps). *Zeitschrift für Gletscherkunde und Glazialgeologie*, 24(1):1–19.
- Hock, R. (1999). A distributed temperature-index ice-and snowmelt model including potential direct solar radiation. *Journal of Glaciology*, 45(149):101–111.
- Hoelzle, M., Darms, G., Lüthi, M., and Suter, S. (2011). Evidence of accelerated englacial warming in the Monte Rosa area, Switzerland/Italy. *Cryosphere*, 5(1), 231–243 (doi: 10.5194/tc-5-231-2011).
- Hoffmann, H., Preunkert, S., Legrand, M., Leinfelder, D., Bohleber, P., Friedrich, R., and Wagenbach, D. (2017). A New Sample Preparation System for Micro-14C Dating of Glacier Ice with a First Application to a High Alpine Ice Core from Colle Gnifetti (Switzerland). *Radiocarbon*, page 1–17.
- Hoffmann, H. M. (2016). *Micro radiocarbon dating of the particulate organic carbon fraction in Alpine glacier ice: method refinement, critical evaluation and dating applications*. Phd thesis, Universität Heidelberg.
- Hughes, T. J. (1987). Recent progress in the development and understanding of SUPG methods with special reference to the compressible Euler and Navier-Stokes equations. *International journal for numerical methods in fluids*, 7(11):1261–1275.
- IPCC (2014). *Climate change 2014: Synthesis Report. Contribution of Working Groups I, II and III to the Fifth Assessment Report of the Intergovernmental Panel on Climate Change [Core Writing Team, R.K. Pachauri and L.A. Meyer (eds.)]*. IPCC, Geneva, Switzerland, 151 pp.
- Jenk, T. M., Szidat, S., Bolius, D., Sigl, M., Gaeggeler, H. W., Wacker, L., Ruff, M., Barbante, C., Boutron, C. F., and Schwikowski, M. (2009). A novel radiocarbon dating technique applied to an ice core from the Alps indicating late Pleistocene ages. *Journal of Geophysical Research: Atmospheres*, 114(D14).
- Johnsen, S. J., Dahl-Jensen, D., Gundestrup, N., Steffensen, J. P., Clausen, H. B., Miller, H., Masson-Delmotte, V., Sveinbjörnsdóttir, A. E., and White, J. (2001).

- Oxygen isotope and palaeotemperature records from six Greenland ice-core stations: Camp Century, Dye-3, GRIP, GISP2, Renland and NorthGRIP. *Journal of Quaternary Science*, 16(4):299–307.
- Keck, L. (2001). *Climate significance of stable isotope records from Alpine ice cores*. Dissertation, IUP Heidelberg.
- Kerch, J. (2016). *Crystal-orientation fabric variations on the cm-scale in cold Alpine ice: Interaction with paleo-climate proxies under deformation and implications for the interpretation of seismic velocities*. Phd thesis, Universität Heidelberg.
- Kipfstuhl, S., Pauer, F., Kuhs, W. F., and Shoji, H. (2001). Air bubbles and clathrate hydrates in the transition zone of the NGRIP deep ice core. *Geophysical Research Letters*, 28(4):591–594.
- Konrad, H. (2011). *Characterization of the age distribution and the flow field of an Alpine glacier by a combination of simple flow modeling and ground-penetrating radar*. Diploma thesis, Universität Heidelberg.
- Konrad, H., Bohleber, P., Wagenbach, D., Vincent, C., and Eisen, O. (2013). Determining the age distribution of Colle Gnifetti, Monte Rosa, Swiss Alps, by combining ice cores, ground-penetrating radar and a simple flow model. *Journal of Glaciology*, 59(213).
- Krug, J., Weiss, J., Gagliardini, O., and Durand, G. (2014). Combining damage and fracture mechanics to model calving. *The Cryosphere*, 8(6):2101–2117.
- Kumar, L., Skidmore, A. K., and Knowles, E. (1997). Modelling topographic variation in solar radiation in a GIS environment. *International Journal of Geographical Information Science*, 11(5):475–497.
- Kuzmin, D. (2010). A guide to numerical methods for transport equations. *University Erlangen-Nuremberg*.
- Lambert, F., Delmonte, B., Petit, J.-R., Bigler, M., Kaufmann, P. R., Hutterli, M. A., Stocker, T. F., Ruth, U., Steffensen, J. P., and Maggi, V. (2008). Dust-climate couplings over the past 800,000 years from the EPICA Dome C ice core. *Nature*, 452(7187):616–619.
- Lüthi, D., Le Floch, M., Bereiter, B., Blunier, T., Barnola, J.-M., Siegenthaler, U., Raynaud, D., Jouzel, J., Fischer, H., Kawamura, K., et al. (2008). High-resolution carbon dioxide concentration record 650,000–800,000 years before present. *Nature*, 453(7193):379–382.
- Lüthi, M. and Funk, M. (2000). Dating of ice cores from a high Alpine glacier with a flow model for cold firn. *Ann. Glaciol.*, 31:69–79.

- Lüthi, M. and Funk, M. (2001). Modelling heat flow in a cold, high altitude glacier: interpretation of measurements from Colle Gnifetti, Swiss Alps. *J. Glaciol.*, 47:314–324.
- Lüthi, M. P. (2000). *Rheology of cold firn and dynamics of a polythermal ice stream (studies on Colle Gnifetti and Jakobshavns Isbrae)*. PhD thesis.
- Ma, Y., Gagliardini, O., Ritz, C., Gillet-Chaulet, F., Durand, G., and Montagnat, M. (2010). Enhancement factors for grounded ice and ice shelves inferred from an anisotropic ice-flow model. *Journal of Glaciology*, 56(199):805–812.
- Medici, F. and Rybach, L. (1995). Geothermal map of switzerland. *Swiss Geophysical Commission, Geophysique*, 30:30.
- Miller, S. L. (1969). Clathrate hydrates of air in antarctic ice. *Science*, 165(3892):489–490.
- Mosso, A. (1899). *Der Mensch auf den Hochalpen*. Veit, Leipzig.
- Müller, F. (1962). Zonation in the accumulation area of the glaciers of Axel Heiberg Island, NWT, Canada. *Journal of Glaciology*, 4(33):302–311.
- Nye, J. (1957). The distribution of stress and velocity in glaciers and ice-sheets. In *Proceedings of the Royal Society of London A: Mathematical, Physical and Engineering Sciences*, volume 239, pages 113–133. The Royal Society.
- Oeschger, H., Schotterer, U., Stauffer, B., Haeberli, W., and Röthlisberger, H. (1977). First results from Alpine core drilling projects. *Zeitschrift für Gletscherkunde und Glazialgeologie*, 13(1/2):193–208.
- Preunkert, S. (1994). *Glazio-chemische Verhältnisse des Colle Gnifetti im Vergleich zu seiner regionalen Umgebung*. Diploma thesis, Institut für Umweltp Physik der Universität Heidelberg.
- Preunkert, S., Wagenbach, D., Legrand, M., and Vincent, C. (2000). Col du Dôme (Mt Blanc Massif, French Alps) suitability for ice-core studies in relation with past atmospheric chemistry over Europe. *Tellus B: Chemical and Physical Meteorology*, 52(3):993–1012.
- Råback, P., Malinen, M., Ruokolainen, J., Pursula, A., Zwinger, T., and Eds. (2017). Elmer Models Manual. <http://www.nic.funet.fi/pub/sci/physics/elmer/doc/ElmerModelsManual.pdf>.
- Rapp, R. (1997). Use of potential coefficient models for geoid undulation determinations using a spherical harmonic representation of the height anomaly/geoid undulation difference. *Journal of Geodesy*, 71(5):282–289.
- Robin, G. d. Q., Evans, S., and Bailey, J. T. (1969). Interpretation of radio echo sounding in polar ice sheets. *Philosophical Transactions of the Royal Society of London A: Mathematical, Physical and Engineering Sciences*, 265(1166):437–505.

- Ruokolainen, J., Malinen, M., Råback, P., Zwinger, T., Pursula, A., and Byckling, M. (2017). ElmerSolver Manual. <http://www.nic.funet.fi/pub/sci/physics/elmer/doc/ElmerSolverManual.pdf>.
- Ryser, C. (2014). *Cold ice in an alpine glacier and ice dynamics at the margin of the Greenland Ice Sheet*. PhD thesis.
- Ryser, C., Lüthi, M., Andrews, L., Hoffman, M., Catania, G., Hawley, R., Neumann, T., and Kristensen, S. S. (2014). Sustained high basal motion of the Greenland Ice Sheet revealed by borehole deformation. 60(222):647–660.
- Salamatin, A. and Duval, P. (1997). Creep flow and pressure relaxation in bubbly medium. *International journal of solids and structures*, 34(1):61–78.
- Schäfer, J. (1995). *Rekonstruktion bio-geochemischer Spurenstoffkreisläufe anhand eines alpinen Eisbohrkerns*. Diploma thesis, Universität Heidelberg.
- Schaller, C. F., Freitag, J., and Eisen, O. (2017). Critical porosity of gas enclosure in polar firn independent of climate. *Climate of the Past*, 13(11):1685–1693.
- Schotterer, U., Häberli, W., Good, W., Oeschger, H., and Röthlisberger, H. (1978). Datierung von kaltem Firn und Eis in einem Bohrkern vom Colle Gnifetti, Monte Rosa. *Jahrbuch der Schweizerischen Naturforschenden Gesellschaft, wissenschaftlicher Teil*, pages 48–57.
- Schwerzmann, A., Funk, M., Blatter, H., Lüthi, M., Schwikowski, M., and Palmer, A. (2006). A method to reconstruct past accumulation rates in alpine firn regions: A study on Fiescherhorn, Swiss Alps. *Journal of Geophysical Research: Earth Surface*, 111(F1).
- Seddik, H., Greve, R., Zwinger, T., Gillet-Chaulet, F., and Gagliardini, O. (2012). Simulations of the Greenland ice sheet 100 years into the future with the full stokes model Elmer/Ice. *Journal of Glaciology*, 58(209):427–440.
- Shoji, H. and Langway, C. (1988). Flow-law parameters of the Dye 3, Greenland, deep ice core. *Annals of Glaciology*, 10:146–150.
- Shumskii, P. A. (1964). Principles of structural glaciology. *Dover Publications, Inc., New York*, 497.
- Suter, S. (2002). *Cold firn and ice in the Monte Rosa and Mont Blanc areas: spatial occurrence, surface energy balance and climatic evidence*. PhD thesis, ETH Zürich.
- Todd, J. and Christoffersen, P. (2014). Are seasonal calving dynamics forced by buttressing from ice mélange or undercutting by melting? Outcomes from full-Stokes simulations of Store Glacier, West Greenland. *The Cryosphere*, 8(6):2353–2365.

- Vincent, C., Fischer, A., Mayer, C., Bauder, A., Galos, S. P., Funk, M., Thibert, E., Six, D., Braun, L., and Huss, M. (2017). Common climatic signal from glaciers in the European Alps over the last 50 years. *Geophysical Research Letters*, 44(3):1376–1383.
- Vincent, C., Le Meur, E., Six, D., Funk, M., Hoelzle, M., and Preunkert, S. (2007a). Very high-elevation Mont Blanc glaciated areas not affected by the 20th century climate change. *Journal of Geophysical Research: Atmospheres*, 112(D9).
- Vincent, C., Le Meur, E., Six, D., Possenti, P., Lefebvre, E., and Funk, M. (2007b). Climate warming revealed by englacial temperatures at Col du Dôme (4250 m, Mont Blanc area). *Geophysical Research Letters*, 34(16).
- Wagenbach, D., Bohleber, P., and Preunkert, S. (2012). Cold, alpine ice bodies revisited: What may we learn from their impurity and isotope content? *Geografiska Annaler: Series A, Physical Geography*, 94(2):245–263.
- Wagenbach, D. and Geis, K. (1989). The mineral dust record in a high altitude Alpine glacier (Colle Gnifetti, Swiss Alps). In *Paleoclimatology and paleometeorology: modern and past patterns of global atmospheric transport*, pages 543–564. Springer.
- Wagner, S. (1996). *Dreidimensionale Modellierung zweier Gletscher und Deformationssanalyse von eisreichem Permafrost*. Dissertation, Versuchsanstalt für Wasserbau, Hydrologie und Glaziologie der ETH Zürich.
- Werder, M. A., Hewitt, I. J., Schoof, C. G., and Flowers, G. E. (2013). Modeling channelized and distributed subglacial drainage in two dimensions. *Journal of Geophysical Research: Earth Surface*, 118(4):2140–2158.
- Wolff, E., Barbante, C., Becagli, S., Bigler, M., Boutron, C., Castellano, E., De Angelis, M., Federer, U., Fischer, H., Fundel, F., et al. (2010). Changes in environment over the last 800,000 years from chemical analysis of the EPICA Dome C ice core. *Quaternary Science Reviews*, 29(1):285–295.
- Yen, Y.-C. (1981). Review of thermal properties of snow, ice and sea ice. Technical report, COLD REGIONS RESEARCH AND ENGINEERING LAB HANOVER NH.
- Zwinger, T., Greve, R., Gagliardini, O., Shiraiwa, T., and Lyly, M. (2007). A full stokes-flow thermo-mechanical model for firn and ice applied to the Gorshkov crater glacier, Kamchatka. *Annals of Glaciology*, 45(1):29–37.
- Zwinger, T., Schäfer, M., Martín, C., and Moore, J. C. (2014). Influence of anisotropy on velocity and age distribution at scharffenbergbotnen blue ice area. *The Cryosphere*, 8(2):607–621.

List of Figures

2.1	Areal imagery of the CG glacier saddle, Monte Rosa massif	5
2.2	Photographs of the CG glacier saddle	6
2.3	Accumulation rate and mean $\delta^{18}\text{O}$ level in the Monte Rosa area [Bohleber et al., 2013]	7
2.4	CG ice-core chronologies calculated in Lüthi and Funk [2000]	10
2.5	CG englacial temperatures calculated in Lüthi and Funk [2001]	11
3.1	Deformation of a polycrystalline ice sample (schematic representation) . .	15
3.2	Components of the Cauchy stress tensor	16
3.3	Pure and simple shear	17
3.4	Recommended values for the creep parameter A	20
3.5	Ice slab geometry	21
3.6	The parameters a and b in the firn flow law	23
4.1	Measured surface velocities 1980–99	30
4.2	Measured surface velocities 2014–16	31
4.3	Principle of surface velocity measurements using stakes as marker	32
4.4	Surface topography measurements performed in the period 2014–2016 . .	34
4.5	The inclinometer probe: centralizer and operation in the field	37
4.6	Measured inclination angles at KCC (2016)	38
4.7	Measured inclination angles at KCI (2016)	38
5.1	The study area	42
5.2	Surface DEM used as input in the numerical model	43
5.3	Exemplary radargram of a GPR profile at CG [Konrad et al., 2013] . . .	45
5.4	Bedrock DEM used as input in the numerical model	46
5.5	Map of glacier thickness at CG	46
5.6	The bergschrund and the big crevasse at the western boundary	47
5.7	Surface temperature map used for the model spin-up	50
5.8	Instrumental air temperature anomalies for CG (1900–2015)	51
5.9	Daily maximum air temperatures for 2015 estimated at CG and the parameter T^+	52
5.10	The parameter \tilde{T}^+ estimated in the years 1982–2016	52
5.11	The parameter \tilde{T}^+ estimated in the years 1901–2016	52
5.12	Basal heat flux map used as boundary condition	54
5.13	Execution of the spin-up of the full Stokes model	56
5.14	Procedure to calculate the transient solution of the full Stokes model. . .	57
6.1	Three-dimensional mesh used to approximate the geometry of CG	60
6.2	Two-dimensional mesh of the glacier footprint	61
6.3	Uniaxial stress-driven compression test: sketch	64
6.4	Uniaxial stress-driven compression test: numerical and analytical results	65
6.5	Test runs of the modified Porous-Solver applied at CG	67

6.6	Sketch of the attempt to combine firm and anisotropic flow law	68
6.7	Simulation results for combined firm and anisotropic flow law	69
7.1	Calculated horizontal surface flow velocities	72
7.2	Quantitative validation of the calculated surface flow velocities	73
7.3	Horizontal and vertical velocities calculated at the drilling sites KCC, KCI, KCH, CC and KCS using firm and anisotropic flow law	74
7.4	Components of the strain-rate tensor $\dot{\epsilon}$ calculated at KCC	75
7.5	Vertical velocity profiles calculated at KCC and compared with annual layer thickness	76
7.6	Diagonal components and eigenvalues of the tensor $\bar{\mathbf{A}}^{(2)}$ measured at KCC	78
7.7	Illustration of method 1 and 2 to calculate borehole inclination angles . .	80
7.8	Calculated borehole deformation at the drilling site KCC	82
7.9	Calculated borehole deformation at the drilling site KCI	82
7.10	Calculated inclination angles at KCC compared with measurements . . .	84
7.11	Calculated inclination angles at KCI compared with measurements . . .	84
7.12	Calculated surface accumulation rate	86
7.13	Comparison between calculated and GPR-derived accumulation rate . . .	87
7.14	Comparison between calculated and measured density profiles	89
7.15	Comparison between calculated and measured temperature profiles . . .	91
7.16	Backward trajectories starting from the KCC drilling site	94
7.17	Aerial view of backward trajectories starting from KCC and KCI	95
7.18	Aerial view of backward trajectories starting from KCC, KCI, KCH, CC and KCS	96
7.19	Aerial view of forward trajectories starting from KCC, KCI, KCH, CC and KCS	96
7.20	Calculated chronologies of the ice cores KCC and KCI compared with annual layer counting and radiocarbon dating results	98
7.21	Calculated chronologies of the ice cores KCH, CC and KCS compared with annual layer counting dating results	99
7.22	Depths of equal age calculated for all five IUP drilling sites	102
7.23	Calculated depths of equal age compared with depths of equal age derived from IRHs	103
A.1	Measured orientation angles at KCC (2016)	128
A.2	Measured orientation angles at KCI (2016)	128
A.3	Evolution of the norm of the velocity solution during the model spin-up .	129
A.4	Evolution of the norm of the density solution during the model spin-up .	130

List of Tables

2.1	Characteristics of the five deep ice cores recovered at CG (IUP cores) . . .	8
3.1	Summary of the quantities required for the enthalpy method	28
5.1	Data sources used to estimate the surface DEM	44
5.2	Data sources used to estimate the bedrock DEM	45
5.3	Basal heat fluxes estimated at the borehole sites	55
6.1	List of the most relevant Elmer and Elmer/Ice solvers used in this work .	61
7.1	Comparison of calculated and at the ice cores observed accumulation rates	87
7.2	Basic information about the measured temperature profiles	92
A.1	Measured surface velocities 2014–15	125
A.2	Measured surface velocities 2015–16	126
A.3	Measured surface velocities 2014–16	126
A.4	Measured surface accumulation 2014–15 and 2015–16	127
A.5	Source points and ice ages of the KCC drill site	131
A.6	Source points and ice ages of the KCI drill site	132
A.7	Source points and ice ages of the KCH drill site	133
A.8	Source points and ice ages of the CC drill site	134
A.9	Source points and ice ages of the KCS drill site	135

List of Abbreviations

AD	Anno Domini
AWI	Alfred Wegener Institute, Bremerhaven
BP	Before present ¹
CC	Deep ice core at Colle Gnifetti
CFA	Continuous Flow Analysis
CG	Colle Gnifetti
DEM	Digital elevation model
DG	Discontinuous Galerkin
DGPS	Differential GPS
GG	Grenzgletscher
GOLF	General orthotropic linear flow law
GPR	Ground-penetrating radar
GPS	Global Positioning System
IUP	Institute of Environmental Physics, University of Heidelberg
KCC	Deep ice core at Colle Gnifetti
KCH	Deep ice core at Colle Gnifetti
KCI	Deep ice core at Colle Gnifetti
KCS	Deep ice core at Colle Gnifetti
LA-ICP-MS .	Laser Ablation Inductively Coupled Plasma Mass Spectrometry
POC	Particulate organic carbon
PSR	Potential solar radiation
SUPG	Streamline Upwind Petrov-Galerkin
USF	User function
VAW	Versuchsanstalt für Wasserbau, Hydrologie und Glaziologie (ETH Zürich)

¹When [years BP] is used as unit for the model calculated ages of ice, “present” is the age of the glacier surface

w. e. Water equivalent

ZAA Zero annual amplitude

A Appendix

A.1 Measured surface velocities (2014–16)

Surface velocities measured at CG in the frame of this work are summarized in the Table A.1, A.2 and A.3 (velocities visualized in Figure 4.2). Details concerning surveying methods and error estimation are given in section 4.1. The position of the stakes (in 2014) are expressed using the Swiss coordinate system, with the x -coordinate pointing to the east and the y -coordinate pointing to the north.

Table A.1: Surface velocities measured from the 24th September 2014 to the 25th September 2015.

Stake ID	coord. x [m]	coord. y [m]	v_x [m a ⁻¹]	v_y [m a ⁻¹]	Δv_x (1σ) [m a ⁻¹]	Δv_y (1σ) [m a ⁻¹]
2	633989	86502	0.344	1.290	0.198	0.223
3	634050	86439	0.438	1.329	0.198	0.216
5	634046	86512	0.546	0.970	0.204	0.221
6	634002	86451	0.372	1.429	0.198	0.227
7	633920	86393	-0.289	0.882	0.200	0.227
8 ¹	633949	86467	-0.096	1.236	0.196	0.225
9 ²	634004	86565	0.220	1.362	0.197	0.224
12	633899	86367	-0.500	0.445	0.211	0.208
13	633950	86403	-0.185	1.180	0.197	0.229
15	634028	86480	0.577	1.127	0.202	0.219
17	633910	86458	-0.465	1.412	0.199	0.225
19	633885	86510	-0.008	1.711	0.196	0.232
20	633874	86412	-0.527	0.751	0.208	0.220

¹ nearby KCC drilling site

² nearby KCI drilling site

Table A.2: Surface velocities measured from the 25th September 2015 to the 24th September 2016.

Stake ID	coord. x [m]	coord. y [m]	v_x [m a ⁻¹]	v_y [m a ⁻¹]	Δv_x (1 σ) [m a ⁻¹]	Δv_y (1 σ) [m a ⁻¹]
2	633989	86502	0.082	0.962	0.085	0.138
5	634046	86512	0.346	0.734	0.098	0.136
8 ¹	633949	86467	0.274	1.260	0.088	0.137
9 ²	634004	86565	0.274	1.042	0.089	0.136
15	634028	86480	0.198	0.796	0.089	0.137

¹ nearby KCC drilling site

² nearby KCI drilling site

Table A.3: Surface velocities measured from the 24th September 2014 to the 24th September 2016.

Stake ID	coord. x [m]	coord. y [m]	v_x [m a ⁻¹]	v_y [m a ⁻¹]	Δv_x (1 σ) [m a ⁻¹]	Δv_y (1 σ) [m a ⁻¹]
2	633989	86502	0.210	1.127	0.091	0.139
5	634046	86512	0.446	0.853	0.104	0.136
8 ¹	633949	86467	0.089	1.247	0.089	0.141
9 ²	634004	86565	0.248	1.202	0.091	0.139
15	634028	86480	0.383	0.963	0.097	0.136

¹ nearby KCC drilling site

² nearby KCI drilling site

A.2 Measured surface accumulation (2014–16)

Surface snow accumulation rates acquired at CG in the period 2014–2016 are summarized in Table A.4. The installation sites of the stakes are represented with the accompanying ID numbers in Figure 4.2. The accumulation measured in the timespan 2014–15 is much higher than in the year after. Such a strong inter-annual variability is consistent with the glaciological settings of CG, since the accumulation regime is mostly dominated by wind erosion and solar irradiation, rather than by the meteorological precipitation rate.

Table A.4: Surface accumulation measured at CG from September 2014 to September 2015, and from September 2015 to September 2016.

Stake ID	coord. x [m]	coord. y [m]	Accumulation 2014–15 [m a ⁻¹]	Accumulation 2015–16 [m a ⁻¹]	Ratio acc ₁₄₋₁₅ / acc ₁₅₋₁₆
2	633989	86502	1.34	0.59	2.27
3	634050	86439	1.22	-	-
5	634046	86512	0.58	0.18	3.22
6	634002	86451	1.85	-	-
7	633920	86393	1.69	-	-
8 ¹	633949	86467	1.85	0.73	2.53
9 ²	634004	86565	1.10	0.13	8.46
11	633973	86631	1.72	-	-
12	633899	86367	1.43	-	-
13	633950	86403	2.09	-	-
15	634028	86480	1.11	0.50	2.22
17	633910	86458	1.92	-	-
19	633885	86510	1.62	-	-
20	633874	86412	1.89	-	-

¹ nearby KCC drilling site

² nearby KCI drilling site

A.3 Orientation angles measured at KCC and KCI

Orientation angles measured at the boreholes KCC and KCI using the magnetometer integrated in DIBOSS [Ryser, 2014; Ryser et al., 2014] are presented in Figure A.1 and A.2. The measurements were performed together with the borehole inclination measurements presented in section 4.3 and are used to assess the quality of the inclination measurements. At both drill sites the ice flows approximately northwards. Hence, the bottom of the boreholes are located southern of the top of the boreholes and the lowest end of the probe inside the boreholes is expected to point southwards. The black lines in Figure A.1 and A.2 indicate the expected orientation of the probe inside the boreholes (ca. southwards orientation, therefore ca. 180°). In this work, inclination measurements with corresponding orientation angles deviating more than 60° from the expected direction are considered not reliable enough and are therefore rejected (see rejected points in Figure A.1, and in Figure 4.6 in section 4.3).

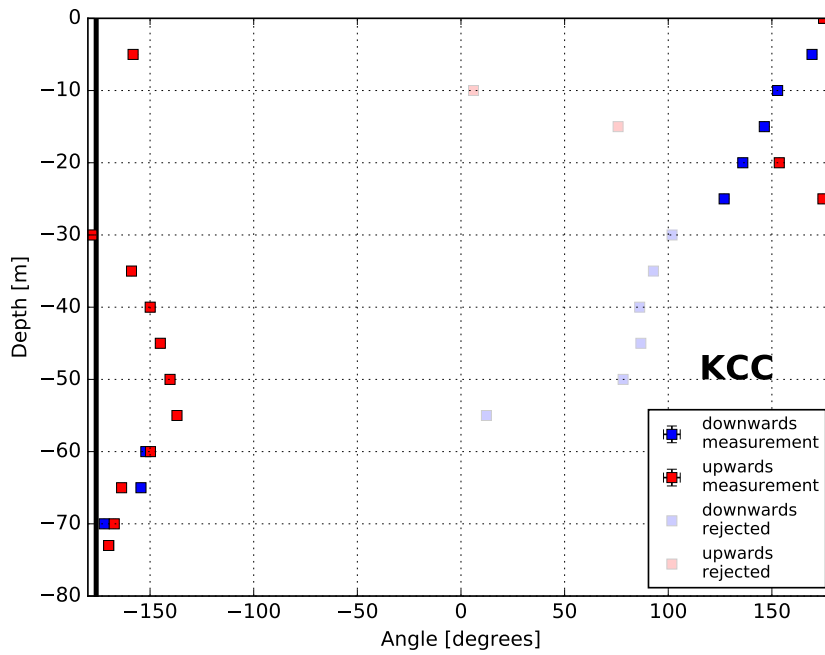


Figure A.1: Measured orientation angles at KCC in September 2016, i.e. ca. 3 years after drilling. The black line indicates the expected borehole orientation (southwards) according to the flow direction at surface. Orientation angles deviating more than 60° from the expected borehole orientation indicate mispositioning of the probe inside the borehole and are rejected.

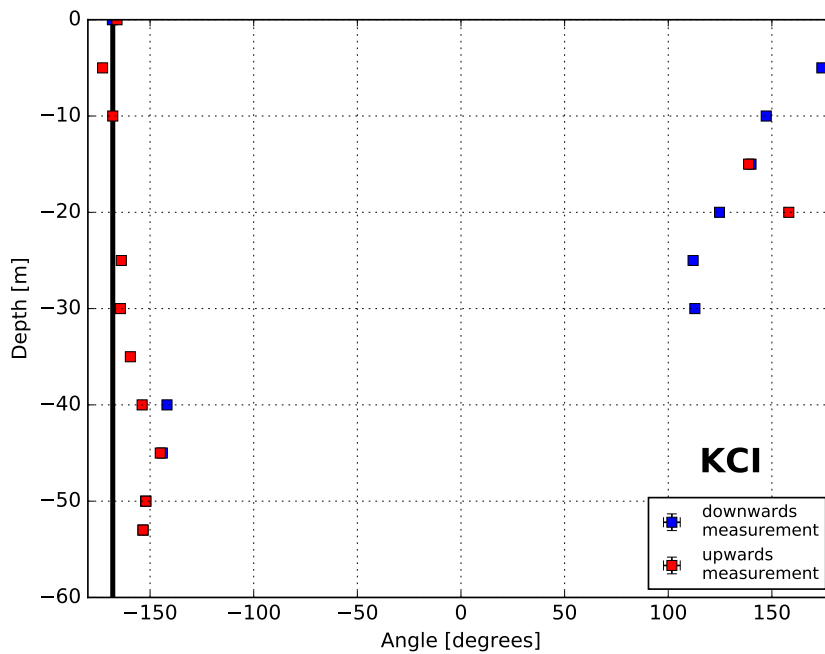


Figure A.2: Measured orientation angles at KCI in September 2016, i.e. ca. 11 years after drilling. The black line indicates the expected borehole orientation (approximately southwards) according to the flow direction at surface.

A.4 Convergence plots

The spin-up of the full Stokes model, required to reach a steady fully coupled solution, is described in Figure 5.13 in section 5.4. Figure A.3 and A.4 show how the norm of the velocity and density solution change during the model spin-up used to produce the results described in chapter 7. The spin-up lasted 5000 iteration steps (time step size of 0.1 years). During the first 1000 iteration steps only the Stokes and the continuity equation are coupled. Diagnostic simulations to update the temperature field are executed every 100 iteration steps starting from the 1000th step (see the discontinuity in the velocity solution in Figure A.3). At the end of the spin-up, changes in the norm of the velocity solution are of order 10^{-2} , whereas changes in the norm of the density solution are of order 10^{-6} to 10^{-5} .

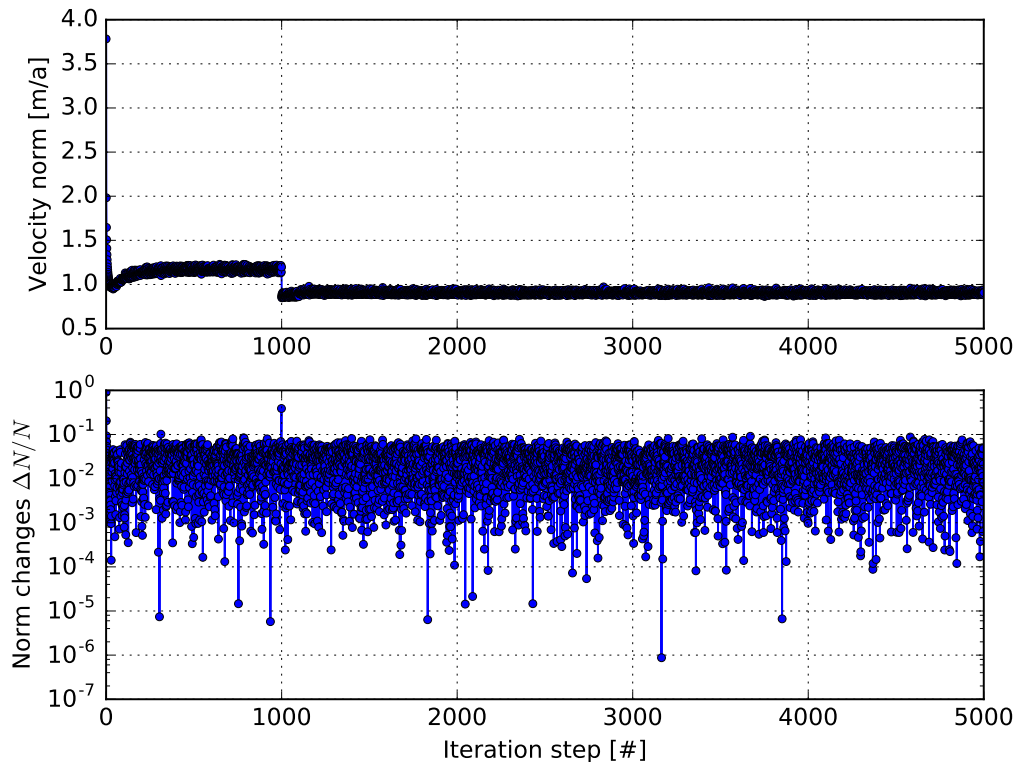


Figure A.3: Evolution of the norm of the velocity solution during the model spin-up (5000 iteration steps with a step size of 0.1 years). Note the discontinuity at the 1000th iteration step, where the temperature field is calculated for the first time.

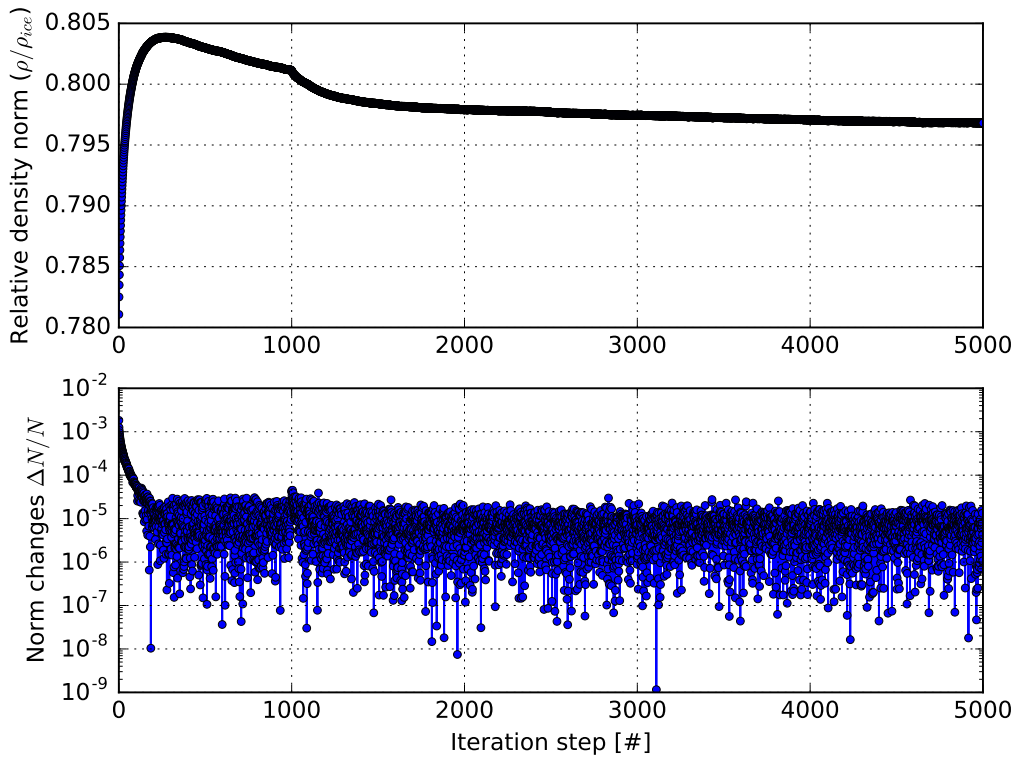


Figure A.4: Evolution of the norm of the density solution during the model spin-up (5000 iteration steps with a step size of 0.1 years). Note the discontinuity at the 1000th iteration step, where the temperature field is calculated for the first time.

A.5 Ice-core source coordinates and chronologies

The calculation of backward trajectories starting from the drill sites KCC, KCI, KCH, CC and KCS using the Runge-Kutta method is presented in section 7.5. The source points, i.e. the interception points between trajectories and the glacier surface are plotted with red dots in Figure 7.17 and 7.18. The coordinates of the calculated source points are tabulated for each drill site in Table A.5, A.6, A.7, A.8 and A.9 (Swiss coordinate system, with the x -coordinate pointing to the east and the y -coordinate pointing to the north). The uncertainty of the positions is $\sim 10\%$ of the distance from the corresponding drill site (see section 7.5), equally distributed in the x - and y -direction. The ice ages are determined from the integration time of the trajectories and have an error of $\sim 20\%$.

Table A.5: Source points of ice samples recovered at the KCC drill site at different depths and corresponding ice ages with uncertainties.

Core depth	Source point coord. x [m]	Source point coord. y [m]	Position error $\Delta x, \Delta y$ [m]	Age [years BP]	Age error [years BP]
3.2	633948.1	86462.4	0.2	4	1
5.0	633948.3	86460.3	0.3	8	2
6.8	633948.4	86457.9	0.5	12	2
8.6	633948.6	86455.4	0.7	17	3
10.4	633948.9	86452.5	0.9	22	4
12.2	633949.1	86450.2	1.0	26	5
14.0	633949.4	86447.5	1.2	32	6
15.8	633949.8	86444.7	1.4	38	8
17.6	633950.1	86441.9	1.6	44	9
19.4	633950.6	86438.5	1.9	51	10
21.2	633951.0	86435.3	2.1	59	12
23.0	633951.5	86431.9	2.4	67	13
24.8	633952.0	86428.8	2.6	75	15
26.6	633952.5	86425.2	2.8	84	17
28.4	633953.1	86421.5	3.1	94	19
30.2	633953.7	86417.8	3.4	105	21
32.0	633954.3	86414.1	3.6	116	23
33.8	633955.1	86410.0	3.9	128	26
35.6	633955.8	86406.2	4.2	141	28
37.4	633956.9	86401.6	4.5	157	31
39.2	633957.7	86397.9	4.8	172	34
41.0	633958.9	86393.0	5.1	192	38
42.8	633959.9	86389.0	5.4	211	42
44.6	633961.1	86384.5	5.8	235	47
46.4	633962.3	86380.3	6.1	258	52
48.2	633963.6	86376.1	6.4	284	57
50.0	633965.3	86371.2	6.7	314	63
51.8	633966.8	86366.7	7.1	351	70
53.6	633968.4	86361.9	7.4	394	79
55.4	633970.4	86356.8	7.8	446	89
57.2	633972.3	86352.2	8.2	504	101
59.0	633974.2	86347.9	8.5	567	113
60.8	633976.1	86344.0	8.8	645	129
62.6	633979.3	86338.0	9.2	763	153
64.4	633983.9	86329.8	9.9	954	191
66.2	633986.9	86324.9	10.3	1194	239
68.0	633990.4	86319.6	10.7	1601	320
69.8	633993.8	86315.4	11.1	2465	493
71.6	633997.6	86311.2	11.4	7003	1401

Table A.6: Source points of ice samples recovered at the KCI drill site at different depths and corresponding ice ages with uncertainties.

Core depth	Source point coord. x [m]	Source point coord. y [m]	Position error $\Delta x, \Delta y$ [m]	Age [years BP]	Age error [years BP]
3.1	633999.3	86549.8	0.3	4	0.9
4.9	633998.1	86546.8	0.5	8	1.5
6.7	633996.6	86542.9	0.8	12	2.4
8.5	633995.3	86539.3	1.1	17	3.3
10.3	633993.8	86535.3	1.4	22	4.4
12.1	633992.4	86531.2	1.7	27	5.4
13.9	633990.8	86526.5	2.1	34	6.8
15.7	633989.5	86522.5	2.4	40	8.0
17.5	633987.9	86517.3	2.8	48	9.6
19.3	633986.4	86512.2	3.1	56	11.1
21.1	633985.1	86507.1	3.5	64	12.8
22.9	633983.7	86501.9	3.9	73	14.6
24.7	633982.3	86496.1	4.3	83	16.6
26.5	633981.2	86490.9	4.7	93	18.5
28.3	633980.1	86485.0	5.1	105	20.9
30.1	633979.1	86479.3	5.5	117	23.3
31.9	633978.3	86473.0	5.9	130	26.0
33.7	633977.6	86466.6	6.4	145	29.0
35.5	633976.9	86459.8	6.9	162	32.3
37.3	633976.4	86452.5	7.4	181	36.2
39.1	633976.0	86444.2	8.0	203	40.7
40.9	633975.8	86435.2	8.6	230	46.1
42.7	633975.8	86425.5	9.3	262	52.4
44.5	633976.3	86416.6	9.9	296	59.2
46.3	633977.1	86408.0	10.5	335	67.0
48.1	633978.3	86399.1	11.1	384	76.7
49.9	633979.6	86391.3	11.6	437	87.4
51.7	633981.2	86383.6	12.1	506	101.3
53.5	633983.6	86374.4	12.8	613	122.6
55.3	633987.8	86360.6	13.7	837	167.4
57.1	633992.2	86348.5	14.5	1184	236.9
58.9	633994.6	86343.1	14.9	1470	294.0
60.7	633997.1	86338.1	15.3	1960	391.9
62.5	633999.4	86333.6	15.6	3323	664.6

Table A.7: Source points of ice samples recovered at the KCH drill site at different depths and corresponding ice ages with uncertainties.

Core depth	Source point coord. x [m]	Source point coord. y [m]	Position error $\Delta x, \Delta y$ [m]	Age [years BP]	Age error [years BP]
3.4	633923.2	86381.0	0.2	5	1
5.2	633924.1	86379.5	0.3	10	2
7.0	633924.9	86378.2	0.4	14	3
8.8	633925.7	86376.8	0.5	19	4
10.6	633926.7	86375.1	0.6	24	5
12.4	633927.7	86373.4	0.8	30	6
14.2	633928.7	86371.7	0.9	37	7
16.0	633929.7	86370.0	1.1	44	9
17.8	633930.6	86368.5	1.2	50	10
19.6	633931.8	86366.5	1.4	58	12
21.4	633932.8	86364.8	1.5	67	13
23.2	633933.7	86363.1	1.6	75	15
25.0	633934.8	86361.2	1.8	85	17
26.8	633936.1	86359.0	2.0	96	19
28.6	633937.4	86356.8	2.1	108	22
30.4	633938.7	86354.6	2.3	122	24
32.2	633940.2	86352.1	2.5	137	27
34.0	633941.6	86349.8	2.7	153	31
35.8	633943.2	86347.1	2.9	173	35
37.6	633944.7	86344.5	3.2	194	39
39.4	633946.7	86341.2	3.4	220	44
41.2	633948.4	86338.3	3.7	249	50
43.0	633950.6	86334.8	4.0	286	57
44.8	633952.7	86331.3	4.3	326	65
46.6	633955.4	86326.8	4.6	382	76
48.4	633959.2	86321.2	5.1	461	92
50.2	633963.3	86315.5	5.6	567	113
52.0	633967.5	86310.4	6.1	698	140
53.8	633972.7	86304.9	6.6	908	182
55.6	633979.2	86299.4	7.2	1313	263

Table A.8: Source points of ice samples recovered at the CC drill site at different depths and corresponding ice ages with uncertainties.

Core depth	Source point coord. x [m]	Source point coord. y [m]	Position error $\Delta x, \Delta y$ [m]	Age [years BP]	Age error [years BP]
2.7	633872.4	86415.8	0.1	2	0
4.5	633873.9	86414.5	0.3	5	1
6.3	633875.4	86413.1	0.4	8	2
8.1	633876.9	86411.9	0.6	12	2
9.9	633878.3	86410.5	0.7	15	3
11.7	633880.2	86408.8	0.9	19	4
13.5	633881.6	86407.4	1.0	23	5
15.3	633883.6	86405.5	1.2	29	6
17.1	633885.4	86403.6	1.4	33	7
18.9	633887.3	86401.7	1.6	39	8
20.7	633889.1	86399.7	1.8	45	9
22.5	633890.9	86397.8	2.0	51	10
24.3	633893.1	86395.4	2.2	59	12
26.1	633895.1	86393.2	2.4	67	13
27.9	633897.3	86390.7	2.6	75	15
29.7	633899.6	86388.1	2.9	85	17
31.5	633901.6	86385.7	3.1	94	19
33.3	633904.4	86382.3	3.4	108	22
35.1	633906.7	86379.4	3.7	120	24
36.9	633909.5	86375.6	4.0	137	27
38.7	633912.2	86371.7	4.3	156	31
40.5	633915.1	86367.5	4.7	178	36
42.3	633918.1	86362.9	5.1	203	41
44.1	633921.1	86358.1	5.5	234	47
45.9	633924.3	86353.2	5.9	270	54
47.7	633927.8	86347.8	6.3	315	63
49.5	633931.6	86341.9	6.8	374	75
51.3	633935.9	86335.2	7.4	458	92
53.1	633941.1	86326.9	8.1	581	116
54.9	633948.8	86315.2	9.1	805	161
56.7	633956.4	86306.8	9.9	1082	216
58.5	633962.9	86301.2	10.5	1421	284
60.3	633971.1	86295.7	11.1	2060	412

Table A.9: Source points of ice samples recovered at the KCS drill site at different depths and corresponding ice ages with uncertainties.

Core depth	Source point coord. x [m]	Source point coord. y [m]	Position error $\Delta x, \Delta y$ [m]	Age [years BP]	Age error [years BP]
3.0	633748.0	86484.6	0.2	2	0
4.8	633750.6	86485.1	0.4	3	1
6.6	633753.5	86485.6	0.6	5	1
8.4	633756.4	86486.1	0.8	7	1
10.2	633759.3	86486.5	1.0	9	2
12.0	633762.6	86487.0	1.3	11	2
13.8	633764.9	86487.3	1.4	12	2
15.6	633767.9	86487.6	1.6	15	3
17.4	633771.0	86487.9	1.9	17	3
19.2	633773.9	86488.2	2.1	19	4
21.0	633776.3	86488.4	2.2	21	4
22.8	633779.4	86488.5	2.5	24	5
24.6	633782.4	86488.6	2.7	26	5
26.4	633785.6	86488.6	2.9	29	6
28.2	633788.6	86488.6	3.1	32	6
30.0	633791.4	86488.5	3.3	35	7
31.8	633794.6	86488.3	3.5	38	8
33.6	633797.9	86488.0	3.8	41	8
35.4	633800.6	86487.8	3.9	44	9
37.2	633803.8	86487.3	4.2	48	10
39.0	633807.1	86486.8	4.4	52	10
40.8	633810.4	86486.1	4.6	56	11
42.6	633813.6	86485.3	4.9	60	12
44.4	633817.1	86484.4	5.1	64	13
46.2	633820.4	86483.4	5.3	69	14
48.0	633823.8	86482.3	5.6	74	15
49.8	633827.2	86481.0	5.8	80	16
51.6	633830.9	86479.4	6.1	86	17
53.4	633834.6	86477.6	6.3	92	18
55.2	633838.3	86475.7	6.6	99	20
57.0	633842.1	86473.5	6.9	107	21
58.8	633845.9	86471.1	7.2	115	23
60.6	633849.7	86468.5	7.5	124	25
62.4	633853.8	86465.3	7.8	134	27
64.2	633857.6	86462.2	8.1	145	29
66.0	633861.8	86458.4	8.5	157	31
67.8	633865.9	86454.4	8.8	170	34
69.6	633870.1	86450.2	9.2	185	37
71.4	633873.9	86446.2	9.5	199	40

73.2	633878.3	86441.4	9.9	217	43
75.0	633882.6	86436.3	10.3	238	48
76.8	633887.4	86430.3	10.8	261	52
78.6	633891.9	86424.2	11.2	287	57
80.4	633896.0	86418.5	11.6	318	64
82.2	633900.0	86412.5	12.1	353	71
84.0	633903.9	86406.7	12.5	395	79
85.8	633907.9	86400.6	12.9	446	89
87.6	633912.0	86394.4	13.4	508	102
89.4	633917.3	86385.3	14.0	606	121
91.2	633922.7	86375.2	14.7	747	149
93.0	633928.9	86363.3	15.6	971	194
94.8	633937.3	86347.4	16.7	1404	281
96.6	633944.9	86333.3	17.7	2423	485

Acknowledgements

Diese Arbeit konnte dank der Unterstützung vieler Menschen vollendet werden:

- Vielen Dank an **Dietmar Wagenbach**. Ohne dich hätte ich niemals die Eiswelt entdeckt und diese Arbeit begonnen. Vielen Dank für das anfängliche Vertrauen, obwohl ich aus einem anderen Gebiet der Physik gekommen war. Leider konnten wir nur in der Entstehungsphase dieser Arbeit zusammen arbeiten und sicherlich hätten die vergangenen drei Jahren einen anderen Charakter gehabt.
- Vielen Dank an **Prof. Dr. Olaf Eisen** für deine Betreuung, sehr aufmerksame und detaillierte Diskussionen meiner Zwischenergebnisse und hilfreichen Ratschläge. Du hast für mich immer Zeit gefunden. Auch wenn ich wortwörtlich an einer steilen Felswand hing.
- Vielen Dank an **Prof. Dr. Klaus Pfeilsticker** für Ihre Bereitschaft zur Erstellung des Zweitgutachtens.
- Vielen Dank an **Pascal Bohleber** für das Mitteilen deiner Leidenschaft für hochalpine Forschung und deiner Erfahrung in Sachen Colle Gnifetti und Eiskerne. Vielen Dank auch für die vielfältige Auswahl an selbstgebrauten Biersorten, die du uns mitgebracht hast.
- Many thanks to **Olivier Gagliardini** and all the “Elmer guys”. Many thanks for guiding me in the first steps of assembling the model, for rapid and efficient support during the whole project, for discussions of the results and for providing code.
- Vielen Dank an **Martin Lüthi** für das Mitteilen deiner vorherigen Erfahrungen im Modellieren des Colle Gnifettis, für das kritische Bewerten meiner Zwischenergebnisse und für die sehr konstruktiven Vorschläge. Vielen Dank dir und der VAW für das Ausleihen der Inclinometer-Sonde.
- Vielen Dank an **Martin Hoelzle** für die Unterstützung bei den Feldkampagnen, für die kritische Diskussionen meiner Zwischenergebnisse und für die Bereitstellung von Temperaturmessungen.
- Vielen Dank an **Kurt Roth** für die wertvollen Gespräche, Diskussionen und für das Ausleihen der Leica Station.
- Vielen Dank an **Ingeborg Levin** und **Susanne Preunkert**, und nicht nur für das aufmerksame, ausführliche, schnelle und sehr konstruktive Korrekturlesen dieser

Arbeit, sondern auch für das kulinarische Verwöhnen u.a. in Form von Brezel, Laugenbrötchen, Vitello Tonnato und raffinierten Espresso, und für die menschliche Unterstützung.

- Vielen Dank an die Eisgruppe in der Form wie ich sie erlebt habe und zwar: **Helene Hoffmann, Johanna Kerch, Josef Lier** und **Lars Zipf**. Danke Helene, dass du als erfahrenstes Gruppenmitglied immer für uns als Referenz da gewesen bist, und vielen Dank auch für das Korrekturlesen. Viel Spaß in der Antarktis! Danke Johanna für dein Engagement innerhalb und außerhalb der Gruppe. Danke Josef für die vielen lustigen und lehrreichen Gespräche, viel mehr als nur Fließmodellierung und Glaziologie. Danke an Lars, und nicht nur für die Einweisungen bei der Praktikumsbetreuung oder dem Ski fahren, sondern auch für das Näherbringen von für mich unbekanntem Saunamethoden und von neuen Horizonten der Volksmusik.
- Vielen Dank an die Menschen, die bei der Kampagne geholfen haben, insbesondere **Michael Sabasch**, der kurzfristig einspringen konnte, und die Bergführer **Richard Biner** und **Jeremias Varela**.
- Molte grazie alla **mia famiglia**, che da lontano mi sostiene e mi ha dato la possibilità di seguire i miei interessi e le mie passioni und vielen Dank an **Anja**, die mit Geduld mich in allen diesen Jahren unterstützt hat.